



Unione Europea
Fondo Sociale Europeo

Sede Amministrativa
UNIVERSITA' DEGLI STUDI DI SASSARI
Dipartimento di Scienze Botaniche, Ecologiche e Geologiche
Sede Consorzata
UNIVERSITA' DI NAPOLI "FEDERICO II"
Dipartimento di Scienze della Terra



1562

SCUOLA DI DOTTORATO IN

Scienza della Natura e delle sue Risorse

INDIRIZZO

Scienza e Tecnologia dei Minerali e delle Rocce di Interesse
Industriale

XXV CICLO

Tesi di dottorato

**Post-emplacement minerogenetic processes in Upper
Tufo Giallo della Via Tiberina (Latium): a
mineralogical and volcanological approach**

IL DIRETTORE
Prof. Marco Curini Galletti

TUTORE
Prof. Piergiulio Cappelletti

DOTTORANDO
Dott. Gianmarco Rapisardo

COTUTORE
Prof.ssa Paola Petrosino

INDEX

INTRODUCTION	6
1. GEOLOGICAL SETTING	10
1.2. SABATINI VOLCANIC DISTRICT	14
1.3. TUFO GIALLO DELLA VIA TIBERINA	19
1.3.1. LOWER TUFO GIALLO DELLA VIA TIBERINA	19
1.3.2. UPPER TUFO GIALLO DELLA VIA TIBERINA	20
2. FIELD INVESTIGATION	22
2.2. PROXIMAL AREA OF ERUPTIVE CENTRE	23
2.3. DISTAL AREA FROM ERUPTIVE CENTRE	30
2.4. SAMPLE LOCATION	32
2.5. SAMPLES DESCRIPTION	36
3. METHODS	38
3.2. PHYSICAL ANALYSES	38
3.2.1. GRAINSIZE ANALYSIS	38
3.2.2. COMPONENT ANALYSIS	39
3.3. MINERALOGICAL AND PETROGRAPHICAL CHARACTERIZATION	40
3.3.1. X RAY POWDER DIFFRACTION (XRPD)	40
3.3.2. X RAY FLUORESCENCE SPECTROMETRY (XRF)	46
3.3.3. LOSS ON IGNITION	47
3.3.4. CALCIMETRY	47
3.3.5. OPTICAL MICROSCOPY	49
3.3.6. SCANNING ELECTRON MICROSCOPY (SEM)	49
3.3.7. PHASE CONCENTRATION	51

3.3.8.	THERMAL ANALYSIS	51
3.3.9.	TERMODINAMIC MODELLING	52
3.4.	PHYSICAL-MECHANICAL CHARACTERIZATION	54
3.4.1.	HELIUM PYCNOMETRY	54
3.4.2.	MERCURY INTRUSION POROSIMETRY (MIP)	55
3.4.3.	TOTAL ABSORPTION WATER (UNI EN 13755)	57
3.4.4.	ULTRASONIC WAVE (UNI-EN 14579)	58
3.4.5.	UNIAXIAL COMPRESSIVE STRENGTH (UNI-EN 11926)	59
3.4.6.	LINEAR THERMAL EXPANSION COEFFICIENT (UNI-EN 14581)	60
4.	RESULTS	62
4.2.	PHYSICAL ANALYSES	62
4.2.1.	GRAINSIZE ANALYSIS	63
4.2.2.	COMPONENT ANALYSIS	64
4.3.	MINERALOGICAL-PETROGRAPHICAL CHARACTERIZATION	68
4.3.1.	X-RAY POWDER DIFFRACTION (XRPD)	68
4.3.2.	X-RAY FLUORESCENCE (XRF)	81
4.3.3.	CALCIMETRY	86
4.3.4.	POLARIZING OPTICAL MICROSCOPE (OM)	87
4.3.5.	SCANNING ELECTRON MICROSCOPE (SEM)	89
4.3.6.	EDS MICROANALYSIS	97
4.4.	PHASE CONCENTRATION	113
4.5.	THERMAL ANALYSIS	114
4.6.	THERMADINAMIC MODEL	114
4.7.	PHYSIC-MECHANICAL CHARACTERIZATION	116
4.7.1.	TOTAL ABSORPTION WATER (UNI EN 13755)	118
4.7.2.	ULTRASONIC VELOCITY TEST (UNI EN 14579)	120
	Dott. Gianmarco Rapisardo. Scuola di dottorato in Scienze della Natura e delle sue Risorse.	4
	Indirizzo: Scienza e tecnologia dei Minerali e delle rocce di interesse industriale. XXV ciclo.	
	Post-emplacement minerogenetic processes in Upper Tufo Giallo della Via Tiberina (Latium): a mineralogical and volcanological approach	

4.7.3.	UNIAXIAL COMPRESSIVE STRENGTH TEST (UCS, UNI EN 11926)	121
4.7.4.	LINEAR THERMAL EXPANSION COEFFICIENT (UNI EN 14581)	125
5.	DISCUSSION	126
	CONCLUSION	132
	REFERENCES	135

INTRODUCTION

Several volcanic districts are located in the central-southern Italy; they are all referred to the so called Roman Comagmatic Province activity. These volcanic districts are: Vulsini, Sabatini, Albani Hills, Vico and Ernici Mounts in the Latium Region; Roccamonfina, Phlegraean Fields and Vesuvius volcano in Campanian Region, Mount Vulture in the eastern part of Appennino Lucano. Starting from Middle Pleistocene, most of these volcanic areas were characterized by intense explosive activity, which emplaced widespread pyroclastic products both as fall and pyroclastic density current deposits. The fine ash juvenile fraction of the latter, in particular, often underwent processes of authigenic mineralization of feldspars or zeolites (Langella et al., 2002) that brought to their lithification.

The large availability and workability, along with good physic-mechanical features of pyroclastic deposits, since Greek-Roman age favoured the use as building stone. Several researches proved the high potential of zeolitized volcanoclastites in technological processes. Fields of application of natural zeolitized products are: cation exchange, for heavy-metal and for potential radionuclear ion from wastewater (Colella, 1996; Pansini, 1996; de Gennaro et al. 2005; Cappelletti et al., 2011); cement production where zeolites can be used in the preparation of pozzolanic cements and for the production of lightweight aggregates in the building industry (de Gennaro, 2004; 2005; 2007; 2008; 2009); traditional ceramic and tile production, substituting for commonly utilized raw materials (Di Bartolomeo et al., 1996, de Gennaro et al., 2003; 2007); zootechny, in particular animal feedings and composting (Tsitsishvili et al., 1984); agriculture, as amendants in soil and slow-release fertilizer (Langella et al., 1995; de' Gennaro et al., 1995b, de Gennaro et al., 2009).

On the basis of the above quoted fields of application, it is necessary to obtain an accurate knowledge on minerogenetic processes that led to the zeolitization of deposits, in order to better understand their technological properties and to evaluate the economic potential of bulk deposit (Cappelletti et al., 1999).

The zeolitization process occurred through transformation of precursor material (the most common is volcanic glass), after interaction with alkaline solution (de' Gennaro and Langella, 1996, de' Gennaro et al., 2000). The principals requirements for

zeolitization are: a high proportion of glassy particles, high internal surface area and high permeability, and favorable hydrological conditions (Hay, 1966). Zeolitization is governed also by several conditions, of which emplacement temperature, cooling rate of volcanoclastic deposit, pressure, pH of solution, chemical composition of parent glass and water content (Hall, 1998; Bear et al., 2009) are the most important.

Temperature exerts a control on the species of authigenic minerals. The zeolitization process occurs after emplacement when deposit have cooled to a temperature within the stability range of zeolites (from 50°C to 450°C, Bear et al., 2009). Less hydrous zeolites, such as laumontite, analcime and wairakite, are stable at higher temperature than more hydrous zeolites, such as clinoptilolite, chabazite, and stilbite (Hay and Sheppard, 2001).

Another important factor is the rate of cooling of the deposit, which determines how long it remains in the optimum temperature range for zeolitic alteration (Hall, 1998; Bear., et al., 2009). Cooling volcanic deposit starts immediately after emplacement; the cooling rate depends on several factors: initial temperature, deposits thickness, basement nature. If the deposits are initially wet, zeolitization process can occur very soon, after emplacement. This is what has been hypothesized for a phreatomagmatic eruption that exhibits low emplacement temperature (<100°C; de' Gennaro et al., 2000). The alteration of natural glasses is strongly dependent on pH, and silicate glasses are most quickly altered by strongly alkaline solutions. For zeolitization process to occur, the range of pH must be 7-10; therefore zeolitization takes place under alkaline conditions (Mariner and Surdam, 1970; Hall, 1998; de' Gennaro et al., 1999).

Also the chemical composition of precursor (volcanic glass) exerts a control on the species of authigenic minerals. The zeolite genesis is favored by high-alkaline composition. The reaction rate of glass inversely changes with its silica content. Alkali-rich low silica glass is the most reactive common natural material (Hay, 1966; Sheppard e Gude, 1968, 1969, 1973; Hay and Sheppard, 2001; Bear et al., 2009).

According to de' Gennaro et al (2000), a sufficient quantity of water must be available to enhance the hydration-dissolution of volcanic glass. Magmatic water, that comes from pyroclasts as volatiles can provide part of the water needed to promote zeolitization. Therefore most of the water must be incorporated from an external source before transport or after deposition (Bear et al., 2009).

Mumpton (1973) proposed six types of sedimentary zeolites deposits: 1) volcanic material in alkaline or saline lake system hydrologically closed; 2) deposit formed by slow percolation of meteoric water in hydrologically open system; 3) deposit in marine environments; 4) deposit from hydrothermal activity; 5) deposit formed by low-grade, burial metamorphism; 6) zeolitic deposit in soil and land surface (Passaglia and Vezzalini, 1985; Hay and Sheppard, 2001). Lenzi and Passaglia (1974) proposed another kind of genesis, later called geoautoclave by Aleksiev and Djourova (1975). Previous work on Phlegreans Fields deposit (Neapolitan Yellow Tuff) suggests, that, in order to better understand the physico-chemical condition favorable to the zeolitization and to hypothesize a minerogenetic model, it is necessary a comparative study which takes into the right account both mineralogical and volcanological features (de' Gennaro et al., 2000). A recent study suggested that in addition to the physical-chemical parameters influencing the formation of zeolites (temperature, glass chemistry, and water content), the physical volcanological constrains including eruption style, transport and emplacement processes play a major role in influencing post-emplacement zeolitization in ignimbrites (Bear et al., 2009).

Further information on secondary mineral alteration processes can be provided by the occurrences of authigenic feldspars. Discovery of this last phase would validate an earlier zeolitization process followed by secondary feldspar crystallization, resulting from a series of reactions from metastable phases (zeolites) to more stable phases by interaction with pore solutions (de' Gennaro et al., 2000). This evolution process would lead to the progressive disappearance of zeolite and the crystallization of phases such as analcime and K-feldspar (Dibble and Tiller, 1981). The occurrence of authigenic feldspars would lead to a higher welding degree in the portion of the deposit where the highest temperatures were developed and preserved (Hall, 1998; Cappelletti et al., 2003).

The authigenic mineralization processes have been traced to models often unsuitable to describe the several local condition. The present research deals with the characterization of the authigenic mineralization in the Tufo Giallo della Via Tiberina, a pyroclastic deposits cropping out in a widespread area north of Rome, ascribed to the Sabatini volcanic district. As we anticipated before, the crystallization of authigenic minerals plays an important role in the lithification process of volcanoclastic deposit, influencing

the petro-physical features of material. Because of this, the physico-mechanical characterization of the Tufo Giallo della Via Tiberina was performed as well.

In summary, the main topics addressed in the present research are:

- ✓ An accurate investigation of the volcanological features of Tufo Giallo della Via Tiberina, aimed at pointing out the possible presence of different eruptive units within the formation.
- ✓ The mineralogical-petrographical characterization of the products of these different units, aimed at defining the zeolite content and investigating the type of zeolites and their stratigraphical and areal changes.
- ✓ The evaluation of the physico-mechanical properties of the products of the Tufo Giallo della Via Tiberina, taking into account the variation of the mineralogical-petrographic features.

Ultimately, the purpose of the research are

- ✓ to hypothesize a mineralogical model able to explain, in a comprehensive framework, the genesis of the different authigenic phases (chabazite, phillipsite, feldspar) in the Tufo Giallo della Via Tiberina pyroclastic deposits.
- ✓ to try and verify if, and to what extent, the physico-mechanical properties of the products are linked to their mineralogical features.
- ✓ To set the crystallization sequences, in order to assume a mineralogical model;
- ✓ To establish thermodynamic modeling in order to calculate stability fields for an assemblage of a variety of zeolites, including chabazite, phillipsite, and analcime.

1. GEOLOGICAL SETTING

Plio-Quaternary magmatism developed after the opening of the Tyrrhenian back arc basin. Starting from Pliocene, both insular and peninsular Italy became the site of intense volcanic activity. Plio-Quaternary magmatism in Italy exhibits an extremely variable composition, and petrological and geochemical data are used to group the activity in various magmatic provinces, mainly linked to different types of magma genesis (Peccerillo, 2003 and references therein). Petrographic and geochemical data made it possible to recognize several magmatic provinces separated by tectonic lines: Tuscany, Intra-Appennine, Roman, Ernici-Roccamonfina, Campania, Vulture, Aeolian Arc, Sicily, Sardinia, Tyrrhenian sea floor (figure 1.1) (Peccerillo, 2003, 2005).

The Tuscany province (14–0.2 Ma) displays anatectic silicic magmas and minor mantle derived calcalkaline to ultrapotassic mafic rocks. The Roman, Umbria, Ernici-Roccamonfina and Neapolitan provinces (0.8 Ma to present) are formed by mantle derived potassic to ultrapotassic rocks having variable trace element and isotopic compositions. The Aeolian arc (1 Ma to present) mainly consists of calcalkaline to shoshonitic rocks. The Sicily province contains young to active centers (notably Etna) with a tholeiitic to Na-alkaline affinity. Finally, volcanoes of variable composition occur in Sardinia and, as seamounts, on the Tyrrhenian Sea floor. Magmas in the Aeolian arc and along the Italian peninsula have a subduction related geochemical character, whereas the Sicily and Sardinia provinces display intraplate signatures.

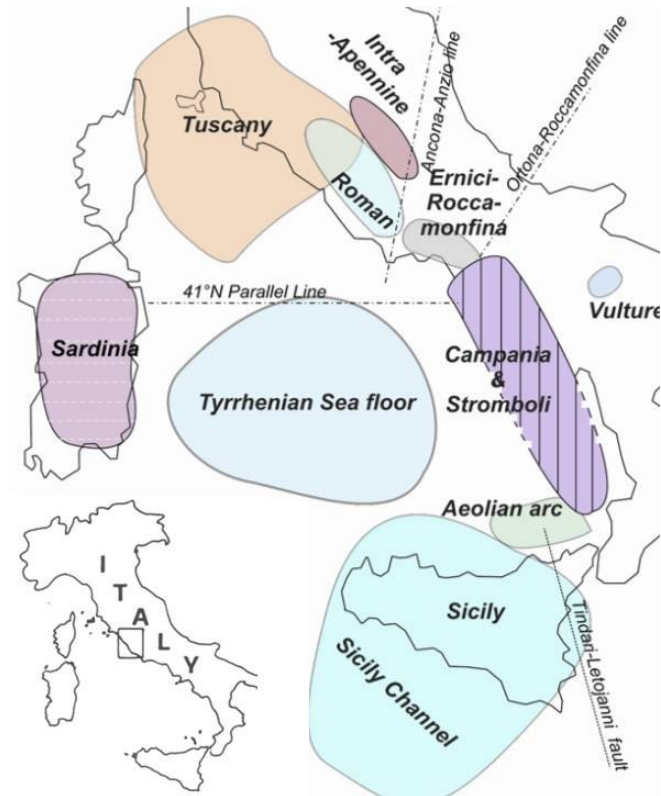


Figure 1.1: Distribution of magmatic province in Italy (Peccerillo, 2003, 2005)

The Roman Magmatic Province (hereafter RMP), comprises several volcanic districts: Albani Hills, Tolfa-Ceriti-Manziana, Sabatini, Cimino-Vicano, and Vulsini (figure 1.2). The compositional range of volcanic products spans from potassic to ultrapotassic and from SiO_2 -undersaturated to SiO_2 -saturated (Peccerillo, 2003, 2005).

The extensional faulting, started during Pliocene and ended during Lower Pleistocene, induced the location of the aforementioned volcanic districts along a NW–SE tectonic trend (Sottili et al., 2004, 2010).

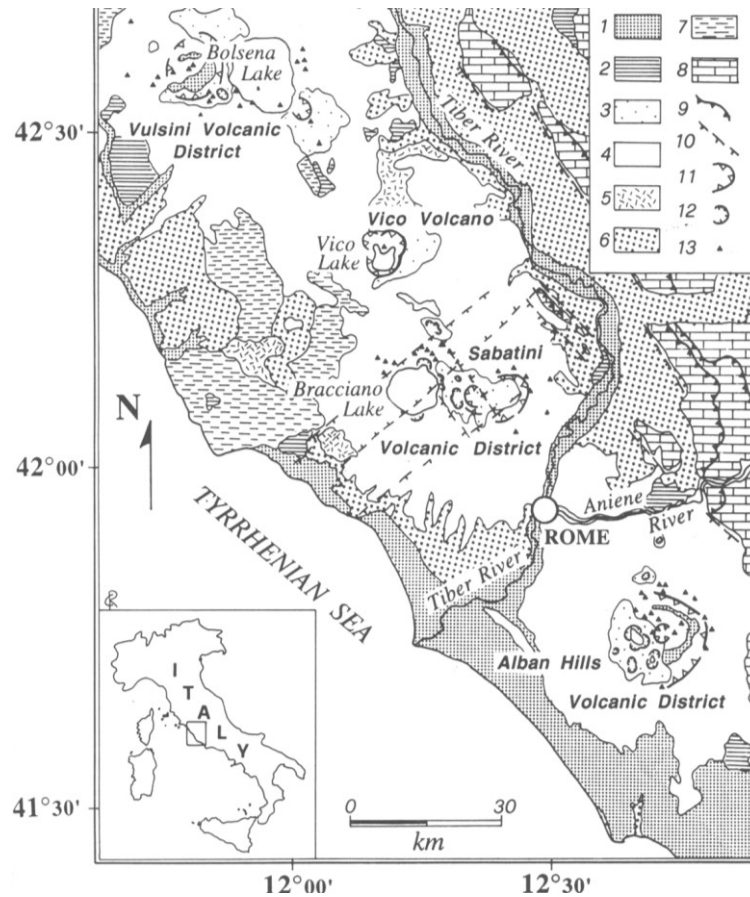


Figure 1.2: Sketch map of the Latian volcanic area, central Italy. Legend: (1) continental and marine sediments (upper Pleistocene to Holocene); (2) travertine; (3) hydromagmatic units; (4) Tolfa Cerite Manziate acidic volcanic district; (5) K-alkaline volcanic products; (6) Plio-Pleistocene marine sediments; (7) Cretaceous-Oligocene marls and marly limestones; (8) Meso-Cenozoic limestones and marls; (9) thrusts; (10) normal faults; (11) calderas; (12) craters; (13) scoria cones (De Rita et al., 1996).

This tectonic phase disrupted the Meso-Cenozoic carbonate substratum, forming a series of horsts and grabens and causing marine ingressions during the Upper Pliocene and Lower Pleistocene with deposition of clay and sand bearing sequences, that make up the substratum of the volcanic products (Sottili et al., 2004).

The RMP included both central and areal volcanism; the former phase is characterized by the early formation of a stratovolcano and the subsequent collapse of this volcano into a caldera, as is the case of the Albani Hills district (De Rita et al., 1996). The areal volcanism showed an activity located at different vents and a main depression larger than 8 km in diameter, as is the case of the Sabatini district. The depression associated with areal volcanism corresponds to both a peak in post-orogenic extension and to the beginning of volcanic activity (De Rita et al., 1996).

1.1. PREVIOUS STUDIES ON THE GEOLOGICAL ONSET OF THE TUFO GIALLO DELLA VIA TIBERINA (TGVT)

Since the late 19th century many geologists have investigated the volcanic districts of central-southern Latium to understand the genesis and evolution of the volcanic sources and the depositional characteristic of the erupted products (Campobasso et al., 1994). The volcanism, forming the Latial volcanic province, developed from late Pliocene to late Pleistocene as a consequence of rifting in the Tyrrhenian basin and post-orogenic extension in the Apennines (Conticelli et al., 1986; Serri et al., 1992).

The Sabatini volcanic district is one of the most complex volcanic areas in Central Italy. Mattias and Ventriglia (1970) report a detailed analysis of the stratigraphy of the Sabatini complex. Several papers (Nappi et al., 1979; De Rita et al., 1983; Campobasso et al., 1994) investigated the stratigraphic correlation among the products of different volcanic centers of the Latial volcanic province (Alban Hills, Sabatini and Vulsini districts). The pre-volcanic setting and the interrelation of the various factors, controlling the evolution of Sabatini volcanic district, have been studied in detail by De Rita et al. (1996), and Nappi and Mattioli (2003). The former reconstruct the volcano-tectonic history of the Sabatini volcanic district, suggesting that the lithological and structural features of the pre-volcanic basement controlled the onset of volcanic activity, the style of eruptions and the relationship among the different volcanic units in the Sabatini volcanic district.

The activity of Sabatini volcanic district was mainly explosive and emplaced several formations, among which the Tufo Giallo della Via Tiberina (TGVT). This formation is considered the most important pyroclastic deposit ascribed to the Sacrofano caldera, located nearby the present Morlupo town. The first studies of the TGVT formation were carried out by palaeontologists, because several fossils of vegetable and remnants of animals (Blanc A.C. et al., 1955; Follieri et al., 1961; Follieri, 1963) were discovered within the pyroclastic product. Mattias and Ventriglia (1970) were the first authors to investigate the stratigraphic and volcanological features of the TGVT. Later on, Alvarez (1973) debated the role of TGVT formation, in the paleo-geographic evolution of the area. TGVT was then analyzed by Nappi et al (1981) and De Rita et al. (1983) as far as its geologic, mineralogic and petrographic characteristics were concerned. For the TGVT formation, these authors supposed an origin from a

pyroclastic flow eruption. Nappi et al. (1979) identified the TGVT as a single pyroclastic flow unit from the Sacrofano eruptive centre; subsequently Campobasso et al. (1994) recognized in an out-crop at Calcata seven pyroclastic units of TGVT; most of these units have been identified as ash fall deposit rather than ignimbrite.

The TGVT formation, identified by Mattias and Ventriglia (1970), corresponds to Sacrofano Lower Pyroclastic Flow Unit of De Rita et al. (1993). Karner et al. (2001), through the acquisition of new geochronologic data, refined the volcanic stratigraphy of Sabatini district. According to Karner et al. (2001) the TGVT was emplaced over a time span and is composed of several flow units emplaced during two different periods separated by about 10 ka; it should be divided into two eruptive units: Lower Tufo Giallo della Via Tiberina and Upper Tufo Giallo della Via Tiberina. Karner et al. (2001) defined the flow units that outcrop at Prima Porta (Tufo Giallo di Prima Porta), which were formerly ascribed to the TGVT, to a different formation, made up of a series of pyroclastic deposits ca. 30 ka younger than the TGVT.

Masotta et al. (2010) investigated the eruptive conditions and textural and chemical variation of juvenile clasts in the TGVT pyroclastic deposit. They suppose a temperature and H₂O content-zoned magma chamber, involving the emplacement of both subaphyric–vitrophyric and highly crystalline magma, which brought to the presence in the products of two types of juvenile clasts: white pumice and black grey scoria. This model is based on the occurrence of extensive crystallization in the cooler, peripheral zones of the magma chamber at initially H₂O-undersaturated conditions.

1.2. SABATINI VOLCANIC DISTRICT

The Sabatini Volcanic District (hereafter SVD) was characterized by a number of explosive eruptions occurred during the last 600 ka that produced pyroclastic deposits cropping out in a widespread area north of Rome. It extended over an area of about 1800 km², and was bordered by Albani Hills Volcanic District, Vico Volcanic District, Tolfetano-Cerite-Manziate Volcanic District and by the Tiber River Valley along the southern, northern, western and eastern side, respectively (Cioni et al 1987; Lombardi et al., 1974; de Rita et al., 1988, 1993, 1997) (figure 1.3). The location of volcanic activity, the styles of eruptions, and the relationships and distribution of volcanic units in the SVD were controlled by the pre-volcanic lithology and structure (De Rita et al., 1996).

The areal activity of the SVD was characterised by highly explosive, caldera-forming eruptions that produced widespread sub-plinian and plinian fall deposits. These eruptions were generally associated to weakly explosive post-caldera activity that produced lavas and scoria cones. Hydromagmatic activity dominated the most recent activity, occurring mainly in the *horst* areas of the limestone substrate (Masotta et al., 2010, reference therein).

Three main eruptive sectors with different volcanic activities were distinguished (figure 1.3):

- 1) The western sector, located within the Bracciano volcano-tectonics depression, displayed effusive and Strombolian eruptions (De Rita et al., 1996; Nappi et al., 2003);
- 2) The eastern sector, the eruptive centre of which was located around Sacrofano volcano, showed a phreatomagmatic activity linked to the presence of deep aquifers (Nappi et al., 2003);
- 3) The northern sector was characterized by phreatomagmatic explosions, sourcing at several monogenic vents, located in Baccano area (De Rita et al., 1996; Nappi et al., 2003).

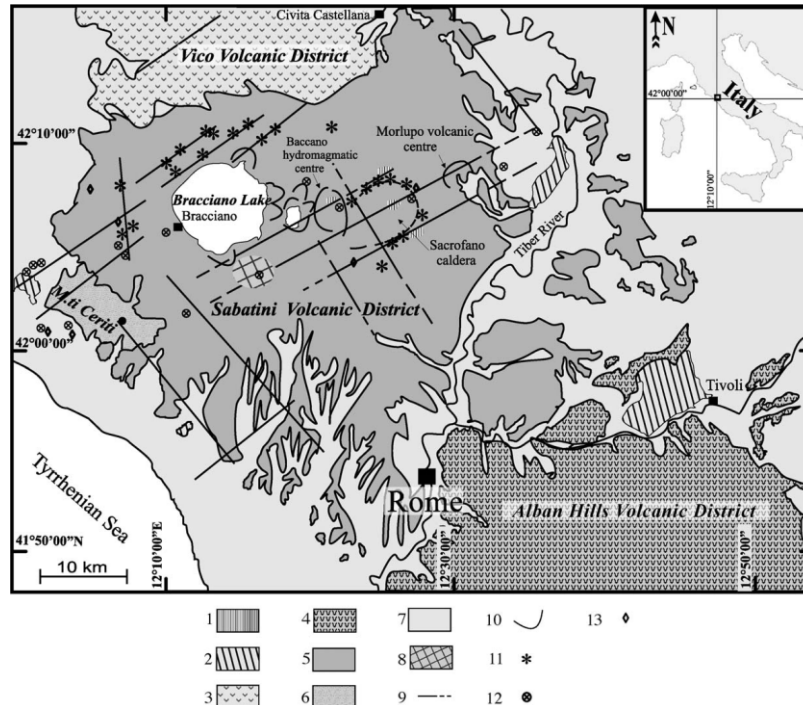


Figure 1.3: Geological sketch map of the Sabatini Volcanic District and nearby areas (central Italy). Main volcanic centres and tectonic lineaments from literature data are also shown. Legend: (1) hydrothermally altered volcanic terrains; (2) travertines; (3) products of the Vico Volcanic District; (4) products of the

Alban Hills Volcanic District; (5) products of the Sabatini Volcanic District; (6) products of the

Dott. Gianmarco Rapisardo. Scuola di dottorato in Scienze della Natura e delle sue Risorse. 15

Indirizzo: Scienza e tecnologia dei Minerali e delle rocce di interesse industriale. XXV ciclo.
Post-emplacment minerogenetic processes in Upper Tufo Giallo della Via Tiberina (Latium): a mineralogical and volcanological approach

Tolfetano-Cerite-Manziate Volcanic District; (7) sedimentary terrains (Mesozoic to Olocene); (8) inferred vent area for the pyroclastic fall units of this study; (9) major tectonic lineaments (observed/supposed); (10) crater rims of the late hydromagmatic centres and Sacrofano caldera rims; (11) strombolian scoria cones; (12) hot springs; (13) gas emissions. (Sottili et al., 2004).

The SVD eruptive activity started at ca. 600 ka, and can be divided into three main periods (Masotta et al., 2010):

- 1) The early activity period, ranging in age between 600 ka and 514 ka, with the eruptive centre located around the present Morlupo town. During this period the First Ash Fall Deposits (hereafter FAD), the Grottarossa Pyroclastic Sequence and also the Tufo Giallo della Via Tiberina formation (hereafter TGVT) were emplaced (Karner et al., 2001).
- 2) The intermediate activity period, characterized by intense explosive events, comprised the main eruptions of Tufo Rosso a Scorie Nere (449 ± 1 ka), Tufo di Bracciano (320 ka) and Tufo di Sacrofano (281 ka), attributed to the Southern Sabatini and Sacrofano sources (Sottili et al., 2004; Karner et al., 2001).
- 3) The most recent period of activity ranged from 250 ka to 90 ka, and included Tufo di Pizzo di Prato and Vigna di Valle; this period was characterized by hydromagmatic explosive events (De Rita et al., 1993; Sottili et al., 2010, 2011).

The very first eruption, dated at ca. 582 ka (Karner et al., 2001), emplaced a trachytic lava flow and the First Ash Fall Deposits (FAD) sourcing from the eruptive centre of Morlupo - Castelnuovo di Porto. Around 561 ka, the activity shifted toward the southern part of SVD with the emplacement of Lower Tufo Giallo della Via Tiberina and Upper Tufo Giallo della Via Tiberina, the age of which was 548 ka (Karner et al., 2001). After the deposition of these products several pyroclastic flows were emplaced along the paleo-Tiber valley. Among these were recorded the weakly lithified tuff of Prima Porta (513 ka) and the Grottarossa Pyroclastic Sequence (514 ka) (figure 4) (Karner et al., 2001).

After a quiescence period, during which the Albani Hills volcanic products and several sedimentary deposits were emplaced, started a new eruptive phase, characterized by the deposition of the Tufo Terroso con Pomici Bianche (507-497 ka - Karner et al., 2001) that is made up of four layers identified as A, B, C, D; A and B are ca 50 cm thick around Rome town, where they are labelled “*Granturco*” and separated by two pumice

fall layers (figure 1.4) (Karner et al., 2001; Marra et al., 2011). The D layer represented the sustained column phase deposit of the eruption, which brought to the deposition of Tufo Rosso a Scorie Nere (449 ka) (Giacomelli and Scandone, 2007), one of the most voluminous eruptions of SVD, and was followed by pumice and scoria fall deposits defined as Tufi Stratificati Vari Colori di La Storta, located in the western and southern part of Sabatini Mounts (Karner et al., 2001).

During the period between 320 ka and 200 ka, the activity shifted toward Bracciano and Sacrofano area (Sottili et al., 2010), where effusive and explosive activity occurred at different times; the main ignimbritic events of this time span were the Tufo di Bracciano and Tufo Giallo di Sacrofano which lead to the collapse of the area, followed by effusive activity (Karner et al., 2001; Giacomelli and Scandone, 2007; Sottili et al., 2010).

The last activity period, between 170 ka and 90 ka, showed hydromagmatic and subordinate Strombolian and effusive activities from several monogenetic tuff rings and scoria cones located around the Baccano eruptive centre. This low size activity emplaced the Tufo di Pizzo di Prato and Tufo di Vigna di Valle (figure 1.4) (Giacomelli and Scandone, 2007; Marra et al., 2011).

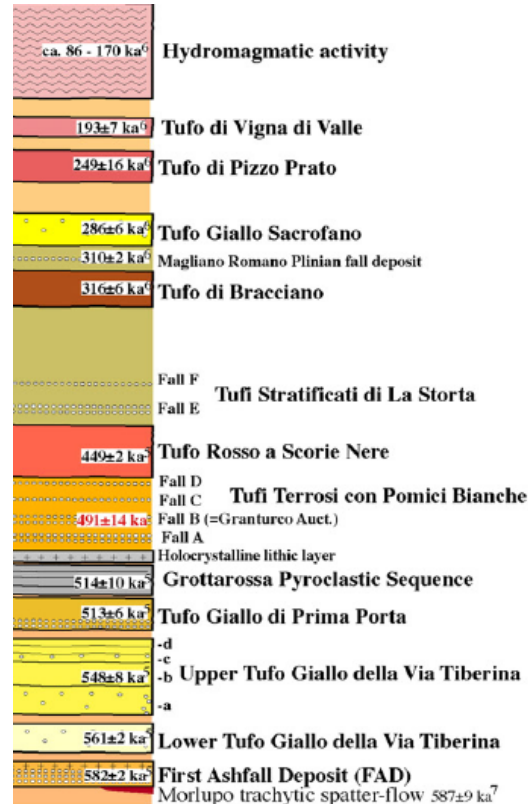


Figure 1.4: Chronostratigraphy of the Sabatini Volcanic District products (Marra et al., 2011).

The SVD belong to the Roman Comagmatic Province (Washington, 1906; Rogers et al., 1986) which is characterized by a particularly high and sometimes discontinuous potassium enrichment relative to silica (Karner et al., 2001). The products display a large chemical variability spanning from the tephrite-phonolite to trachybasalt, tephrite to phonolite fields, with minor latitic and trachytic types in the TAS classification system (LeBas et al., 1986) (figure 1.5).

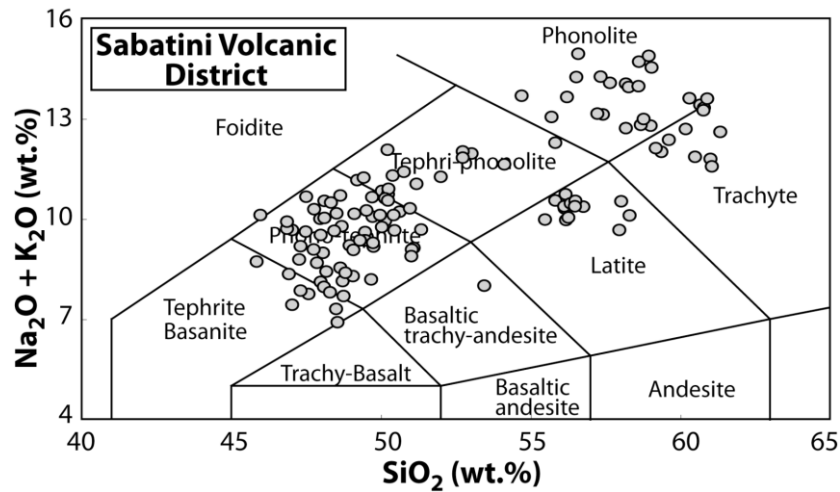


Figure 1.5: TAS diagram showing composition of SVD volcanics (data from Lustrino et al., 2011 and reference therein).

1.3. TUFO GIALLO DELLA VIA TIBERINA

The Sacrofano eruption centre was the source of the Tufo Giallo della Via Tiberina (hereafter TGVT).

The TGVT formation is made up of pumice fragments, leucitic or tephro-leucititic lava fragments embedded in a fine-ash matrix. Engulfed in the fine fraction sanidine, augite, biotite and leucite crystals, and limestone, limestone-marly and clay clasts (Nappi et al., 1979, Lombardi e Meucci, 2006) can be found.

The ash matrix is deeply weathered, due to processes that brought to the formation of zeolites and clay minerals. Chabazite is the main zeolite, found both in the matrix and in the pumice fragments, followed in abundance by phillipsite, whereas the main clay mineral is smectite. The genesis of smectite has been related to the composition of circulating waters, rather than to the mineralogy and chemistry of wall rock (Nappi et al., 1979).

The TGVT was composed of several units that were emplaced during two distinct time intervals, separated by 10 ka (Karner e Renne, 1998; Karner et al., 2001). Between them is somewhere embedded the Tufo Giallo di Trigoria, from Albani Hills Volcanic District. The 10kyr time span separating the two deposits made it possible to divide the TGVT into two eruptive units: Lower Tufo Giallo della Via Tiberina (hereafter LTGVT) and Upper Tufo Giallo della Via Tiberina (hereafter UTGVT).

1.3.1. LOWER TUFO GIALLO DELLA VIA TIBERINA

The LTGVT can be found in the field as a single pyroclastic flow deposit, the age of which was 561 ka (Karner e Renne, 1998; Karner et al., 2001). As to the sedimentary features, the LTGVT is a massive light gray to pale yellow ignimbrite, with abundant white, lapilli-size pumice fragments and frequent accretionary lapilli dispersed throughout.

The base of the formation is a fall deposits with 3-cm thick ash layer, followed by 4-cm of well sorted lapilli layer. LTGVT crops out north of Monti Sabatini around Calcata and along km 13 of the Via Tiberina, with thickness of 4 m and 8 m, respectively (Karner et al., 2001).

1.3.2. UPPER TUFO GIALLO DELLA VIA TIBERINA

The UTGVT consists of three distinct pyroclastic flow units with ranging in age between 551 ka and 547 ka.

The UTGVT is the most widespread ignimbrite deposit of SVD, and its emplacement was able of diverting the course of the paleo-Tiber River toward Rome (Alvarez, 1973; Karner et al., 2001).

This deposit could be divided into three sub units *a*, *b*, *c* separated by two ash layer:

- The sub-unit UTGVT-a occurs as a massive yellow deposit with lava, scoria, and non-metamorphosed sedimentary lithic fragments, mainly made up of limestone and marl clasts. The base of the UTGVT-a is a pyroclastic fall deposit, composed by a 10-cm thick with pumice layer, containing rare lavic and sedimentary clasts. The top of this sub-unit is covered by an ash layer with dune structure, normal grading, and accretionary lapilli, that make it possible to hypothesize a diluted pyroclastic current mechanism of emplacement (Karner et al., 2001).
- The sub-unit UTGVT-b with similar characteristic to those of the basal level UTGVT-a, is 10 m around km 12,7 of Via Tiberina, where the upper 120 cm are made up by an ash deposit. It also crops out around Calcata displaying an 8m thickness (Karner et al., 2001).
- The sub-unit UTGVT-c showed at the base a planar and cross-bedded ash layer and lapilli and pumice-rich layer, which was interpreted as sequence of alternating surge and pyroclastic fall deposits. This sub-unit contained more pumice and scoria fragments than the sub-units *a* and *b*. At the top the unit showed a welded ash layer about 1,50 m, followed by 1,40 m thick layer made up of cm-sized scoria and pumice fragments with normal grading embedded in an ash matrix, which grades into a 1 m-thick ash level (Karner et al., 2001).

Figure 1.6 depicts a stratigraphic section of TGVT around Calcata, where Karner et al (2001) observed the overlap of LTGVT and UTGVT.

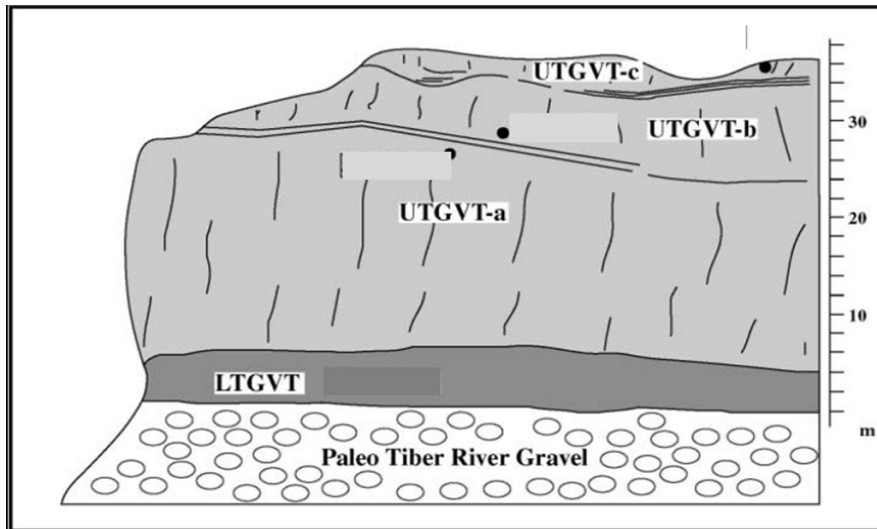


Figure 1.6: Section of Tufo Giallo della Via Tiberina. Legend: LTGVT = Lower Tufo Giallo della Via Tiberina (561 ± 1 ka); UTGVT-a = Upper Tufo Giallo della Via Tiberina sub-unit a (551 ± 1 ka); UTGVT-b = Upper Tufo Giallo della Via Tiberina sub-unit b (548 ± 1 ka); UTGVT-c = Upper Tufo Giallo della Via Tiberina sub-unit c (547 ± 1 ka) (Karner et al., 2001).

2. FIELD INVESTIGATION

The TGVT (560 ka) was main explosive deposits sourcing at the Sacrofano vent. It has been divided into two distinct deposits separated by a 10 ka time span, named LTGVT and UTGVT (Karner e Renne, 1998; Karner et al., 2001).

The LTGVT (561 +/- 1 ka), is a widespread ignimbrite, that crops out to the north of Monti Sabatini around Calcata and to the south-east at km 12.7 of the Via Tiberina. The southernmost outcrop of this volcanic unit is near Grotta Oscura. LTGVT is a massive light gray to pale yellow ignimbrite with abundant white lapilli-size pumice and frequent accreziory lapilli (Karner et al., 2001, Masotta et al., 2010).

The UTGVT is made up of three distinct sub-unit (a, b and c), separated by two ash layers, the age of which ranges between 551 ka and 547 ka (Karner et al., 2001; Nappi et al., 2003).

The UTGVTa is a massive yellow ash deposit with scoria, lava and non-metamorphosed sedimentary lithic fragments, white pumice and accreziory lapilli. The base of UTGVTa has a 10-cm thick horizon, rich in lava, sedimentary lithic clasts and pumice. The upper part of this unit is a fine-grained, bedded ash with abundant accreziory lapilli.

The UTGVTb is an ignimbrite with similar petrographic characteristic to the UTGVTa. The UTGVTc has one meter of alternating planar and cross-bedded ash, lapilli, and pumice rich layers at its base, it is interpreted to be surge and pyroclastic fall deposit (Nappi et al., 2003; Karner et al., 2001).

For the purposes of the present work, the sampling area of UTGVT was firstly selected through the study of previous papers dealing with the products of this formation (Karner et al., 2001; Lombardi et al., 2006). In a second step of the preliminary work, we compared the geological map of the area (geological map n° 365, Monterotondo, scale 1:50,000) and the map of the census of mining edited by PRAE (Piano Regionale delle Attività estrattive) of Latium region (figure 2.1). Finally, a preliminary field survey was carried out in order to define the accessibility and the suitability to the sampling of the whole area.

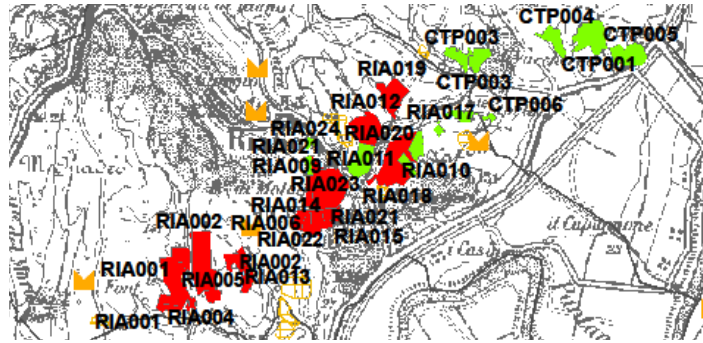


Figure 2.1: Sketch map of active (green) and inactive (red) quarries distribution from map of census of mining edited by PRAE.

2.2. PROXIMAL AREA OF ERUPTIVE CENTRE

km 13 quarry

Under a volcanological point of view, this abandoned quarry is the most important of the whole investigated area, since along its walls the whole sequence of the UTGVT products is exposed. In this quarry, in fact, it is possible to observe both the overlapping of three sub-unit UTGVTa, UTGVTb, UTGVTc with Tufo Giallo di Prima Porta (hereafter TGPP), and the contact with Pyroclastic sequence of Grottarossa (Karner et al., 2001) (figures 2.2 and 2.3). The basal contact of the products of the formation is not exposed.



Figure 2.2: Front of quarry km 13

In this section the thickness of unit UTGVTa was about 10 m, while units UTGVTb, UTGVTc were ca 5 m of thick.

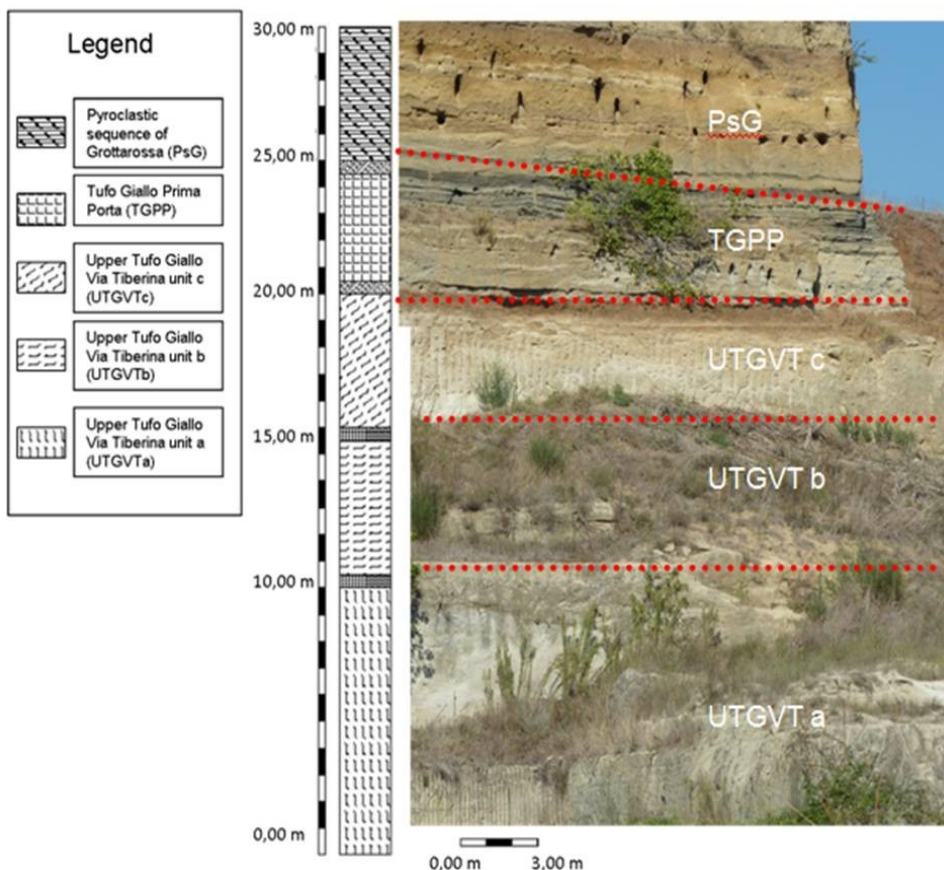


Figure 2.3: Sampling section, where were taken samples in the three sub-unit.

The contact between UTGVTb and UTGVTc was represented by a 10 cm thick scoriaceous layer.

The non-welded top of UTGVTb showed two ash layers containing accretionary lapilli, interbedded to a gray-blackish pumice-rich layer (figure 2.4).



Figure 2.4: On the left top UTGVTb- UTGVTc contact; on the right pumice-rich layer.

In this section the UTGVTc is made up of a 160 cm thick lithified ash horizon, followed by a 140 cm thick fining upward layer of pumice and scoria fragments embedded in a pale yellow ash matrix.

km 12.7 quarry

Along the main wall of the abandoned quarry, the three units making up the whole sequence of the UTGVT can be observed. The basal unit shows a lithified basal layer, passing towards the top to a about 4 m of unwelded ash layer with dune structure. Above this cineritic both the UTGVTb (ca 2 m thick) and UTGVTc can be observed on the topmost part of the wall (figure 2.5).



Figure 2.5: On the left contact between UTGVTa – cineritic top – UTGVTb; on the right un-welded cineritic layer

SICAT quarry

In this quarry, it is possible to observe the overlapping of sub-unit UTGVTb - UTGVTc with TGPP, along the wall there is not any clear evidence of the overlap between sub-unit UTGVTa and UTGVTb; the basal contact of the products of the formation is not exposed (figure 2.6).

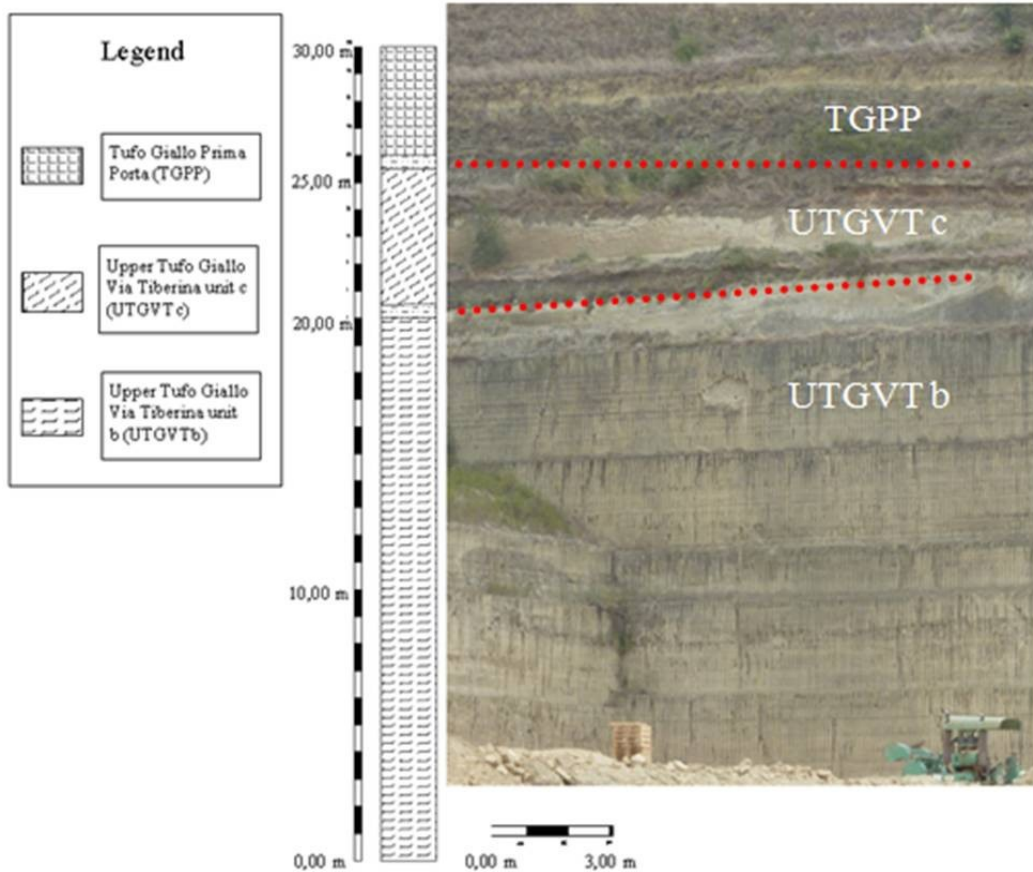


Figure 2.6: SICAT quarry front

Perina quarry

The UTGVT products along the wall of quarry are made up of a deeply welded to welded cineritic deposit, engulfing pale grey to yellowish cm-sized juvenile fragments, often isooriented and clustered in lenses, together with lavic, limestone and marl lithic fragments. Looking at the wall from the basal floor of the quarry, the deposit is very uniform and no clear evidence of the presence of different flow units can be pointed out (figure 2.7). During the sampling, however, the high degree of welding of a layer, corresponding to the second quarrying crag of the wall, was pointed out by the difficult hammering of the rock climber. As to the colour, the dark grey very basal part of the sequence gives way towards the top to a yellowish deposits, but slight changes in colour can be observed here and there along the whole sequence. As to sedimentary structure, slightly laminated layers and low angle dunes can be hardly observed, mainly due to the deep quarrying fingerprints along the wall.

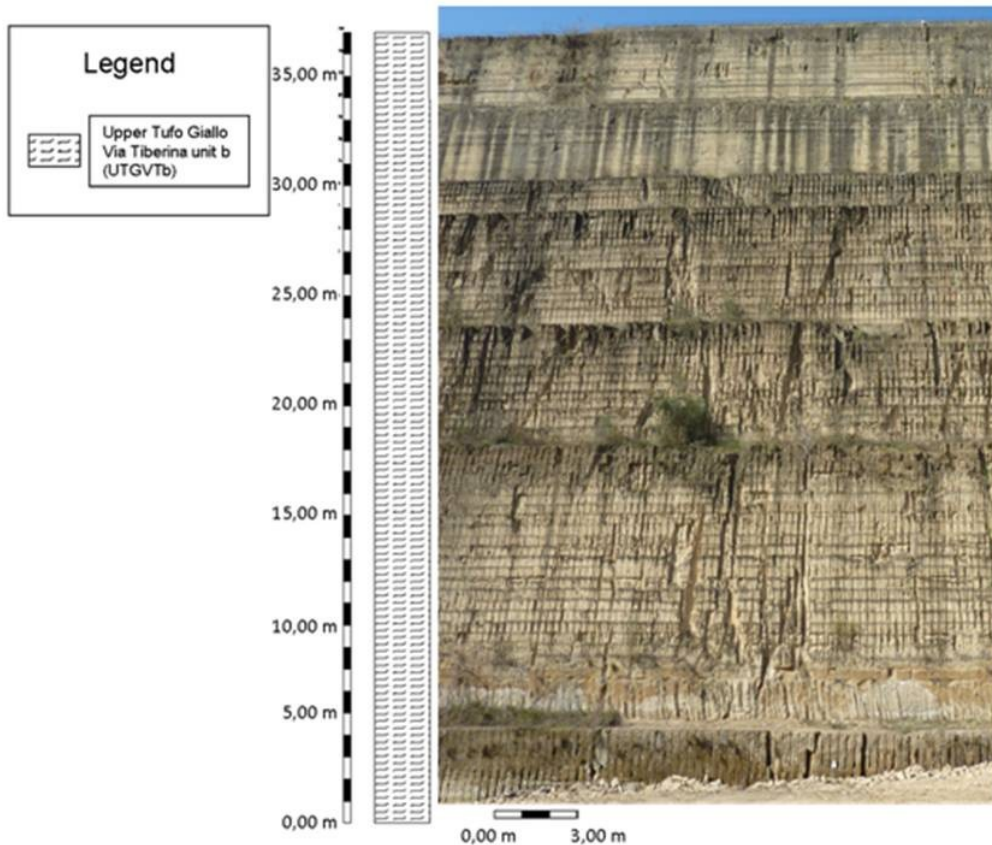


Figura 2.7: Perina quarry front.

Cannetaccio quarry

During the preliminary field survey of the UTGVT outcrops, aimed at selecting the sampling sites, a drill core of 15 m was collected from the quarry floor of the Cannetaccio quarry (figure 2.8).



Figure 2.8: Cannetaccio quarry floor.

In this quarry the UTGVT formation reaches 60m in thickness, along the wall there is not any clear evidence of the overlap between sub-unit UTGVTa and UTGVTb.

Fantini quarry

This quarry is located at km 7,5 of the Via Tiberina, and is the only proximal site where the pre-volcanic substratum of the UTGVT was observed. In this specific site, in fact, a core drilled on the quarry floor pointed out the presence of 2m thick fall products, ascribable to the ancient Sabatini fall products, directly underlying the UTGVT welded tuff and overlaying the Paleo-Tiber clay and sandy sediments (figure 2.9).



Figure 2.9: Drill core on the Fantini quarry floor.

Along the wall, ca 50m thick the whole succession made up of the three sub-units UTGVTa – UTGVTb – UTGVTc, can be observed (figure 2.10).

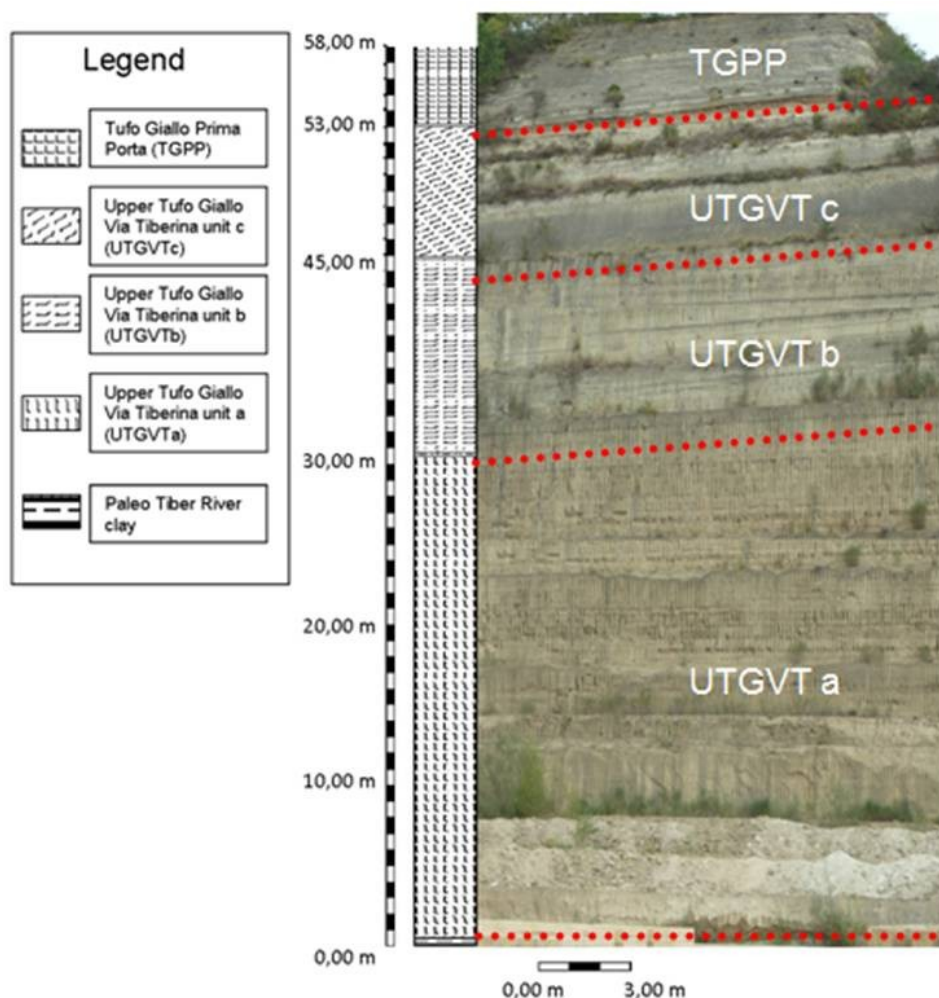


Figure 2.10: Fantini quarry front

The basal part of the sequence is represented by 30 m thick of welded material (UTGVTa), overlain by a cineritic layer. The second unit is made up by a 15m thick yellowish welded layer, overlain by a ca 8 m unwelded deposit (UTGVTc). A paleosol divides the products of the TGVT formation from those of the TGPP.

In the lower unit of TGVT, well visible on the present quarry floor several wooden fragments can be observed embedded in the welded tuff. They are carbonized wood remnants of the trees collapsed by the pyroclastic current during its passage on the soil of the age. Furthermore it can be observed, that the vugs of wooden fragments are filled up in with calcite, which possibly formed diagenetically through a solution-precipitation process. (figure 2.11).



Figure 2.11: On the left wooden fragment, on the right the dashed area shows crystals of authigenic calcite.

2.3. DISTAL AREA FROM ERUPTIVE CENTRE

Calcata

Further field surveys were performed on the distal outcrops of the UTGVT, in the Calcata neighbourhood. The survey, aimed at pointing out the basal and topmost deposits of the UTGVT, made it possible to observe the overlapping of UTGVTa to LTGVT, that reach 20m and 4m in thickness, respectively, and the pre-volcanic basement made up of Plio-Pleistocenic conglomeratic deposit (figure 2.12).

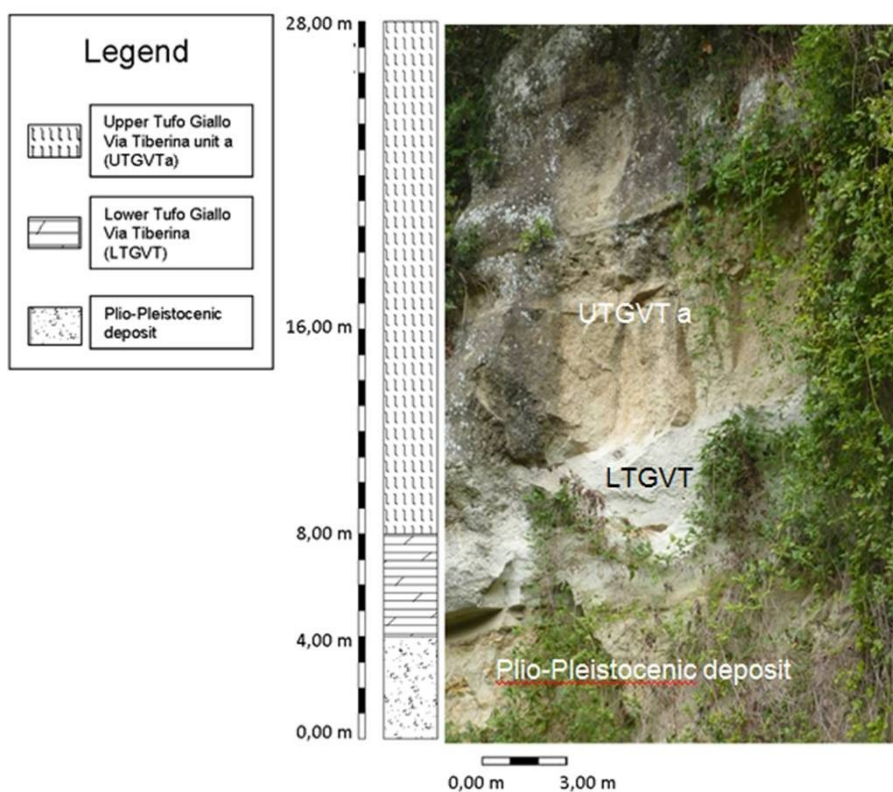


Figure 2.12: Outcrop close to Calcata (Treja valley)

In this outcrop the lowermost sub-unit (UTGVTa) is a massive, accretionary lapilli-bearing, yellow ash deposit, containing diffuse white pumice and scarce grey scoria, lava and non-metamorphosed sedimentary lithic fragments. This deposit directly overlaps the sedimentary basement, here made up of Pliocene fluvial conglomerates.

Castel Nuovo di Porto

Close to Castel Nuovo di Porto village, the non-welded facies of TGVT was observed. This deposit is made up of a 50 cm thick gray pumice layer, which covered an ash layer containing accretionary lapilli (figure 2.13).



Figure 2.13: Castel Nuovo di Porto outcrop, on the left gray pumice layer ; on the right accretionary lapilli

2.4. SAMPLE LOCATION

Samples selected for further laboratory analysis were taken from four active quarries along the Tiberina road managed by “Cave Riunite srl”, namely the Cannetaccio, Perina and SICAT quarries, located between km 11 and km 12 of the consular road, and from the Fantini quarry, located at the km 7,50.

Samples were also taken from two abandoned quarries between 12,7 and 13 km of Tiberina road (figure 2.14).

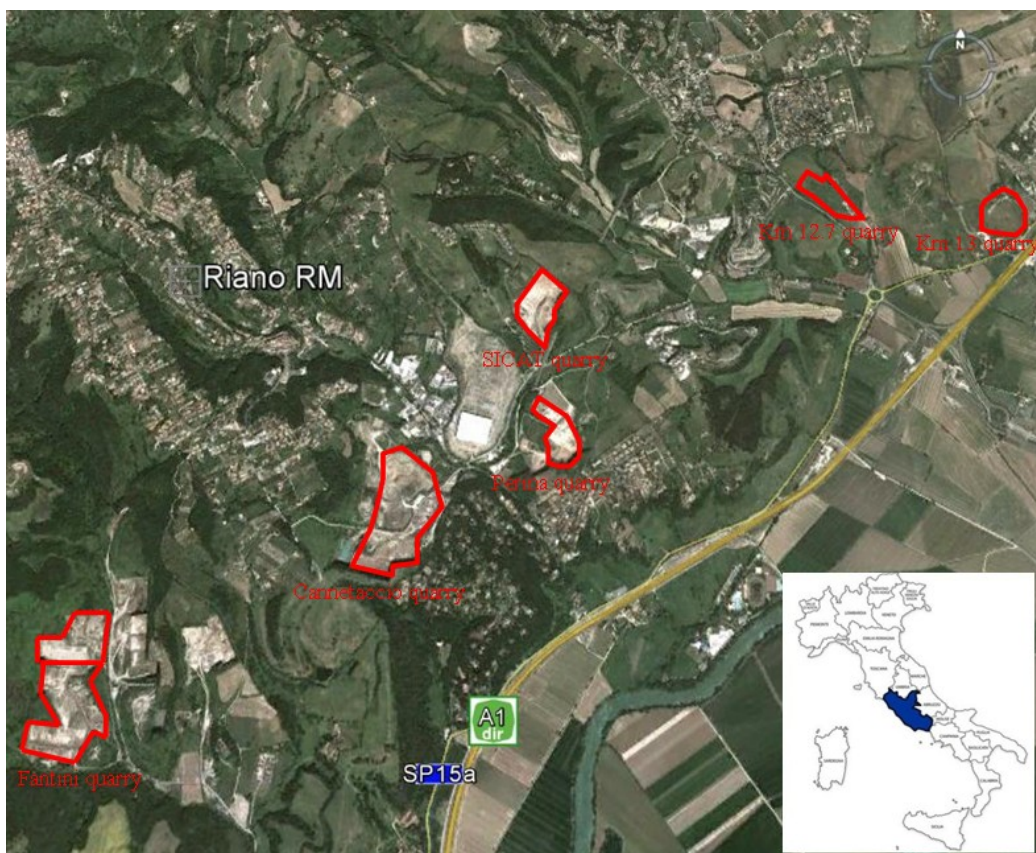


Figure 2.14: Google Earth image, localization of sampling areas.

km 13 quarry

In this quarry samples of sub-units a, b, and c were collected. Samples belong both to the welded and to the un-welded facies, where the un-welded facies represented the passage between UTGVTa -UTGVTb and UTGVTb - UTGVTc. In the figure 2.15 the blue circle point out the sampling points.



Figure 2.15: km 13 quarry front

km 12.7 quarry

Along the main wall of the abandoned quarry, were collected five lithified samples from sub-unit a, 1 m spaced (figure 2.16). The total height of the sampled wall is 15 m high.

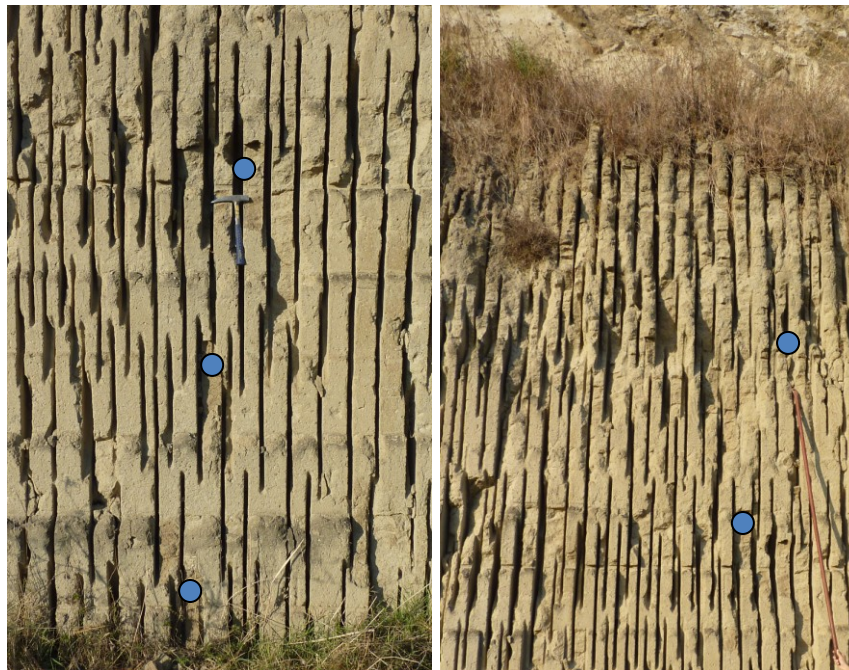


Figure 2.16: km 12.7 quarry front the blue circle point out the sampling points.

SICAT quarry

In this quarry one sample was taken from the wall, a second sample from the quarry floor and a third from a street cut 4m below to the present quarry floor (figure 2.17).



Figure 2.17: SICAT quarry, outcrop below to the quarry floor

Perina quarry

Among the set of quarries above listed, Perina quarry resulted the most suitable to carry out a vertical sampling along a front, collecting 1 m spaced samples. As a matter of fact, the choice was mainly driven by the good accessibility of the quarry floor and by the complete absence of products younger than the UTGVT along the selected wall. The sampling, in fact, was carried out by an expert rock climber under the supervision of the researchers involved in the project. The whole of the sampled wall is 36 m high.

Thirty-eight samples were collected along the main front, whereas the last two were taken from a drainage cut beneath the vertical sampling site.

In the early phases of the research, some scattered samples were taken from two different quarry floors and fronts of the same quarry area (figure 2.18).



Figure 2.18: Perina quarry, first and second site respectively on the left and on the right.

Cannetaccio quarry

Samples 50 cm spaced are collected from the whole of the cored sequence (figure 2.19).



Figure 2.19: Drill core on the Cannetaccio quarry floor

In the last phases of the research, several samples were collected from the quarry floor where the core had been drilled and along one of the quarry walls bordering the same floor. In the figure 2.20 the blue circle point out the sampling points, the dashed area shows the zone where the drill core has been carried out in late.

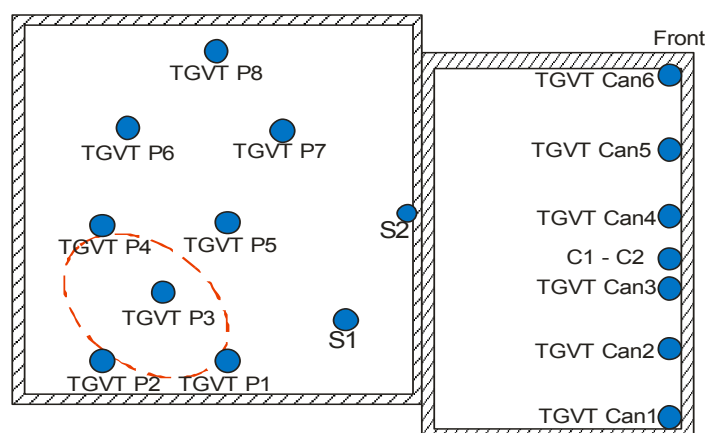


Figure 2.20: Plan of Cannetaccio quarry floor and sample location

Fantini quarry

In this quarry, some scattered samples were taken from two different quarry floors and fronts within the quarry (figure 2.21).



Figure 2.21: Fantini quarry, first and second site respectively on the left and on the right.

2.5. SAMPLES DESCRIPTION

Samples of UTGVTa and UTGVTb are massive, well-lithified, matrix supported with abundant pale grey to yellowish partly altered cm-size juvenile fragments. The matrix is made up of cineritic to coarse ash mainly juvenile. Within the matrix are dispersed cm-sized lava and sedimentary lithic (limestone and marly) fragments, mica biotite, pyroxenes.

Samples of UTGVTc are lithified matrix supported with grey mm-size pumice fragments, within the matrix are dispersed mica biotite, pyroxenes and abundant leucite crystals, almost completely transformed into analcime.

The collected samples with a brief summary of the collection points is reported in table 2.1.

Table 2.1: TGVT, samples collected

Quarry	Sample	Description
km 13 Via Tiberina	a1	Sub-unit a
	a2	Sub-unit a
	a3	Discontinuity a-b (unwelded facies)
	b1	Sub-unit b
	b2	Discontinuity b-c (unwelded facies)
	b2 bis	Discontinuity b-c (unwelded facies)
	c1	Sub-unit c
km 12,7 Via Tiberina	CTP 1	Sub-unit a (base of quarry front)
	CTP 2	Sub-unit a +1 m from base
	CTP 3	Sub-unit a +2 m from base
	CTP 4	Sub-unit a +3 m from base
	CTP 5	Sub-unit a +4 m from base
Sicat	C3_1	Quarry floor
	C3_2	Front. (+4 m from base)
	C3_3	-4m below of quarry floor
Perina	From CV_1 to CV_38	Vertical sampling (CV_1 top - CV_38 base)
	C2_P1_1	First site
	C2_P1_2	Front of first site
	C2_P2_1	Second site
	C2_P2_2	Front of second site
Cannetaccio	From C1_1 to C1_30	Drill core (C1_1 top - C1_30 base)
	CC1	Front opposite from quarry floor
	CC2	Up to the previous
	S1	Quarry floor
	S2	Front below quarry floor
	Can1	Front opposite from quarry floor
	Can2	Wall bordering the quarry floor (+ 15 m)
	Can3	Wall bordering the quarry floor (+ 15 m)
	Can4	Wall bordering the quarry floor (+ 15 m)
	Can5	Wall bordering the quarry floor (+ 15 m)
	Can6	Wall bordering the quarry floor (+ 15 m)
	P1	Quarry floor of drill core
	P2	Quarry floor of drill core
	P3	Quarry floor of drill core
	P4	Quarry floor of drill core
	P5	Quarry floor of drill core
	P6	Quarry floor of drill core
P7	Quarry floor of drill core	
P8	Quarry floor of drill core	
Fantini	C4_1	Quarry floor
	C4_2	Front of quarry floor
	C4_3	Second site
Fantini second site	C5_1	Front of quarry floor
	C5_2	Quarry floor

3. METHODS

For the purposes of present research, in order to better understand the physic-chemical condition favourable to the zeolitization and to hypothesize a minerogenetic model, it is necessary a comparative study which takes into the right account both volcanological and mineralogical features.

Aiming at this, the collected samples underwent: physical analyses (grainsize and component analysis), X ray powder diffraction (XRPD), X ray fluorescence spectrometry (XRF), calcimetry, optical microscopy (OM), scanning electron microscopy (SEM) equipped with energy dispersive X-ray microanalysis (EDS).

A further detailed investigation was carried out on zeolite-enriched samples, through thermal analyses: thermogravimetry (TG), derivative thermogravimetry (DTG) and differential thermal analysis (DTA).

The secondary crystallization of authigenic minerals such as zeolites and feldspars progressively enhances the physical properties of the deposit. Zeolites act as a cementing agent in pyroclastic rocks exhibiting superior mechanical properties compared with non-zeolitized deposits (Aversa and Evangelista, 1998; Evangelista et al., 2000). In order to better understand the lithification process it is undertaken the physic-mechanical characterization of TGVT deposits.

3.2. PHYSICAL ANALYSES

Samples of non-welded facies (TGVT A3, TGVT B2, TGVT B2 bis) were investigated in order to characterize volcanological features through grain size and component analysis.

The samples, before being analyzed, were dried at 70°C and then quartered.

3.2.1. GRAINSIZE ANALYSIS

Grainsize analysis were performed by dry-sieving of 60-100 g of sample with a set of sieves with mesh size spaced at one-phi (Φ) intervals, where $\Phi = -\log_2 d$ (d is the grainsize in millimeters) and ranging in size from -3Φ to $+4\Phi$.

For each size class, the material, retained in each sieve, was weighed, successively the weight percentage and cumulative weight percentage were calculated.

Afterwards, by means the grainsize data, was constructed the cumulative curves of grainsize distribution and determined the Inman (1952) parameters:

- median diameter: $Md\Phi = \Phi_{50}$;
- graphical standard deviation, which is a measure of sorting, $\sigma\Phi = (\Phi_{84} - \Phi_{16})/2$;
- first order skeness $\alpha\Phi = [(\Phi_{84} + \Phi_{16}) - Md\Phi]/\sigma\Phi$

3.2.2. COMPONENT ANALYSIS

The relative proportion of the different components in a pyroclastic deposit reflected its mode of formation and transport process. These features were obtained separating pumice, crystal and lithics in the different size classes.

Component analyses were performed between -3Φ and $+4\Phi$ size interval. The larger size classes ($> -1\Phi$) were hand picked; while for the size classes between -1Φ and $+1\Phi$, hand picking was carried out under binocular microscope. The finest size classes, 2Φ and 3Φ , were counted under binocular microscope, the minimum number of grains was usually 500 grains per sample.

The counted percentage of grains were converted into equivalent weight percentage using a conversion factor that were usually between 0.5 and 0.75.

3.3. MINERALOGICAL AND PETROGRAPHICAL CHARACTERIZATION

Sample preparation: samples were grinded, coned and quartered and entirely sieved < 100 mesh; finally, the powders were quartered again to obtain suitable material for further laboratory analysis.

3.3.1. X RAY POWDER DIFFRACTION (XRPD)

The mineralogical assemblages of UTGVT samples was investigated by X-ray powder diffraction. The powder obtained as above described, it was mixed to α -Al₂O₃, 1 μ m size, (Buehler Micropolish), as internal standard, with a ratio of 80-20 wt% between sample and standard.

The mixture (sample-to-standard) was micronized using a “Mc Crone micronising mill” (figure 3.1) with agate cylinders and wet grinding time (15 min); this procedure produced powders with a <5 μ m particle size in order thus override several problems such as: particle statistic, primary extinction, micro adsorption and preferred orientation (Bish andand Chipera, 1988; Klug and Alexander, 1974).



Figure 3.1: McCrone Micronising Mill.

The XRPD analysis was carried out using a Panalytical X’Pert PRO PW 3040/60 diffractometer for quantitative analysis with X’celerator and MPD PW 3710 unit (figure 3.2).



Figure 3.2: Panalytical X'Pert PRO PW 3040/60 diffractometer.

The operating condition for the acquisition of diffraction patterns were the following :

- $\text{CuK}\alpha$ radiation, 40 kV, 40 mA;
- 4-80° 2 θ scanning interval, 0.017° equivalent step size;
- 120 s per step equivalent counting time.

Data acquisition and interpretation were performed through software Panalytical X'Pert Data Collector[®] and X'pert Highscore Plus[®], respectively (figure 3.3).

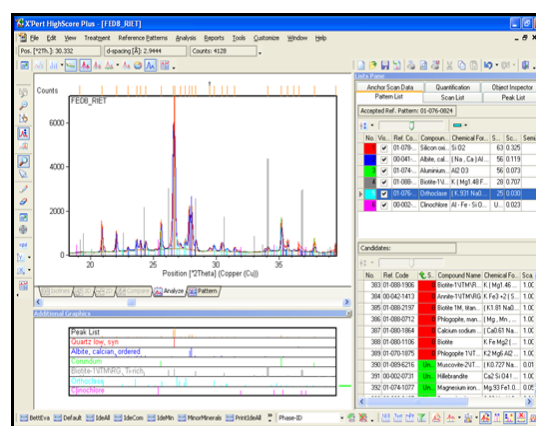


Figure 3.3: Software X'Pert Highscore Plus 2.2

Quantitative mineralogical analyses were performed using the Reference Intensity Ratio (RIR) (Chipera and Bish, 1995), and RIR/Rietveld technique (Bish and Post, 1993).

Reference Intensity Ratio (RIR)

The RIR method represents an evolution of a) internal standard technique proposed by Chung (1974), and b) “*matrix-flushing*” method developed by Bish and Chipera (1988) for quantitative analysis of compounds with several components.

The Reference Intensity Ratio is defined as the ratio between the intensity of a peak, from a given phase, and the intensity of a peak of an internal standard (α -Al₂O₃) in a 50-50 mixture of phase-to-standard (Chipera and Bish, 1995).

According to Chung (1974), the weight per cent of a X_i phase in a mixture was given by:

$$X_i = X_c I_i / K_i I_c$$

- X_c = the internal *standard* percentage,
- K_i = the RIR value of considered reflection,
- I_i = the integrated area of same reflection,
- I_c = the integrated area of internal standard (α -Al₂O₃).

Bish and Chipera (1988) applied this method for natural mixtures containing feldspar and zeolites, improved the methodologies including the effects of variability of chemical composition and preferred orientation of feldspar. Moreover other type of corrections allowed to minimize the effects of peak overlaps.

Rietveld method

The Rietveld method was a technique of full profile analysis, that allowed to obtain, at the same time, information relating to sample and utilized instrument (Young, 1993).

The former was relative to:

- identification and quantization of crystalline phases,
- refinement of structural model of phases,
- determination of micro-structural and textural information;

while the latter allowed to obtain information for:

- wavelength,
- optical component,
- instrumental background.

In order to measure quantitatively each phase, structural models of phases were required, which were obtained from databases like: Inorganic Crystal Structure Database (ICSD), Cambridge Structure Database (CSD), Mineral Structure (MSA).

A report to the IUCr Commission on Powder Diffraction (Smith and Gorter, 1991) lists information about a large number of available programs for Rietveld refinement such as:

- GSAS : It can work with multiple data sets simultaneously, including mixed powder and single crystal data; it provide for separate determination of crystallite size and microstrain parameters.
- DBWS: It uses a pseudo-Voigt function (Young and Desai, 1989), to allow separation of crystallite-size broadening effects and microstrain broadening effects on the bases of order dependence, while permitting each effect to have both a Lorentzian and a Gaussian component.
- RIETAN: It offers the user a choice of Gauss-Newton and Conjugate Direction least-squares algorithms, the choice can be made anew at the start of each refinement cycle.
- XRS-82: It is described as being a complete collection of programs for Rietveld refinement and related calculation. It is a particular favourite to work on zeolite.

Rietveld method was based on the minimization of difference between observed and calculate profile. The quantity minimized in the least-squares refinement was the residual S_y (Young, 1993):

$$S_y = \sum w_i (y_i - y_{ci})^2$$

where:

$$w_i = 1/y_i,$$

y_i = observed intensity at the i th step,

y_{ci} = calculated intensity at the i th step.

During the refinement several variable should be considered: scale factors, instrumental parameters (wavelength; polarization factors P; background function), lattice parameters, structural parameters (atomic coordinates: x, y, z; fractional occupancies; atomic displacement parameters), correction factors (primary extinction; superficial absorption; preferred orientation; sample displacement).

The calculated intensity (y_{ci}) was determined from the square of the absolute value of the structure factor ($|F|^2$), which was calculated from the structural model (Young, 1993):

$$y_{ci} = s \sum L_K |F|^2 \Phi(2\theta - 2\theta_K) P_K A + y_{bi}$$

s = scale factor;

K = represents the Miller indices h, k, l , for a Bragg reflection;

L_K = contain the Lorenz, polarization and multiplicity factor;

Φ = reflection profile function

P_K = preferred orientation;

A = absorption factor;

$|F|^2$ = structure factor for the k th Bragg reflection;

y_{bi} = background intensity at the i th step.

The background intensity at the i th step, y_{bi} , may be obtained from a specified background function; it includes refinable models for an amorphous component contribution. A simple function is a fifth-order polynomial to allow added flexibility in fitting broad humps in the background curves (Young, 1993).

$$y_{bi} = \sum B_m [(2\theta/BKPOS) - 1]^m$$

where BKPOS is the origin that is to be user-specified in the input control file.

In typical Rietveld refinements of crystalline materials, the observed diffraction intensities $y_{obs}(Q)$ can be modelling by summing the contributions from crystalline Bragg scattering and background scattering:

$$y_{obs}(Q) = y_{cx}(Q) + y_b(Q)$$

where:

$y_{cx}(Q)$ = calculated crystalline intensities

$y_b(Q)$ = background intensities

$Q = 4\pi \sin \theta / \lambda$; is the magnitude of the scattering vector

The background is commonly fitted with low-order polynomial functions. In some cases the conventional background functions are unable to account for all non-crystalline scattering :

$$y_{obs}(Q) = [y_{cx}(Q) + y_b(Q)] + y_{ca}(Q)$$

where:

$y_{ca}(Q)$ = additional non crystalline intensity contributions.

High-order polynomials can be used to estimate $y_{ca}(Q)$. One such method is Fourier-filtering (Richardson and Faber, 1986); it involves Fourier transforming residual Rietveld intensities, to produce a correlation function, $d(r)$, related to the radial distribution function for non-crystalline scatterers. In Fourier-filtering a smoothed $y_{ca}(Q)$ is calculated from the reverse Fourier summation of $d(r)$ values:

$$y_{ca}(Q) = y_{inc}(Q) \sum d(r) \sin(Qr)/(Qr) \Delta r$$

where:

$y_{inc}(Q)$ = intensities in the incident spectrum

r = residual intensities from Rietveld refinement, range between 5-15; it depends on the range of significant correlation.

3.3.2. X RAY FLUORESCENCE SPECTROMETRY (XRF)

On the basis of different mineralogical assemblages, subsequently chemical analyses of bulk-rock samples were obtained by X ray fluorescence spectrometry. The XRF allowed to measure the weight per cent for 10 major elements (SiO₂, TiO₂, Al₂O₃, Fe₂O₃, MnO, MgO, CaO, Na₂O, K₂O e P₂O₅) and 11 trace elements (Rb, Sr, Y, Zr, Nb, Sc, V, Cr, Ba, Cu e Zn), as described by Melluso et al. (2005). For this purpose a fixed aliquot of sample (about 4 grams) was reduced to powder using a mortar with agate spheres and dry grinding time for 20 min. Polyvinyl alcohol, at 10 per cent, was added to powder in ratio of 1cc of alcohol and 4 grams of sample; afterward, mixture was oven- dried at 50°C per 48h. After dehydrated, the powder was transferred on metal bearing filled about ½ of boric acid. Afterwards a pressure of 18 atmospheres per 20 seconds has been applied to the sample.

The preparation and analysis of samples were carried out at “Centro di Servizio Interdipartimentale per le Analisi Geomineralogiche” (CISAG) of University “Federico II” of Napoli.

Major and trace elements were determined through Panalytical Axios spectrometer equipped with a W tube and controlled by Super Q 4.0J.L software (figure 3.4).



Figure 3.4: Panalytical Axios spectrometer.

Data were corrected for drift and background effects.

The analytical accuracy was about $\pm 1\%$ for SiO_2 , TiO_2 , Al_2O_3 , Fe_2O_3 , CaO , K_2O e MnO ; and $\pm 4\%$ for MgO , Na_2O e P_2O_5 .

The accuracy of measures for trace elements ranges between $2\div 3\%$ per 1000 ppm, $\pm 5\div 10\%$ per 100 ppm, and $\pm 10\div 20\%$ per 10 ppm.

The detection limits were about 3 ppm for most of trace elements analyzed.

3.3.3. LOSS ON IGNITION

For all samples analyzed by XRF, Loss on Ignition (LOI) was measured. LOI is the weight reduction due to loss of water and carbon dioxide in a sample when it is heat-treated. LOI was estimated placing the sample in a muffle furnace, within a ceramic crucible (previously weighed and brought to constant weight) at a temperature of 1100°C for 2 h. Then sample cooled and weighed; this step was repeated until a constant weight was attained.

3.3.4. CALCIMETRY

In order to verify the calcite content, previously determined with quantitative mineralogical analyses, calcimetry analysis is carried out. Calcimetry allowed to determine the total carbonate content by attacking the sample with hydrochloric acid and subsequently measuring the CO_2 developed.

According to UNI-Normal 32/89, sample was grinded until to obtain a powder less then $63\ \mu\text{m}$ size, then it was dried in oven at $60 \pm 5^\circ\text{C}$ until constant weight.

The Dietrich-Frühling calcimeter, exploited for this analysis, is constituted by a burette of 200 ml for gas collection, and by a tank arranged parallel to the latter and opened in the upper part, while the lower part of tank was linked, through hose, at the lower part of burette (figure 3.5).

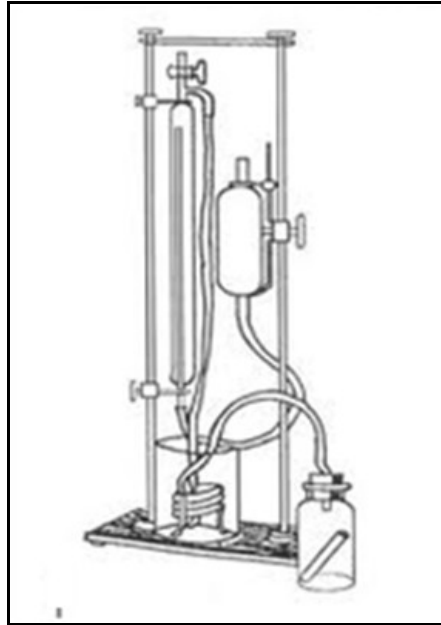


Figure 3.5: Scheme of the equipment for Dietrich-Frühling calcimeter.

The upper part of burette was connected by a hose at an Erlenmeyer flask, where $1 \text{ g} \pm 0,2 \text{ mg}$ of sample and a test-tube containing an acid solution was introduced. The contact between sample and acid solution causes a reaction and the subsequent CO_2 development ($\text{CaCO}_3 + 2 \text{ HCl} \rightarrow \text{CaCl}_2 + \text{CO}_2 + \text{H}_2\text{O}$), which moved from Erlenmeyer flask to burette, determining a reduction in the water column; therefore the gas pressure was lead to equal at the atmospheric pressure, lowering the water level of burette at the same level of the tank.

To measure the volume of CO_2 , as weight per cent, was used the following formula:

$$\% \text{CO}_2 = \frac{7,0573 \cdot 10^{-2}}{M_c T} [(V_1 - V_0)(P - P_{\text{H}_2\text{O}}) + P V_{\text{ass}}]$$

where:

V_0 = the gas volume developed without sample (ml);

V_1 = the gas volume developed from sample (ml);

T = the room temperature (K);

P = the environmental barometric pressure (mm Hg);

$P_{\text{H}_2\text{O}}$ = the vapour pressure at the temperature T (mm Hg);

M_c = the mass sample (g);

V_{ass} = CO_2 volume that was adsorbed in the reagent (ml).

3.3.5. OPTICAL MICROSCOPY

Preliminary optical microscopy (OM) observations both on polished thin sections and juvenile clasts (white pumice and black grey scoria) were conducted. Mineralogical and lithological features of UTGVT were studied using a Nikon Eclipse E600 POL binocular polarizing microscope.

Thin sections were realized at “Massimo Sbrana - Servizi per la Geologia” laboratory, on sample reduced in size and cut by a diamond blade.

The sample obtained was polished using a disc sander with horizontal plate, afterwards it was pasted on glass-slide through epoxy resin bicomponent and was left to create a polymeric compound for at least 24h.

The excess thickness of sample was taken away with a cut-back; then the thickness was further reduced until to obtain a 80 μm thick. Finally the polishing of thin sections was carried out on sander with horizontal plate.

3.3.6. SCANNING ELECTRON MICROSCOPY (SEM)

A careful SEM observations, carried out on a large number of samples, provide further information on authigenic minerals. SEM allowed to obtain tridimensional image at high resolution ($\sim 100 \text{ \AA}$), through the scanning a small area of sample test by an electron beam. Primary electrons (0.5-30 kV), interact with the surface of sample generating secondary electrons with lower energy. The intensity of these secondary electrons is connected to the topography surface of sample.

The presence of bright and dark areas, which gave tridimensional image, were associated to the intensity of secondary electrons, that was greater for the most superficial areas compared to the inner zones.

An image of sample's surface could be reconstructed by measuring the intensity of secondary electrons, estimated as a function of primary beam's position, during its scanning movement.

It was possible to obtain high resolution images because primary electrons could be focused on a point with size lower than 10 nm. The greater sensitivity to the external surface ($< 5 \text{ nm}$) was achieved using low intensity of primary beam ($< 1 \text{ keV}$). Primary electrons primarily generate secondary electrons but also produce backscattered electrons and X-rays as a result of interaction between the primary beam and the sample. Intensity of backscattered electrons could be correlated with atomic number of

elements, present in the area of the sample, and provide qualitative composition of the investigated area.

Analysis were carried out at “Centro di Servizio Interdipartimentale per Analisi Geomineralogiche” (CISAG) using a Jeol JSM 5310 scanning microscope equipped with energy dispersive spectroscopy (hereafter EDS) microanalysis system of Oxford Inca (figure 3.6).



Figure 3.6 : Jeol JSM 5310 scanning microscope and Oxford INCA EDS.

The analyzed samples were previously pasted on suitable metal stubs, and covered with a gold coating through an Agar Auto Coater 108 A, in order to ensure the electrical conductivity.

The EDS microanalysis system allowed to determine chemical composition, both qualitative and quantitative, of elements presents in the observed zone.

In order to perform quantitative chemical analysis X-EDS, sample must be polished and covered with graphite; results were obtained for comparison with international standard. Both polished thin sections and juvenile clasts and single crystals of zeolites, embedded in thermosetting bi-component resin (STRUERS EPOFIX RESIN) and suitably polished, were analyzed through EDS; it allow to calculate the chemical composition of each single mineralogical phase (chabazite, phillipsite, analcime and feldspar) and glassy fraction. EDS chemical analysis was considered reliable, measuring the percentage value of the error by means of the following formula (Passaglia, 1970):

$$E = \frac{Al + Fe^{III} - [Na + K + 2(Ca + Mg + Sr + Ba)]}{Na + K + 2(Ca + Mg + Sr + Ba)} \times 100$$

The maximum percentage of error satisfactory was set to 10%.

Dott. Gianmarco Rapisardo. Scuola di dottorato in Scienze della Natura e delle sue Risorse.
Indirizzo: Scienza e tecnologia dei Minerali e delle rocce di interesse industriale. XXV ciclo.
Post-emplacment minerogenetic processes in Upper Tufo Giallo della Via Tiberina (Latium): a
mineralogical and volcanological approach

EDS allow to obtain chemical analysis in terms of oxides (wt%); it has been calculate the unit cell content, too. In order to determine the number of atoms (for each investigated phase), chemical analyses of chabazite, phillipsite and analcime are normalized to 24, 32, 96 oxygen atoms, respectively; while the unit cell content of feldspar is calculated on 8 oxygens. Finally Barth's anhydrous standard cell content (normalized to 160 oxygens) of glasses are calculated (Barth, 1948).

3.3.7. PHASE CONCENTRATION

Basing on XRPD data the samples that had showed the highest percentage of phillipsite or chabazite were selected to carry out the zeolites enrichment

Samples were grinded and then sieved in the of 60-120 MESH size range, the powders were washed in deionized water in an ultrasonic tank (Ney 300 ultrasonik), in order to remove the clay fraction. Afterwards silic phases (feldspar, zeolites) were roughly separated from the femic phases, through Frantz's magnetic separator according to de' Gennaro and Franco (1979).

Finally, zeolites were separated, from the other silic phase, using a series of techniques based on the different physical behavior of the various constituents (Chipera et al., 1993).

3.3.8. THERMAL ANALYSIS

Zeolite-enriched samples were investigated through thermal analyses: thermogravimetry (TG), derivative thermogravimetry (DTG) and differential thermal analysis (DTA). Thermal analysis comprises a group of techniques in which a physical property of a substance is measured as a function of temperature, while the substance is subjected to a controlled temperature programme. The equipment of a thermoanalyzer consisted of: furnace, sample holder comprising thermocouples, sample containers and a ceramic or metallic block, temperature programmer, recording system. It could be distinguished in Thermogravimetry (TG), Derivative Thermogravimetry (DTG) and Differential Thermal Analysis (DTA).

TG was a technique by which, the weight of a substance, in an environment heated or a cooled controlled rate, was recorded as a function of time or temperature. TG gives absolute changes in sample weight so that the calculated extent of reaction was not affected by the heating rate used. DTG exploits the first derivative of the TG curve, it

allowed to determine the weight variation velocity of sample as a function of temperature .

DTA recorded the difference in temperature (ΔT), between a substance and a inert material (Corundum) against either time or temperature as the two specimens are subjected to identical temperature regimes in an environment heated or cooled at a controlled rate. The difference in temperature (ΔT) was a function of absorption or evolution of heat from the examined sample as a results of reactions. The absorption of heat was recorded graphically on DTA curves as a thermal minimum, which was equivalent of endothermic reaction (loss of material, structural collapse). While the evolution of heat was recorded graphically as a thermal maximum, that was equivalent of exothermic reaction (crystallization, oxidation).

These analysis were carried out with a Netzsch STA 409 Thermoanalyzer (100 mg of sample, which, before being analyzed, were dried at 60°C and maintained at constant humidity - 50%, heat rate = 10 °C to minute, atmosphere = room air) (figure 3.7).

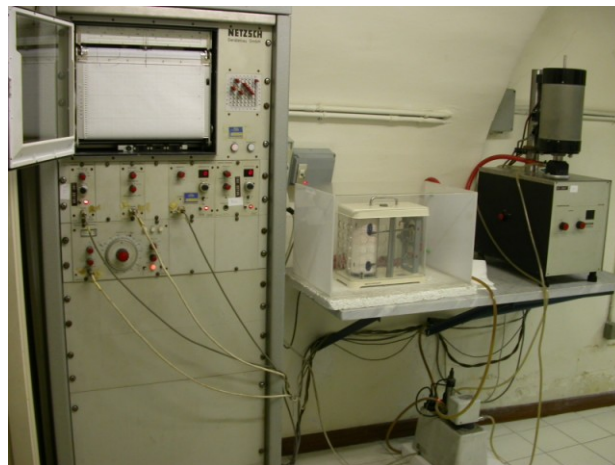


Figure 3.7: Netzsch STA 409 Thermoanalyzer.

3.3.9. TERMODINAMIC MODELLING

Thermodynamic modeling was carried out to calculate stability fields for an assemblage of a variety of zeolites, including chabazite, phillipsite, and analcime. Simulations used Geochemist's Workbench, Release 6.0 (RockWare) with Act2 used to plot diagrams (figure 3.8) and React modules used to calculate activity values with fixed T° (figure 3.9).

In order to calculate stability fields of zeolites, two parameters: silica and water activity are considered (Stumm and Morgan, 1981). Silica activity values range between: -2.7 for an amorphous silica and -3.7 for a quartz saturation; whereas for the water activity

values of 1; 0.99; 0.98 are suggested; the last one identifies sea water activity value. Because of water activity does not influence stability fields is used a water activity fixed to 1.

The software used an internal thermo database that requires a series of entries identified in Thermo datasets about all mineral phases existent in a determined system.

The data, needed to model the stability field for each phase, are: chemical composition, chemical formula, mole volume, species in reaction, activity values for eight temperatures °C (0, 25, 60, 100, 150, 200, 250, 300).

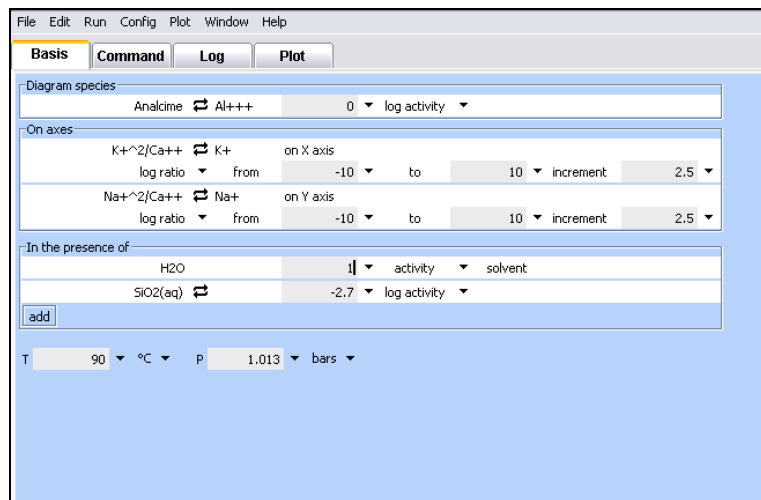


Figure 3.8: Act 2 module

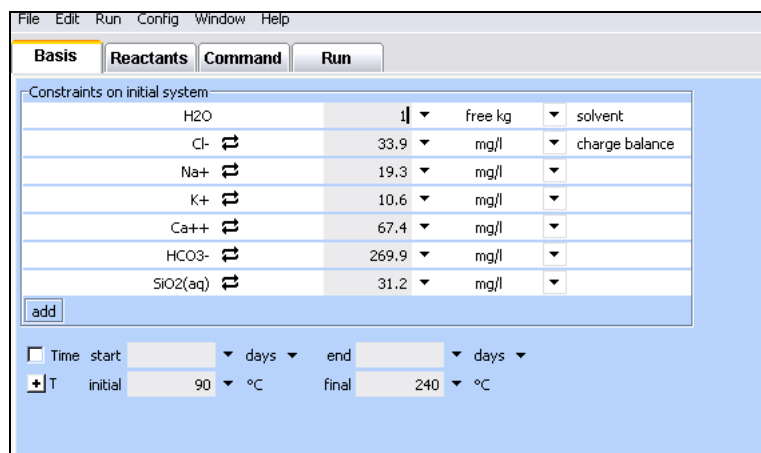


Figure 3.9: React module

3.4. PHYSICAL-MECHANICAL CHARACTERIZATION

In order to evaluate physic-mechanical features of TGVT specific gravity, open porosity, mercury porosimetry, water absorption, ultrasonic wave velocity, uniaxial strength and thermal dilatation were determined.

First of all, the traces of weathering were removed from all laboratory samples. Then a lot of sets of samples were obtained according to the testing methodologies recommended by technical norms (UNI EN).

3.4.1. HELIUM PYCNOMETRY

Specific gravity and open porosity were measured by helium pycnometry. Gas pycnometry is an analytical technique that uses a gas displacement method to measure two values of a porous solid: the true and the apparent density, from which it is possible to determine the total porous volume and the porosity. An inert gas, such as helium is used as the displacement medium.

The sample is sealed inside instrument compartment of known volume; the appropriate inert gas is admitted, and then expanded into another precision internal volume. The pressure was measured before and after expansion and is used to calculate the sample volume. Dividing this volume into the sample weight gives the gas displacement density. The true density (ρ_s) is given by:

$$\rho_s = m/v$$

where:

m: sample mass;

v: sample volume.

Specific gravity was determined with a He-pycnometer Micromeritics Multivolume Pycnometer 1305; figure 3.10), with an accuracy of 90.1–0.2 per cent on cylindrical samples (2,5 diameter, <3 cm height). Because of the high heterogeneity of the material, the test was carried out on five samples and, for each of them, at least three measures were performed. The measured apparent and real volumes allowed the open porosity to be calculated.



Figure 3.10: He-pycnometer Micromeritics Multivolume Pycnometer 1305

3.4.2. MERCURY INTRUSION POROSIMETRY (MIP)

Mercury intrusion porosimetry is a widely used technique to characterize the distribution of pore sizes in geomaterials. It was developed by Ritter e Drake in 1945 and allows to measure volume and size of both mesopores and macropores in porous solid materials (figure 3.11).

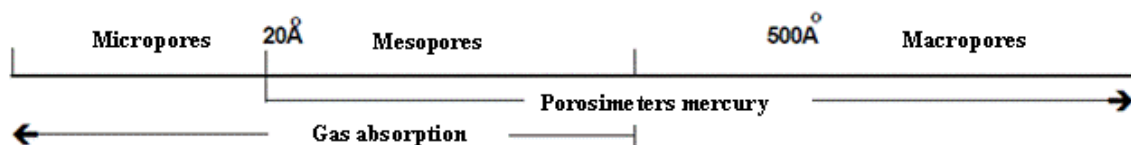


Figure 3.11: pore radii intruders by mercury porosimetry and helium pycnometry techniques.

It is based on the non-wetting liquid property of mercury (with contact angle greater than 90°).

It is a simple and quick indirect technique, but it has limitations when applied to materials that have irregular pore geometry. Mercury intrudes from the outside capillary under pressure. The relationship between the pressure and the pores diameter is defined by Washburn:

$$P = 2\gamma\cos\theta/ r$$

P: pressure (N/m^2);

γ : surface tension of mercury (N/M);

θ : contact angle of the mercury;

R: pore radii (μm);

The pore size distribution is determined by the volume intruded at each pressure increment. Total porosity is determined by total volume intruded.

The MIP technique is widely used because of its easy. However, it does not measure the true distribution of sizes for some pore geometries. For these systems, large internal pores are accessible by very narrow throats. The MIP technique misrepresents the size of these pores as having the diameter of their throats. This bias is referred to as the "ink bottle" effect.

Pore size distribution was measured by Thermo Finnigan Pascal 140 240 e 440 (figure 3.12). They operate at maximum pressure of 400 Mpa and are able to investigate pore radii between 58000 and 1900 nm. Data were processed through the Pascal *software* able to determine the relationships between the pressure applied by the mercury and the pore volume (assumed size round) in the sample analyzed.



Figure 3.12: Mercury porosimeters Thermo Finnigan 140, 240, 440.

3.4.3. TOTAL ABSORPTION WATER (UNI EN 13755)

Further information on the porosity of the rocks have been obtained by the determination of water absorption. Water absorption by total immersion tests revealed the high attitude of material in allowing fluid circulation linked to the occurrence of a net of interconnected pores.

Water absorption test allows to determine the maximum amount of water absorbed by stone.

The total absorbed water after immersion (in deionized water) at room temperature and pressure was estimated according to the procedure reported in UNI EN 13755.

Samples were dried inside an oven to constant mass at temperature of 60°C. Immediately upon cooling, the specimens are weighed. Then they are placed into a tub and immersed in deionized water (figure 3.13); samples were buffered with a cloth dump and weight with an accuracy of 0.01g at regular step time.



Figure 3.13: TGVT samples during total absorption water test

The amount of water absorbed by TGVT is given by ratio of the weight of water absorbed by samples ($m_s - m_d$), to the weight of the dry materials:

$$A_b = ((m_s - m_d) / m_d) * 100$$

where:

A_b : water absorption at atmospheric pressure;

m_s : mass of saturated sample;

Dott. Gianmarco Rapisardo. Scuola di dottorato in Scienze della Natura e delle sue Risorse.
 Indirizzo: Scienza e tecnologia dei Minerali e delle rocce di interesse industriale. XXV ciclo.
 Post-emplacement minerogenetic processes in Upper Tufo Giallo della Via Tiberina (Latium): a
 mineralogical and volcanological approach

m_d : mass of dried sample.

3.4.4. ULTRASONIC WAVE (UNI-EN 14579)

Further information on texture and fabric of the rocks (lithics, clast and pumice concentration) of rock can be obtained by ultrasonic velocity test (UNI EN 14579).

Ultrasonic velocity test is performed by a Boviari UTD 1400 ultrasonic digital non destructive test was using with a pair of 55-kHz transducers, in direct arrangement (figure 3.14). Ultrasonic pulses were read out on the digital display, to an accuracy of 90.1 ms. To provide an adequate acoustic coupling between the rock specimen and the transducers, a thin film of hydro-soluble gel was used; to enhance energy transmission, the transducers were firmly hand-pressed onto the specimens.



Figure 3.14: Instrument Boviari UTD 1400 for ultrasonic wave velocity measure

Measurements were carried out along three spatial directions of the cubic samples (7 cm).

Ultrasonic wave can be calculated by the formulae:

$$V = \frac{L}{T}$$

where:

V: pulse velocity (m/s);

Dott. Gianmarco Rapisardo. Scuola di dottorato in Scienze della Natura e delle sue Risorse.
 Indirizzo: Scienza e tecnologia dei Minerali e delle rocce di interesse industriale. XXV ciclo.
 Post-emplacement minerogenetic processes in Upper Tufo Giallo della Via Tiberina (Latium): a
 mineralogical and volcanological approach

L: length of the sample (m);

T: the time used by the impulse to pass through the specimen (μs).

3.4.5. UNIAXIAL COMPRESSIVE STRENGTH (UNI-EN 11926)

UCS is one of the most important parameters of rock strength. Test allows to determine rock resistance against crushing stresses. Previous studies conducted on the mechanical properties of volcanic tuffs have shown a linear relationship between porosity and uniaxial compressive strength (Evangelista et al., 2000; Langella et al., 2002; Bear et al., 2009).

It was carried out according to the procedure reported UNI EN 11926, using cubic samples (70 mm in size). Before each test density rock was determined.

The testing device (Controls C5600; figure 3.15) allowed a maximum load of 3000 kN.

The axial load was increased continuously at a rate within the limits of 0.5–1.0 MPa/s.

The maximum load and deformations were recorded by means of a data-acquisition system.

Uniaxial Compressive strength (R, MPa) was defined by:

$$R = \frac{F}{A}$$

F: breaking load (N);

A: cross section area of the specimen (mm^2).



Figure 3.15: Controls C5600 frame used for uniaxial compressive strength test

3.4.6. LINEAR THERMAL EXPANSION COEFFICIENT (UNI-EN 14581)

This test allows to understand the thermal behaviour of natural stones by mechanical length change measurements. Thermal dilatation tests were carried out according to the UNI EN 14581 on five prismatic specimens (length 25 cm, wide 5 cm and thick 2,5 cm) for each facies.

The test were carried out by using a mechanical measuring device (LONOS TEST) interfaced to a personal computer using software THERMO TEST (figure 3.16).



Figure 3.16: Mechanical measuring device (LONOS TEST) for measurement of the linear coefficients of thermal expansion.

The specimens were dried to constant mass and then they are equipped with two rivets along their longitudinal axis (at a distance of 200 mm); this rivets were connected through spikes to the measurement device. Finally the device was placed inside a chamber at a temperature of 20 °C.

The expansion/contraction values were recorded at increasing temperature of 20°, 40°, 60°C according to the follow formulae:

$$\varepsilon = \frac{\Delta L}{L_{20}}$$

in mm/mm, where $\Delta L = L_{80} - L_{20}$ that is the difference of sample length recorded at 20° C and 80° C.

The linear coefficients of thermal expansion were measured according to formulae:

$$\alpha = \frac{\varepsilon}{\Delta T}$$

They recorded the unit change for each centigrade degree of temperature variation (mm / mm ° C) along that same direction.

4. RESULTS

In the early phase of present research, a geo-volcanological characterization of UTGVT formation is carried out. The field data allow to show the stratigraphic differences within the deposit, linked to emplacement mechanism (thickness, occurrence of different eruptive units and juvenile components). The investigations along several quarries, allow to distinguish three flow units (a, b, c), which made up the UTGVT formation. The lowermost units (a, and b) show similar features; they are made up of yellowish lithified massive cineritic layer, they are overcome by an un-welded cineritic deposit. These flow units are associated with the emission of products from the inner and middle part of magma chamber; these products are characterized by white pumice clasts highly vesiculated, vitrophyric, and contain scarce feldspar and clinopyroxene crystals. The uppermost unit, c, is made up of un-welded layer with pumice rich layers. The UTGVTc flow unit is associated to the emission of products from the peripheral portion of reservoir; these products are characterized by black-grey scoria clasts, which are poorly vesiculated, highly crystallized, and contain diffuse leucite phenocrysts. Along several investigated outcrops, the thickness of units is not constant. Whenever formation reaches high thickness no clear evidence of the presence of different flow units can be pointed out; probably the discontinuity layers between units were erased from the subsequent flow unit. Field investigation also allows to identify the occurrence of an eruptive mechanism linked to magma-water interaction. The occurrence of layers with accretionary lapilli indicates that the emplacement temperature was very close to the water condensation point; this could be linked to pre-eruptive magma-water interaction (de' Gennaro et al., 2000). It is well known that magma-water interaction favored the minerogenesis of authigenic minerals.

Field data were supported by laboratory physical analyses; samples of non-lithified facies were investigated in order to characterize volcanological features through grain size and component analysis.

4.2. PHYSICAL ANALYSES

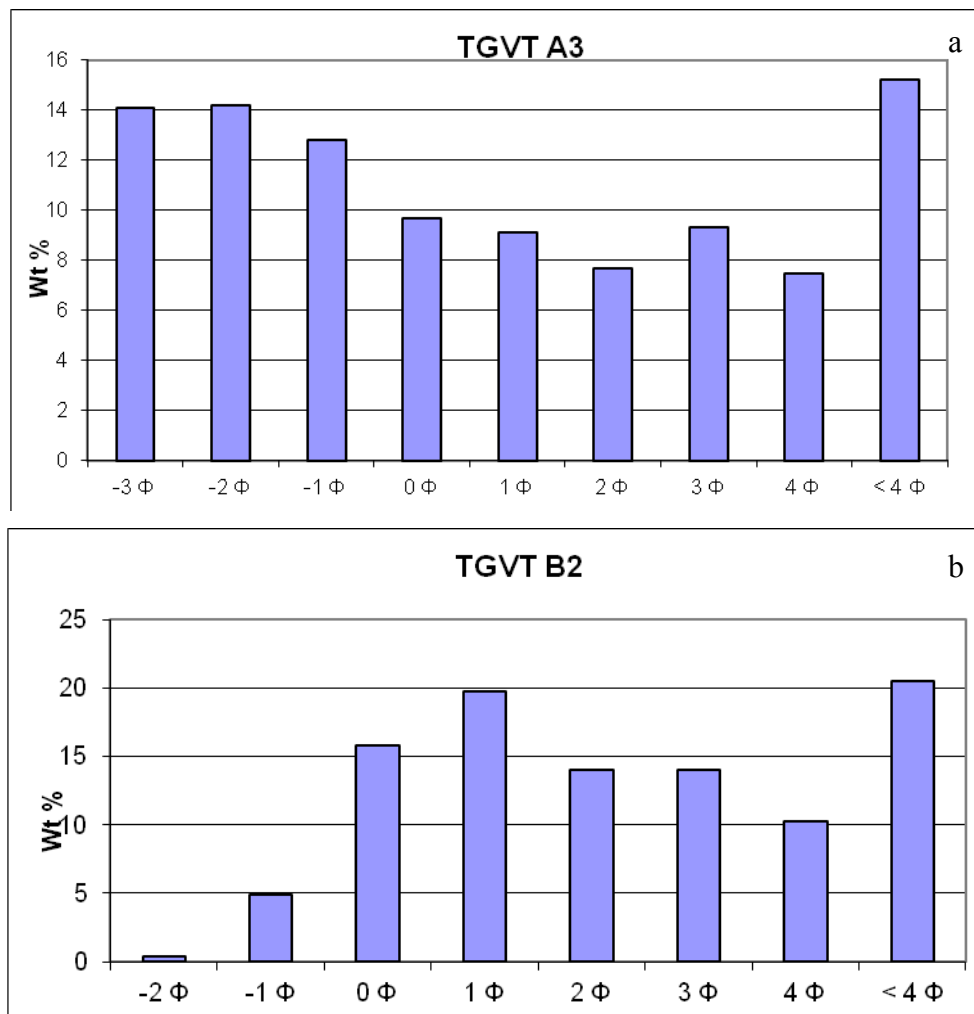
The histograms of weight percentage for each grain size class were constructed from the grain-size data. The pyroclastic deposit, in fact, has an overall distribution, which results from the combined distribution of each component.

The relative proportion of different lithological components in a pyroclastic deposit reflects its way of formation and supplies information on the transport process.

The ultimate reason why we carried out grain-size and lithological component analysis on the loose fractions of TGVT was to investigate which kind of juvenile fragments made up the pyroclastic deposits, and to separate some well preserved juvenile clasts for SEM-EDS chemical analysis.

4.2.1. GRAINSIZE ANALYSIS

Grainsize data are reported as histograms of weight percent components: the A3 sample is polymodal, poorly sorted, and the distribution has a coarse tail. The B2 and B2 bis samples are unimodales and poorly sorted (figure 4.1). As a matter of fact, in all the samples a huge percentage of material finer than 4phi is present, and the real grain-size distribution would have requested the analysis (through density or photo-sedimentographic methods) of the fine tails.



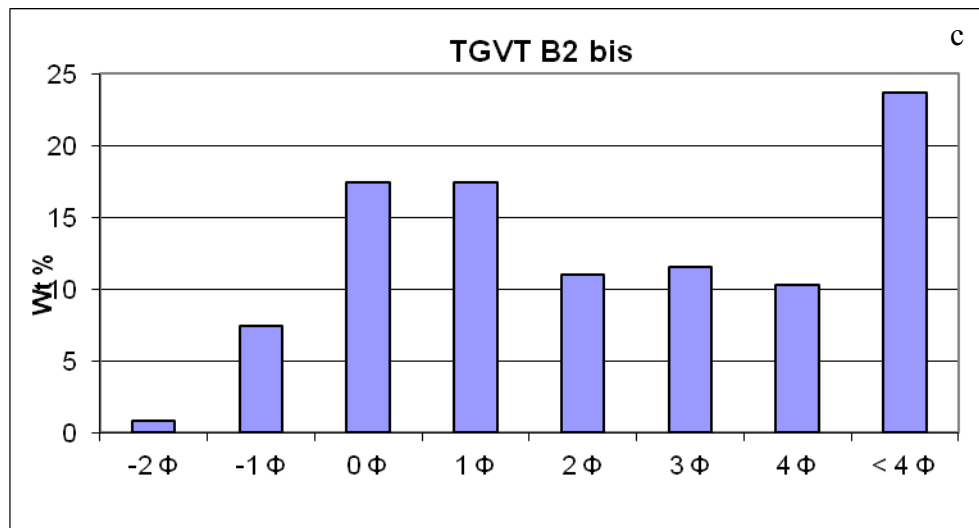


Figure 4.1: Histograms (a, b, c) of weight percent components for each intervals size.

In table 4.1 are reported the grainsize parameters for the three un-welded samples derived grafically from cumulative curves.

Table 4.1: Inman parameters

Sample	MdΦ	$\sigma\Phi$	$\alpha\Phi$
A3	-0,8	3,3	0,54
B2	1,6	2,55	1,13
B2 bis	1,5	2,55	1,01

The A3 sample components has a 2mm size of median diameters, while samples B2 and B2 bis have 0,5 mm size of median diameters.

The sorting values, ranging between 2.55 Φ and 3.3 Φ, made it possible to classify these three samples as poorly sorted pyroclastic deposit.

4.2.2. COMPONENT ANALYSIS

The results of component analysis are reported as histograms of components for each size class, range between -3Φ and 3Φ (figure 4.2 a, b, c).

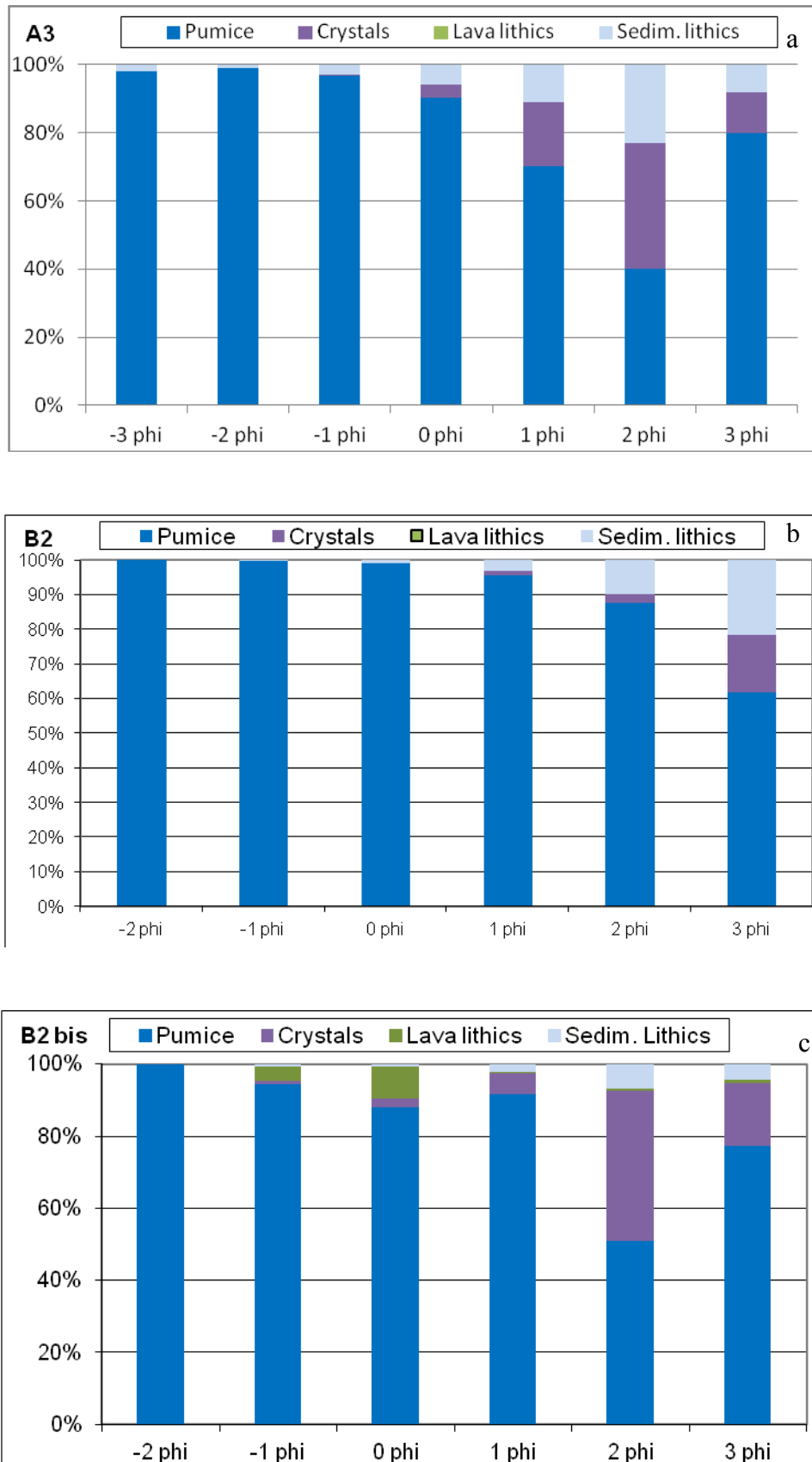


Figure 4.2: Histograms of components for each size class.

On the whole, a cineritic patina covered the single grains in all the samples and they presented many cineritic aggregates, due to the ash aggregation during the transport phases. These aggregates were not disaggregated by the drying and sieving procedures; this is the reason why the samples were washed in an ultrasonic tank for 15m before the lithological component analysis under the binocular microscope. Many aggregated survived also to this treatment, testifying to a slight cementation of the finer fractions.

The A3 sample has about 5 wt% of limestone clasts in larger size classes, and their weight percentage increases in the finer grain-size classes. Crystals grains were mainly made up of feldspars, and about 30 wt% of feldspar can be observed in 2 Φ size class.

The B2 sample is made up of pumice fragments up to more than 60 wt% in overall size classes. Limestone and crystals fragments can be observed in the finest size classes, and reach the higher weight percent (ca 18 wt%) in 3 Φ size. Both in A3 and B2 sample lava fragments are not observed.

The B2 bis sample has juvenile clasts as mainly component (> 50 wt%), crystal grains and sedimentary clasts in the finest classes. Crystals display a weight percent higher than 40% in 2 Φ class size, while the sedimentary clasts range between 2-8 wt%, from 1 Φ to 3 Φ size classes. In this sample, however, limestone fragments reach ca 1 wt% also in -1 Φ and 0 Φ size classes. Lava lithics, found in -1 Φ and 0 Φ size class, range between 5-10 wt%.

The reason why we carried out grain-size and lithological component analysis was to investigate which kind of juvenile fragments made up the UTGVT pyroclastic deposits, and to separate some well preserved juvenile clasts for SEM-EDS chemical analysis. Binocular microscope observation made it possible to point out the presence of two kinds of juvenile clasts classes: whitish pumice and black-grey scoria (figure 4.3).

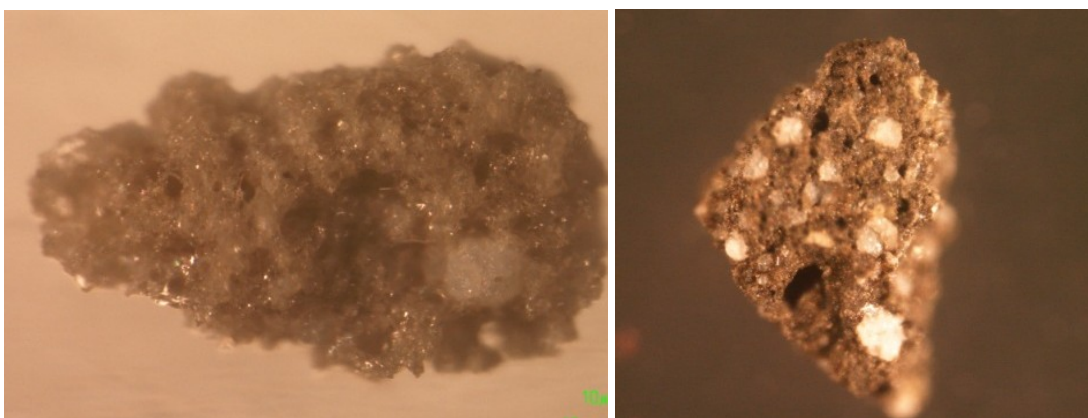


Figure 4.3: Binocular microscope photograph: on the left white pumice, on the right black-grey scoria.

White pumice is characterized by an aphyric texture, vitrophyric groundmass and moderate vesicularity.

Black–grey scoria shows low vesicularity, highly crystalline groundmass and abundant phenocrysts. Leucite is the most abundant phenocryst phase, followed by pyroxene, scarce sanidine and rare mica-biotite.

The weight percentage of the single type of pumices in the various classes is hard to be quantified, mainly because of the presence of ash aggregates. By visually comparing the juvenile fraction content in the three investigated samples, however, it is possible to stress that white pumices are, on the whole, more abundant in the coarser grain-size classes and in A3 with respect to the other samples.

4.3. MINERALOGICAL-PETROGRAPHICAL CHARACTERIZATION

The second phase of the research has provided the mineralogical and petrographical characterization by means of the following analyses: X-ray powder diffraction (XRPD) for all collected samples, X-ray fluorescence (XRF) of bulk rocks, calcimetry, optical microscopy (OM), scanning electron microscope analyses (SEM) and energy-dispersive spectrometry (EDS).

4.3.1. X-RAY POWDER DIFFRACTION (XRPD)

The XRPD data shows that samples are constituted by the following mineralogical phases: feldspars, calcite, mica-biotite, clay minerals (smectite) and zeolites such as chabazite, phillipsite and analcime. Analcime is present only in samples belonging to km 12.7-13 and Cannetaccio quarries.

Afterwards are reported the quantitative mineralogical data, divided for single quarry.

km 13 quarry

Welded facies of UTGVTa and UTGVTb units are deeply zeolitized, and their total zeolites content ranges between 43-51 wt%, with chabazite largely exceeding phillipsite and analcime. Samples of lithified facies show a smectite content between 12-16 wt%. Samples from discontinuities a-b, b-c and sub-unit c are characterized by analcime as the most abundant zeolites, and smectite ranges between 1-18 wt%. This samples are characterized by an high amorphous content (> 50 wt%).

Samples belong to km 13 show a feldspars content between 4-20wt%; calcite content is almost constant with values between 12-16 wt% (sub-unit a and b), whereas calcite is not found in unwelded facies (B2, B2 bis) and in sub-unit c (C1).

UTGVTc unit shows the highest content of analcime (21 wt%).

Table 4.2: Mineralogical content of samples as determined by XRD using RIR (reference intensity ratio) method (km 13 quarry)

Sample	Smectite [%]	Biotite [%]	Chabazite [%]	Phillipsite [%]	Analcime [%]	Feldspar [%]	Calcite [%]	Total [%]	Amorphous [%]
A1	16 (± 2)	0	37 (± 2)	4 (± 1)	2 (± 1)	4 (± 1)	13 (± 1)	77 (± 8)	23
A2	12 (± 2)	0	43 (± 2)	6 (± 1)	1 (± 1)	5 (± 1)	15 (± 1)	83 (± 8)	17
A3	tr	tr	0	2 (± 1)	16 (± 1)	7 (± 2)	12 (± 1)	39 (± 5)	61
B1	13 (± 2)	0	39 (± 2)	2 (± 1)	10 (± 1)	6 (± 1)	16 (± 1)	85 (± 8)	15
B2	18 (± 3)	0	0	4 (± 1)	14 (± 1)	16 (± 4)	0	50 (± 9)	50
B2 bis	3 (± 1)	0	0	2 (± 1)	17 (± 1)	20 (± 4)	0	42 (± 7)	58
C1	1 (± 1)	0	0	3 (± 1)	21 (± 1)	12 (± 3)	0	37 (± 5)	63

Error in brackets = $\sqrt{\sigma_1^2 + \sigma_2^2 + \dots}$ (Chipera and Bish, 1995), amorphous % by difference

km 12.7 quarry

All samples of km 12.7 quarry belong to the welded facies of UTGVTa; they have a feldspars content that never exceeds 3 wt%, calcite is almost constants, with values between 12-14 wt%. This section is deeply zeolitized with a chabazite content >40 wt%, which is the most abundant zeolite followed by phillipsite, with content of about 4%, and traces of analcime ≤ 1 wt%. All samples show an almost constant smectite content (about 14 wt%) (table 4.3).

Table 4.3: Mineralogical content of samples as determined by XRD using RIR (reference intensity ratio) method (km 12.7 quarry)

Sample	Smectite [%]	Chabazite [%]	Phillipsite [%]	Analcime [%]	Feldspar [%]	Calcite [%]	Total [%]	Amorphous [%]
CTP 1	16 (± 2)	45 (± 3)	4 (± 1)	1 (± 1)	3 (± 1)	12 (± 1)	81 (± 9)	19
CTP 2	15 (± 2)	44 (± 2)	4 (± 1)	tr	3 (± 1)	12 (± 1)	79 (± 7)	21
CTP 3	12 (± 2)	46 (± 3)	3 (± 1)	tr	3 (± 1)	14 (± 1)	78 (± 8)	22
CTP 4	14 (± 2)	48 (± 3)	3 (± 1)	tr	3 (± 1)	13 (± 1)	82 (± 8)	18
CTP 5	12 (± 2)	47 (± 3)	3 (± 1)	tr	4 (± 1)	13 (± 1)	80 (± 8)	20

Error in brackets = $\sqrt{\sigma_1^2 + \sigma_2^2 + \dots}$ (Chipera and Bish, 1995), amorphous % by difference

Samples from km 13 and km 12.7 quarries are grouped in a single section, in order to observe the vertical variation of mineralogical phases along the sampling section (figure 4.4).

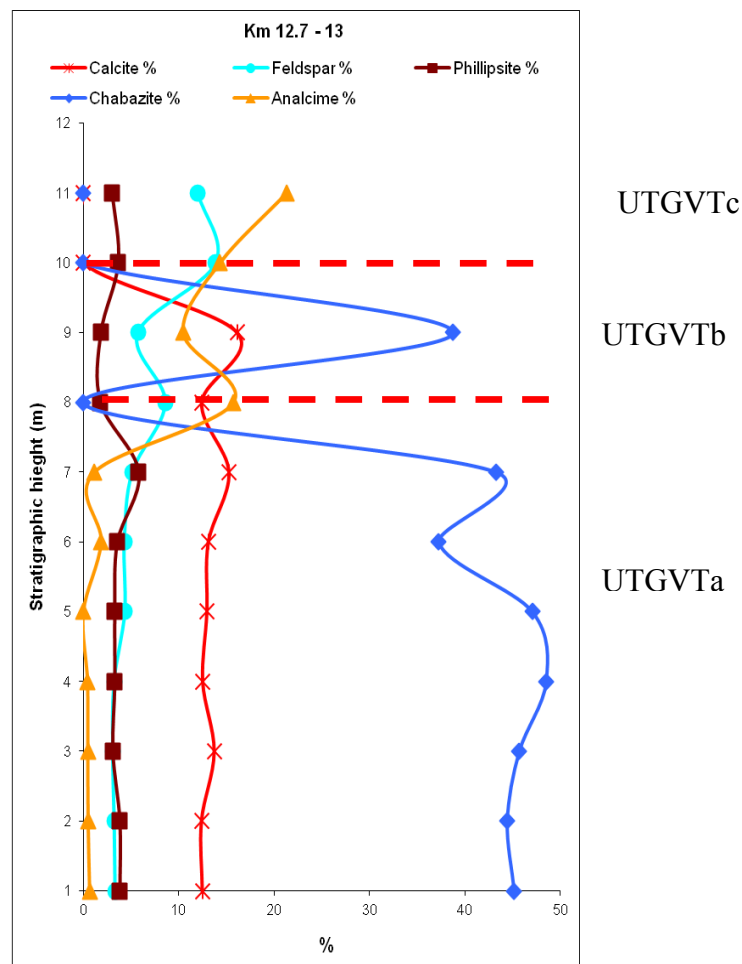


Figure 4.4: Reconstructed stratigraphy of samples from Km 12.7 and Km 13 quarries with the vertical variations of the main mineralogical phases. The red dotted line indicate the position of discontinuity between sub-unit a to b, and b to c. As regard to stratigraphic height, from 1m to 8m correspond to UTGVTa unit, from 8m to 10m correspond to UTGVTb, up to 10m correspond to UTGVTc.

The occurrence of chabazite and phillipsite, within the UTGVTa and UTGVTb suggests suitable temperatures for zeolitization by interaction of fresh glass with water; the water can be attributed to the eruptive mechanism (phreatomagmatic), but also to paleo-Tiber river and meteoric waters, as shown by field evidences. The prevalence of chabazite suggests a chemical composition of glass and solution that favored crystallization of this zeolite, suggesting a calcium-potassic environment. The occurrence of smectite in all investigated samples could be due to an initial acidic environment which altered the glass. This acidic solution interact with calcite, thereby causing a buffer effect on the system with hydrolysis and dissolution of the glassy fraction. Probably the chemical composition of glass, and the Ca-rich solution favored the chabazite crystallization. The uppermost unit UTGVTc, showing absence of chabazite and low content of phillipsite,

suggest un-suitable temperature for zeolitization; this unit was cooled soon after emplacement; its high content of analcime is due to higher content of black-grey scoria emitted from the most peripheral TGVT magma chamber (Masotta et al., 2010). The juvenile clasts are made up of leucite crystals, that interacting with a Na-rich solution favored the analcimization of leucite (Giampaolo and Lombardi, 1994).

The feldspar content of km 13-12.7 samples can be attributed to a primary phase.

SICAT quarry

The upper portion of the outcrop that likely represents the gradational vertical contact between the UTGVTb and UTGVTc units, was not sampled as it was inaccessible, therefore only three sample of UTGVTb unit are here available.

Table 4.3 summarizes the quantitative evaluation of mineralogical composition from SICAT quarry. Samples show a wide range of feldspars between 8-27wt.%, and calcite content is variable between 8 and 14wt.%. In this quarry is observed an higher of total zeolites content (47-70wt.%) than samples from km12.7 and km 13 quarries, though they are lacking in analcime. Chabazite is the most abundant zeolite, with a wide range between 40 and 62 wt%, followed by phillipsite (6-20wt.%). The higher zeolite content compared to km13-12.7 outcrops, can be related to the higher thickness of units; this condition favoured suitable temperature for zeolitization process. The C3_3 sample show a very high feldspar content; it could be attributed to an evolution of the zeolitization process towards more stable phase. Samples have a smectite content between 6-9 wt%.

UTGVTb flow unit is associated to the emission of products from inner portion of the magma chamber, characterized by rare leucite phenocrysts. Thus the absence of analcime in this section, could be attributed to the absence of primary leucite within the flow unit.

Table 4.4: Mineralogical content of samples as determined by XRD using RIR (reference intensity ratio) method (SICAT quarry)

Sample	Smectite [%]	Chabazite [%]	Phillipsite [%]	Feldspar [%]	Calcite [%]	Total [%]	Amorphous [%]
C3_1	9 (± 1)	62 (± 3)	8 (± 1)	8 (± 1)	8 (± 1)	96 (± 7)	4
C3_2	6 (± 1)	40 (± 2)	20 (± 1)	11 (± 2)	14 (± 1)	91 (± 7)	9
C3_3	9 (± 1)	41 (± 2)	6 (± 1)	27 (± 3)	9 (± 1)	92 (± 8)	8

Error in brackets = $\sqrt{\sigma_1^2 + \sigma_2^2 + \dots}$ (Chiperia and Bish, 1995), amorphous % by difference

Perina quarry

In a early phase of the research, samples of UTGVTa flow unit were collected from both two sites and two walls of quarry. Two samples, belong to two sites (C2_P1_1 and C2_P2_1), have quantitative mineralogical data very similar; both have a feldspar content of 23 wt%, calcite is between 16 wt% and 18 wt%, chabazite and phillipsite contents are between 34-36 wt.% and 6-8 wt.% respectively. However, with regard to samples belong to quarry fronts (C2_P1_2 and C2_P2_2), they have a similar feldspar content of about 8-9wt.%, while calcite is between 8% and 14wt.%. The total zeolites content range between 53 and 67wt.%, chabazite is between 43 and 55wt.%, while phillipsite is about 10-12 wt.%. In this samples smectite ranges between 8-18 wt%, and analcime is absent.

Table 4.5 reports the quantitative mineralogical data of aforementioned samples.

Table 4.5: Mineralogical content of samples as determined by XRD using RIR (reference intensity ratio) method (Perina quarry)

Sample	Smectite [%]	Biotite [%]	Chabazite [%]	Phillipsite [%]	Feldspar [%]	Calcite [%]	Total [%]	Amorphous [%]
C2_P1_1	8 (± 1)	tr	36 (± 2)	8 (± 1)	23 (± 4)	18 (± 1)	93 (± 9)	7
C2_P1_2	18 (± 3)	tr	43 (± 2)	10 (± 1)	8 (± 3)	14 (± 1)	92 (± 10)	8
C2_P2_1	10 (± 1)	tr	34 (± 2)	6 (± 1)	23 (± 4)	16 (± 1)	89 (± 9)	11
C2_P2_2	11 (± 2)	tr	55 (± 2)	12 (± 1)	9 (± 3)	8 (± 1)	95 (± 9)	5

Error in brackets = $\sqrt{\sigma_1^2 + \sigma_2^2 + \dots}$ (Chipera and Bish, 1995), amorphous % by difference

Among the set of investigated quarries, Perina quarry resulted the most suitable to perform a vertical sampling along a front, collecting 1 m spaced samples. Samples collected during the vertical sampling have different quantitative mineralogical composition (table 4.6). They have a wide range content of feldspar between 12 and 37wt.%. Many samples have a constant calcite content range between 10-15wt.%, while just three samples show a content higher than 15 wt.%. Zeolites content has a wide range, the upper and lower part of the quarry front have chabazite as the main zeolite, with range between 14-37 wt.% and 23-47 wt.% respectively, while four samples in the central part of the wall show prevalent phillipsite, with range between 29 and 40 wt.%. The whole samples are characterized by the absence of analcime. Samples of vertical sampling are characterized by wide range of smectite content between (2-16 wt%).

Table 4.6: Mineralogical content of samples from vertical sampling (Perina quarry) as determined by XRD using RIR (reference intensity ratio) method

Sample	Smectite [%]	Biotite [%]	Chabazite [%]	Phillipsite [%]	Feldspar [%]	Calcite [%]	Total [%]	Amorphous [%]
CV_1	9 (± 1)	tr	35 (± 2)	10 (± 1)	19 (± 2)	12 (± 1)	80 (± 7)	20
CV_2	10 (± 1)	tr	20 (± 1)	7 (± 1)	22 (± 3)	15 (± 1)	75 (± 7)	25
CV_3	9 (± 1)	tr	14 (± 1)	5 (± 1)	24 (± 4)	18 (± 1)	70 (± 8)	30
CV_4	8 (± 1)	tr	20 (± 1)	5 (± 1)	24 (± 4)	15 (± 1)	73 (± 8)	27
CV_5	13 (± 1)	tr	28 (± 2)	6 (± 1)	30 (± 5)	11 (± 1)	88 (± 10)	12
CV_6	12 (± 3)	tr	29 (± 2)	8 (± 1)	24 (± 4)	14 (± 1)	86 (± 11)	14
CV_7	12 (± 2)	tr	29 (± 2)	7 (± 1)	17 (± 3)	14 (± 1)	80 (± 9)	20
CV_8	6 (± 1)	tr	34 (± 2)	9 (± 1)	21 (± 3)	14 (± 1)	85 (± 8)	15
CV_9	5 (± 1)	tr	30 (± 2)	6 (± 1)	15 (± 2)	17 (± 1)	74 (± 7)	26
CV_10	5 (± 1)	tr	24 (± 1)	7 (± 1)	19 (± 3)	17 (± 1)	72 (± 7)	28
CV_11	10 (± 1)	tr	31 (± 2)	11 (± 1)	15 (± 2)	13 (± 1)	80 (± 8)	20
CV_12	2 (± 1)	tr	37 (± 2)	11 (± 1)	13 (± 2)	10 (± 1)	73 (± 7)	27
CV_13	9 (± 1)	tr	39 (± 2)	15 (± 1)	13 (± 5)	11 (± 1)	88 (± 10)	12
CV_14	7 (± 1)	tr	29 (± 2)	13 (± 1)	15 (± 2)	13 (± 1)	78 (± 7)	22
CV_15	8 (± 1)	tr	28 (± 2)	22 (± 1)	12 (± 2)	13 (± 1)	84 (± 7)	16
CV_16	2 (± 1)	tr	17 (± 1)	35 (± 2)	14 (± 6)	14 (± 1)	82 (± 10)	18
CV_17	4 (± 1)	tr	11 (± 1)	40 (± 2)	18 (± 8)	11 (± 1)	84 (± 13)	16
CV_18	7 (± 1)	tr	16 (± 1)	31 (± 1)	13 (± 6)	13 (± 1)	79 (± 10)	21
CV_19	10 (± 2)	tr	26 (± 1)	29 (± 1)	17 (± 6)	10 (± 1)	92 (± 11)	8
CV_20	3 (± 1)	tr	28 (± 2)	26 (± 1)	16 (± 6)	12 (± 1)	85 (± 11)	15
CV_21	7 (± 1)	tr	39 (± 2)	16 (± 1)	18 (± 6)	10 (± 1)	90 (± 11)	10
CV_22	8 (± 1)	tr	41 (± 2)	11 (± 1)	20 (± 7)	14 (± 1)	93 (± 12)	7
CV_23	8 (± 1)	tr	47 (± 3)	12 (± 1)	14 (± 5)	8 (± 1)	89 (± 11)	11
CV_24	7 (± 1)	tr	46 (± 3)	9 (± 1)	23 (± 4)	10 (± 1)	95 (± 10)	5
CV_25	5 (± 1)	tr	43 (± 2)	4 (± 1)	16 (± 6)	15 (± 1)	83 (± 11)	17
CV_26	5 (± 1)	tr	37 (± 2)	9 (± 1)	22 (± 8)	15 (± 1)	89 (± 13)	11
CV_27	8 (± 1)	tr	43 (± 2)	9 (± 1)	21 (± 8)	12 (± 1)	93 (± 13)	7
CV_28	11 (± 2)	tr	38 (± 2)	6 (± 1)	25 (± 5)	11 (± 1)	91 (± 11)	11
CV_29	7 (± 1)	tr	28 (± 2)	7 (± 1)	22 (± 7)	11 (± 1)	74 (± 12)	26
CV_30	7 (± 1)	tr	30 (± 2)	4 (± 1)	34 (± 5)	14 (± 1)	90 (± 10)	10
CV_31	5 (± 1)	tr	27 (± 1)	3 (± 1)	34 (± 5)	15 (± 1)	84 (± 9)	16
CV_32	16 (± 2)	tr	27 (± 2)	3 (± 1)	37 (± 6)	12 (± 1)	96 (± 12)	4
CV_33	12 (± 2)	tr	23 (± 1)	3 (± 1)	35 (± 7)	14 (± 1)	88 (± 12)	12
CV_34	9 (± 1)	tr	24 (± 1)	3 (± 1)	27 (± 4)	12 (± 1)	75 (± 8)	25
CV_35	13 (± 2)	tr	32 (± 2)	4 (± 1)	30 (± 5)	13 (± 1)	92 (± 11)	8
CV_36	9 (± 1)	tr	28 (± 2)	7 (± 1)	23 (± 3)	12 (± 1)	79 (± 8)	21
CV_37	8 (± 1)	tr	29 (± 2)	3 (± 1)	20 (± 7)	12 (± 1)	73 (± 12)	27
CV_38	16 (± 2)	tr	30 (± 2)	2 (± 1)	27 (± 5)	13 (± 1)	88 (± 11)	12

Error in brackets = $\sqrt{\sigma_{12} + \sigma_{22} + \dots}$ (Chipera and Bish, 1995), amorphous % by difference

In order to better overview the vertical variation of feldspar, calcite, chabazite and phillipsite content along the quarry front, the quantitative mineralogical data are reported in figure 4.5.

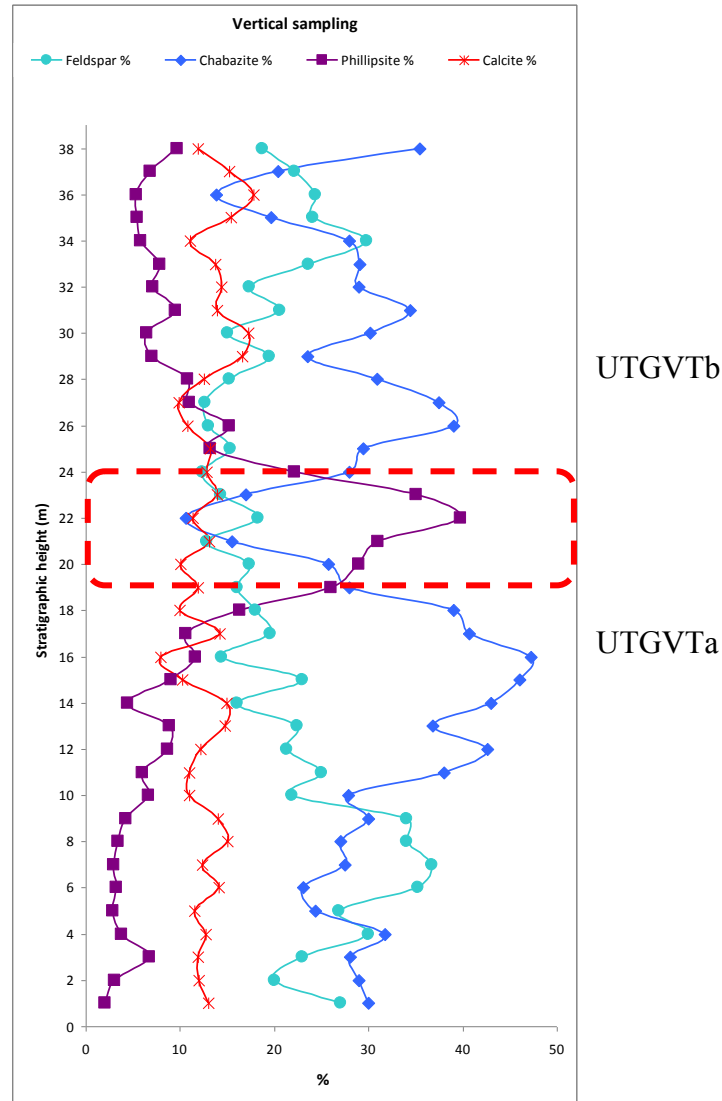


Figure 4.5: Vertical variation of feldspar, calcite and zeolitic minerals: chabazite, phillipsite. In figure the red dotted zone indicate the level that distinguish the UTGVTb unit from UTGVTa unit.

Along this outcrop, as seen at km13-12.7 reconstructed section, the UTGVTa and UTGVTb units confirms a calcitic-potassic environment that favoured the crystallization of chabazite. The middle part of the wall, with prevailing phillipsite, could identify a level that distinguish the UTGVTa unit from UTGVTb unit; along this wall stratigraphic evidence are not clear. The high feldspar content could suggest that high thickness (and preserved temperature for a long time) led to an initial feldspatization process. Figure 4.5 shows that as chabazite content decreases, feldspar

percentage increases and vice-versa, this relationship suggests that authigenic feldspar has been formed at the expense of chabazite.

Cannetaccio quarry

Samples, belonging to drill core, are characterized by an high average feldspar content (about 30wt%), calcite is between 11 and 21wt.%. As regards zeolites, chabazite content increase from the top toward the bottom of drill core, range between 2-32 wt.%, whereas phillipsite content decrease from the top toward the bottom, and it is between 2 and 27wt.%. Analcime has a content almost constant in the upper and central part of drill core, about 6 wt%, while slightly decrease towards the bottom up to disappear in the last three samples. All samples are characterized by wide range of smectite content between 4-19 wt%. Table 4.7 reports the quantitative mineralogical data of drill core samples.

4- RESULTS

Table 4.7: Mineralogical content of samples, belong to drill core (Cannetaccio quarry) as determined by XRD using RIR (reference intensity ratio) method.

Sample	Smectite [%]	Biotite [%]	Chabazite [%]	Phillpsite [%]	Analcime [%]	Feldspar [%]	Calcite [%]	Total [%]	Amorphous [%]
C1_1	5 (± 1)	0	3 (± 1)	23 (± 1)	6 (± 1)	32 (± 6)	15 (± 1)	86 (± 11)	14
C1_2	6 (± 1)	0	2 (± 1)	15 (± 1)	7 (± 1)	40 (± 8)	15 (± 1)	86 (± 13)	14
C1_3	4 (± 1)	0	3 (± 1)	27 (± 1)	6 (± 1)	36 (± 7)	13 (± 1)	89 (± 12)	11
C1_4	10 (± 1)	0	2 (± 1)	15 (± 1)	6 (± 1)	34 (± 7)	16 (± 1)	84 (± 12)	16
C1_5	9 (± 1)	0	2 (± 1)	16 (± 1)	6 (± 1)	36 (± 7)	15 (± 1)	85 (± 12)	15
C1_6	11 (± 2)	1 (± 1)	6 (± 1)	15 (± 1)	8 (± 1)	34 (± 7)	15 (± 1)	90 (± 14)	10
C1_7	10 (± 1)	0	4 (± 1)	11 (± 1)	8 (± 1)	31 (± 6)	13 (± 1)	77 (± 12)	23
C1_8	12 (± 2)	0	5 (± 1)	18 (± 1)	5 (± 1)	34 (± 7)	13 (± 1)	88 (± 13)	12
C1_9	11 (± 2)	0	4 (± 1)	16 (± 1)	5 (± 1)	32 (± 6)	12 (± 1)	79 (± 12)	21
C1_10	12 (± 2)	0	6 (± 1)	17 (± 1)	5 (± 1)	32 (± 6)	13 (± 1)	84 (± 10)	16
C1_11	12 (± 2)	0	9 (± 1)	15 (± 1)	5 (± 1)	31 (± 6)	13 (± 1)	85 (± 12)	15
C1_12	10 (± 1)	0	7 (± 1)	11 (± 1)	6 (± 1)	32 (± 6)	15 (± 1)	83 (± 11)	17
C1_13	10 (± 1)	0	7 (± 1)	8 (± 1)	6 (± 1)	34 (± 7)	13 (± 1)	79 (± 12)	21
C1_14	10 (± 1)	0	8 (± 1)	8 (± 1)	2 (± 1)	35 (± 7)	14 (± 1)	77 (± 12)	23
C1_15	13 (± 2)	0	7 (± 1)	6 (± 1)	5 (± 1)	34 (± 7)	12 (± 1)	77 (± 13)	23
C1_16	9 (± 1)	0	11 (± 1)	8 (± 1)	7 (± 1)	35 (± 7)	13 (± 1)	84 (± 12)	16
C1_17	15 (± 2)	0	9 (± 1)	7 (± 1)	6 (± 1)	35 (± 7)	17 (± 1)	89 (± 13)	11
C1_18	13 (± 2)	1 (± 1)	9 (± 1)	7 (± 1)	5 (± 1)	30 (± 6)	17 (± 1)	82 (± 13)	18
C1_19	15 (± 2)	1 (± 1)	11 (± 1)	10 (± 1)	6 (± 1)	31 (± 6)	17 (± 1)	90 (± 13)	10
C1_20	14 (± 2)	0	6 (± 1)	2 (± 1)	8 (± 1)	32 (± 6)	17 (± 1)	79 (± 12)	21
C1_21	14 (± 2)	1 (± 1)	10 (± 1)	5 (± 1)	10 (± 1)	32 (± 6)	17 (± 1)	89 (± 13)	11
C1_22	11 (± 2)	1 (± 1)	13 (± 1)	7 (± 1)	6 (± 1)	27 (± 5)	15 (± 1)	80 (± 12)	20
C1_23	12 (± 2)	1 (± 1)	13 (± 1)	6 (± 1)	7 (± 1)	28 (± 6)	21 (± 1)	88 (± 13)	12
C1_24	19 (± 3)	1 (± 1)	11 (± 1)	9 (± 1)	5 (± 1)	31 (± 6)	16 (± 1)	92 (± 14)	8
C1_25	18 (± 3)	1 (± 1)	10 (± 1)	7 (± 1)	4 (± 1)	34 (± 7)	14 (± 1)	87 (± 15)	13
C1_26	17 (± 2)	1 (± 1)	19 (± 1)	9 (± 1)	2 (± 1)	33 (± 7)	15 (± 1)	96 (± 14)	4
C1_27	14 (± 2)	1 (± 1)	26 (± 1)	10 (± 1)	1 (± 1)	30 (± 6)	15 (± 1)	97 (± 13)	3
C1_28	13 (± 2)	0	34 (± 2)	2 (± 1)	0	25 (± 5)	13 (± 1)	87 (± 11)	13
C1_29	12 (± 2)	0	32 (± 2)	3 (± 1)	0	24 (± 5)	11 (± 1)	82 (± 11)	18
C1_30	6 (± 1)	0	30 (± 2)	4 (± 1)	0	19 (± 4)	21 (± 1)	80 (± 9)	20

Error in brackets = $\sqrt{\sigma_1^2 + \sigma_2^2 + \dots}$ (Chipera and Bish, 1995), amorphous % by difference

The vertical variation of feldspar, calcite, chabazite, phillpsite and analcime contents along the drill core are reported in figure 4.6.

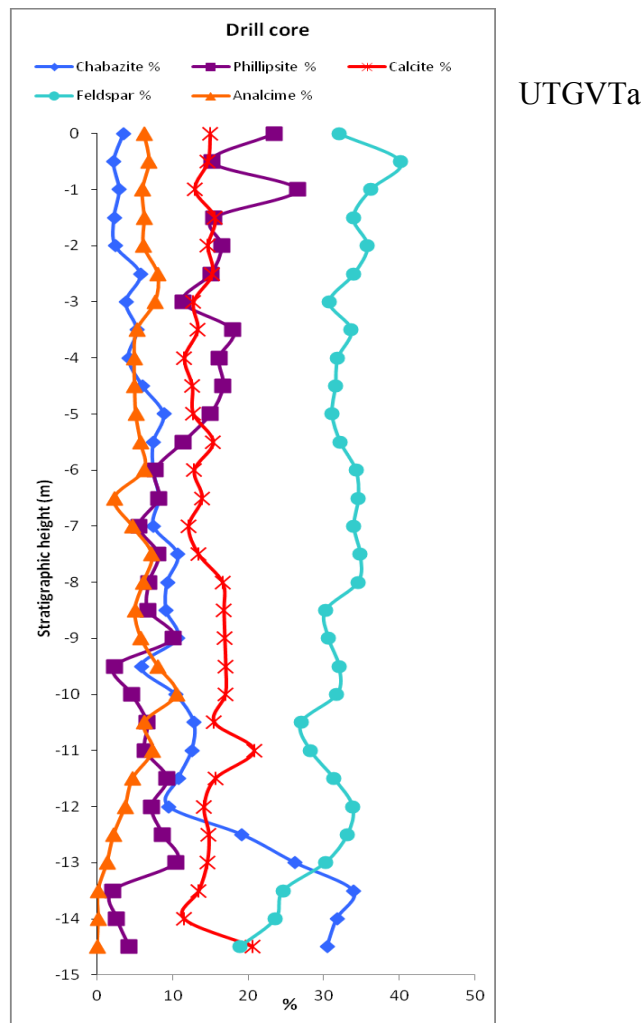


Figure 4.6: Vertical variation of feldspar, calcite and zeolitic minerals: chabazite, phillipsite and analcime. The whole drill core belongs to the middle part of UTGVTa unit.

The evolution of zeolitization process towards more stable phase (authigenic feldspar) is confirmed in samples of drill core. Figure 4.3, as seen in samples belong to vertical sampling, confirms the crystallization of feldspar at the expense of chabazite, favored by high temperature for a long time, a condition suitable for feldspatization process, that was likely reached in this quarry due to the highest thickness of the whole TGVT succession (about 70m). The decrease of feldspars suggests unsuitable temperatures for feldspatization. The decrease of analcime can be attributed to the lower content of leucite phenocrysts, inasmuch the UTGVTa unit flow is associated to the white-pumice eruption (inner part of magma chamber, Masotta et al., 2010).

In the last phases of the research, samples were collected from the quarry floor where the core had been drilled and along one of the quarry walls bordering the same floor.

Samples collected from the quarry walls have a wide range of feldspar content between 17 wt% and 40 wt%, calcite is about 14 wt% with the exception of a sample with 4

wt%. Chabazite is the main zeolite, it range between 10 and 36 wt%, followed by phillipsite with range between 4 and 13 %. Analcime is only found in samples Can 3 and Can 6, the content is 5 wt% and 1 wt% respectively (table 4.8). Smectite range between 7-17 wt%.

Table 4.8: Mineralogical content of samples as determined by XRD using RIR (reference intensity ratio) method (Cannetaccio quarry).

Sample	Smectite [%]	Chabazite [%]	Phillipsite [%]	Analcime [%]	Feldspar [%]	Calcite [%]	Total [%]	Amorphous
Can 1	7 (± 1)	15 (± 1)	4 (± 1)	0	28(± 9)	15 (± 1)	69 (± 13)	31
Can 2	9 (± 1)	22 (± 1)	11 (± 1)	0	30 (± 10)	12 (± 1)	85 (± 14)	15
Can 3	17 (± 2)	11 (± 1)	9 (± 1)	5 (± 1)	40 (± 8)	4 (± 1)	86 (± 14)	14
Can 4	17 (± 2)	20 (± 1)	6 (± 1)	0	33 (± 6)	14 (± 1)	91 (± 11)	9
Can 5	11 (± 1)	36 (± 2)	13 (± 1)	0	17 (± 3)	17 (± 1)	95 (± 8)	5
Can 6	9 (± 1)	10 (± 1)	8 (± 1)	1 (± 1)	27 (± 12)	12 (± 1)	66 (± 17)	34

Error in brackets = $\sqrt{\sigma_1^2 + \sigma_2^2 + \dots}$ (Chipera and Bish, 1995), amorphous % by difference

Samples collected from the quarry floor have a feldspar content greater than 24 wt%, with the exception of sample S2, where the feldspar content is 6 wt%. Calcite is between 9 and 17%. Seven samples (from P1 to P7) have phillipsite as main zeolite, the content is between 9-21 wt%, followed by chabazite (3-9 wt%). In these samples analcime is between 3-6 wt%, with the exception of P5 sample where it is absent. Sample P8 show the same content of chabazite and phillipsite (10%), and analcime content is 2 wt%. The last four samples (CC1, CC2, S1 and S2) contain chabazite with a wide range (15-47 wt%), phillipsite range between 5-15%, these samples are characterized by the absence of analcime. Samples collected from the quarry floor are characterized by an almost smectite content (<9 wt.%) (table 4.9).

Table 4.9: Mineralogical content of samples as determined by XRD using RIR (reference intensity ratio) method (Cannetaccio quarry)

Sample	Smectite [%]	Chabazite [%]	Phillipsite [%]	Analcime [%]	Feldspar [%]	Calcite [%]	Total [%]	Amorphous
P1	7 (± 1)	8 (± 1)	13 (± 1)	5 (± 1)	33 (± 6)	15 (± 1)	81 (± 11)	19
P2	9 (± 1)	7 (± 1)	14 (± 1)	5 (± 1)	30 (± 6)	14 (± 1)	79 (± 11)	21
P3	6 (± 1)	7 (± 1)	18 (± 1)	4 (± 1)	24 (± 5)	17 (± 1)	76 (± 10)	24
P4	8 (± 1)	6 (± 1)	13 (± 1)	6 (± 1)	33 (± 6)	9 (± 1)	76 (± 11)	24
P5	6 (± 1)	3 (± 1)	21 (± 1)	0	32 (± 6)	14 (± 1)	77 (± 10)	23
P6	7 (± 1)	9 (± 1)	11 (± 1)	2 (± 1)	32 (± 6)	15 (± 1)	75 (± 11)	24
P7	7 (± 1)	8 (± 1)	9 (± 1)	3 (± 1)	30 (± 6)	13 (± 1)	70 (± 11)	30
P8	7 (± 1)	10 (± 1)	10 (± 1)	2 (± 1)	32 (± 6)	17 (± 1)	80 (± 11)	20
CC1	7 (± 1)	15 (± 1)	11 (± 1)	0	26 (± 5)	13 (± 1)	72 (± 9)	28
CC2	6 (± 1)	20 (± 1)	9 (± 1)	0	24 (± 5)	13 (± 1)	72 (± 9)	28
S1	3 (± 1)	26 (± 1)	15 (± 1)	0	26 (± 5)	13 (± 1)	83 (± 9)	17
S2	3 (± 1)	47 (± 3)	5 (± 1)	0	6 (± 2)	16 (± 1)	76 (± 8)	24

Error in brackets = $\sqrt{\sigma_1^2 + \sigma_2^2 + \dots}$ (Chipera and Bish, 1995), amorphous % by difference

The presence of phillipsite as main zeolite, on the top of the drill core, and within the samples from the quarry floor, as observed to the middle part of vertical sampling, allow to identify the top of UTGVTa unit. The high feldspar content in the overall samples confirms the high temperature suitable for feldspatization wherever deposit reaches higher thickness.

Fantini quarry

Samples, belonging to the lower portion of UTGVTa unit, are collected along two site of this quarry. All samples have a low feldspar content that never exceed 11 wt%, calcite is almost constant between 11 and 16 wt%. Samples are characterized by a high total zeolite content, between 47 and 68wt.%, with chabazite prevailing, followed by phillipsite (2 and 13 wt%). The sample C5_1 has the highest chabazite content reaching 64 wt%. The whole samples are lacking of analcime. Table 4.10 summarized the quantitative mineralogical data.

The occurrence of chabazite, along with the constant feldspar content around 10 wt% (attributed to a primary phase, as shown in km 13-12.7 outcrop), suggest low temperature unsuitable for feldspatization, probably due to the contact of the flow with the cooler basement. The lowermost unit of UTGVTa is associated to white pumice eruption (absence of leucite phenocryst), and this can explain the absence of analcime. All samples are characterized by smectite content < 7 wt%.

Table 4.10: Mineralogical content of samples as determined by XRD using RIR (reference intensity ratio) method (Fantini quarry)

Sample	Smectite [%]	Chabazite [%]	Phillipsite [%]	Feldspar [%]	Calcite [%]	Total [%]	Amorphous [%]
C4_1	2 (± 1)	49 (± 3)	2 (± 1)	10 (± 1)	11 (± 1)	75 (± 7)	25
C4_2	2 (± 1)	41 (± 2)	13 (± 1)	10 (± 1)	16 (± 1)	83 (± 6)	17
C4_3	7 (± 1)	42 (± 2)	5 (± 1)	9 (± 2)	12 (± 1)	75 (± 7)	25
C5_1	7 (± 1)	64 (± 4)	4 (± 1)	9 (± 2)	12 (± 1)	95 (± 9)	5
C5_2	5 (± 1)	49 (± 3)	10 (± 1)	11 (± 2)	13 (± 1)	88 (± 9)	12

Error in brackets = $\sqrt{\sigma_1^2 + \sigma_2^2 + \dots}$ (Chipera and Bish, 1995), amorphous % by difference

4.3.2. X-RAY FLUORESCENCE (XRF)

On the basis of mineralogical composition of the three distinct flow units of UTGVT formation, in order to determine the possible occurrence of different chemical composition of bulk rocks, several samples have been selected from each quarries for X ray fluorescence analysis.

Table 4.11 reports the chemical analyses of bulk samples collected from km 13 and km 12.7, Perina, SICAT and Fantini quarries. The chemical composition of the samples B2 and C1 is in agreement with the mineralogy and, in particular, they have a LOI values about 10 wt% as a consequence of its analcime content, that also determine its high value of NaO (about 2 wt%). The absence of chabazite, calcite determine the low values of CaO and K₂O, whereas the high value of Fe₂O₃ is due to predominantly glassy fraction.

Chabazite-rich rocks (km 12.7, Perina, SICAT and Fantini samples) have high CaO and LOI values; these rocks show a significant decrease of NaO, linked to the absence of analcime, a significant increase of CaO and K₂O, compared with the chemistry of the km 13 samples.

Tables 4.12 and 4.13 show the chemical analyses of vertical sampling and drill core rocks, respectively. Samples of vertical sampling have similar composition with the km 12.7, Perina, SICAT and Fantini samples, in particular, they have a high value of CaO and LOI in agreement the mineralogical assemblages (zeolite-rich rocks).

The drill core samples show higher values of K₂O, compared with the whole samples, as a consequence of high feldspar content. The sample C1_30 is an exception; it shows a significant increase of CaO and LOI values, and a slight decrease of K₂O, this features is attributed to the high chabazite content.

Table 4.11: Chemical analysis of bulk rocks (km 13, km 12.7, Perina, SICAT and Fantini quarries)

Quarry	km 13		km 12.7			Perina		SICAT			Fantini
Sample	B2	C1	CTP 1	CTP 3	CTP 5	C2-P2-1	C2-P2-2	C3-1	C3-2	C3-3	C4-1
SiO ₂	54,62	54,67	42,65	42,56	42,60	47,73	47,53	46,89	45,86	49,43	45,35
TiO ₂	0,68	0,58	0,50	0,46	0,49	0,43	0,43	0,43	0,42	0,45	0,41
Al ₂ O ₃	18,29	19,20	11,99	12,03	12,30	12,71	12,42	12,42	12,25	12,78	12,00
Fe ₂ O ₃	5,83	4,80	4,00	3,77	4,04	3,42	3,26	3,28	3,23	3,45	3,25
MnO	0,21	0,14	0,11	0,11	0,11	0,12	0,12	0,11	0,13	0,10	0,12
MgO	2,68	1,86	2,35	2,18	2,23	1,21	1,53	1,69	1,12	1,18	1,49
CaO	2,27	2,72	12,70	13,18	13,47	10,41	9,29	9,65	10,98	9,53	11,46
Na ₂ O	2,08	2,82	0,61	0,54	0,56	0,44	0,47	0,41	0,57	0,32	0,90
K ₂ O	3,13	3,24	6,36	6,12	5,56	6,93	6,91	5,58	6,72	6,21	6,28
P ₂ O ₅	0,17	0,13	0,13	0,14	0,15	0,07	0,07	0,08	0,07	0,11	0,07
LOI	10,04	9,86	18,60	18,91	18,51	16,56	17,96	19,46	18,65	16,43	18,68
Tot	100	100	100	100	100	100	100	100	100	100	100
Rb	439,91	525,38	275,04	259,79	250,70	279,00	293,82	255,34	271,58	227,13	287,34
Sr	755,04	1071,67	1409,05	1380,33	1483,33	1173,37	1426,33	3002,48	1920,24	2057,29	1317,01
Y	43,07	43,18	30,01	28,18	30,38	28,73	30,73	27,15	28,37	30,66	29,64
Zr	382,40	487,81	313,14	283,82	313,91	384,70	408,51	384,51	377,20	394,12	402,31
Nb	14,09	10,50	<LLD	<LLD	<LLD	4,44	0,66	<LLD	<LLD	<LLD	2,04
Ba	1003,98	1104,98	1073,26	1082,75	1130,28	743,27	854,02	864,47	950,51	907,94	717,58
Cr	56,07	20,91	23,63	19,79	23,83	36,27	19,61	15,56	16,84	22,43	39,44
Ni	40,99	22,00	20,11	18,81	20,88	26,97	17,30	17,50	19,29	19,49	31,03
Sc	10,65	4,07	9,32	8,80	11,87	5,70	6,76	7,29	8,34	8,82	6,04
V	88,40	35,30	65,24	67,51	72,70	44,56	15,24	21,56	23,14	31,92	22,54
La	151,24	205,48	134,09	130,14	127,72	156,46	167,84	170,50	155,73	169,26	150,16
Ce	269,08	331,48	240,86	233,08	232,85	292,15	295,80	299,58	285,23	306,43	267,26

Dott. Gianmarco Rapisardo. Scuola di dottorato in Scienze della Natura e delle sue Risorse.

Indirizzo: Scienza e tecnologia dei Minerali e delle rocce di interesse industriale. XXV ciclo.

Post-emplacement minerogenetic processes in Upper Tufo Giallo della Via Tiberina (Latium): a mineralogical and volcanological approach

Table 4.12: Chemical analysis of bulk rocks (vertical sampling samples)

Quarry	Vertical Sampling (Perina)											
Sample	CV_1	CV_3	CV_7	CV_9	CV_15	CV_16	CV_17	CV_18	CV_23	CV_27	CV_31	CV_38
SiO ₂	43,34	43,72	44,73	42,95	43,69	44,40	45,39	45,32	46,49	46,33	47,84	47,10
TiO ₂	0,48	0,48	0,46	0,45	0,46	0,46	0,47	0,47	0,46	0,46	0,46	0,48
Al ₂ O ₃	12,82	12,30	12,68	12,22	12,53	12,93	13,61	13,21	13,65	13,72	13,66	13,45
Fe ₂ O ₃	4,06	3,78	4,25	3,43	3,43	3,38	3,49	3,36	3,42	3,48	3,49	3,50
MnO	0,12	0,12	0,17	0,11	0,11	0,12	0,12	0,11	0,13	0,12	0,12	0,09
MgO	1,87	1,89	1,53	1,69	1,84	1,40	1,44	1,71	1,45	1,40	1,49	1,73
CaO	13,52	13,85	11,92	14,16	11,99	11,26	11,07	10,32	9,65	9,75	9,83	10,56
Na ₂ O	0,33	0,32	0,45	0,51	0,68	0,86	0,80	0,77	0,46	0,44	0,35	0,31
K ₂ O	5,83	6,62	6,17	5,50	6,41	7,12	7,71	7,48	7,30	7,49	7,95	7,18
P ₂ O ₅	0,12	0,12	0,10	0,09	0,09	0,09	0,09	0,08	0,08	0,08	0,08	0,09
LOI	17,51	16,82	17,54	18,90	18,79	17,99	15,80	17,18	16,91	16,73	14,73	15,50
Tot	100	100	100	100	100	100	100	100	100	100	100	100
Rb	265,16	253,24	289,70	280,19	304,78	319,73	332,10	319,03	312,66	308,06	281,12	277,15
Sr	1689,74	1379,04	1849,40	1860,47	1614,73	1434,43	1439,71	1597,82	1530,26	1242,28	1066,30	1111,97
Y	28,17	28,56	29,00	29,58	32,64	33,54	36,20	34,03	35,22	34,95	34,32	34,25
Zr	302,70	299,01	345,72	335,21	387,77	410,13	434,79	417,72	448,79	444,36	413,51	380,92
Nb	<LLD	<LLD	<LLD	<LLD	<LLD	0,49	1,27	<LLD	1,25	7,11	9,33	6,36
Ba	1095,03	988,24	953,46	950,77	962,66	1035,34	1117,25	1035,89	870,71	764,55	679,06	519,53
Cr	23,53	27,73	15,16	13,12	3,59	0,33	0,76	4,24	4,59	13,71	23,53	32,30
Ni	26,68	23,30	19,72	16,38	12,16	9,23	14,04	10,40	11,85	18,56	17,89	21,28
Sc	7,21	5,85	5,55	7,33	7,26	5,60	4,31	3,74	5,68	3,09	4,54	6,36
V	65,13	69,99	47,81	39,20	38,84	25,55	36,80	13,81	21,20	49,00	39,79	43,66
La	127,61	121,02	143,44	136,51	164,51	166,95	183,30	171,75	187,38	184,72	158,75	156,93
Ce	238,56	223,92	282,49	270,41	309,43	330,03	325,67	328,93	341,46	314,42	286,26	271,97

Table 4.13: Chemical analysis of bulk rocks (drill core samples)

Quarry	Drill core (Cannetaccio)										
Sample	C1-1	C1-3	C1-8	C1-12	C1-15	C1-20	C1-22	C1-24	C1-26	C1-28	C1-30
SiO ₂	49,15	48,80	48,54	47,49	49,40	49,41	48,40	49,04	48,17	48,09	42,86
TiO ₂	0,48	0,46	0,49	0,48	0,48	0,49	0,49	0,49	0,49	0,47	0,42
Al ₂ O ₃	13,05	13,83	14,10	13,53	13,65	13,60	13,76	13,73	13,93	13,84	12,07
Fe ₂ O ₃	3,60	3,50	3,84	3,49	4,07	4,22	3,67	3,76	3,54	3,82	2,75
MnO	0,11	0,12	0,26	0,10	0,11	0,12	0,10	0,10	0,10	0,12	0,12
MgO	1,57	1,41	1,65	1,57	1,73	1,79	1,84	1,81	1,82	1,78	1,31
CaO	10,30	9,70	9,62	11,13	9,26	9,45	10,51	9,83	10,04	9,52	15,10
Na ₂ O	0,91	0,82	0,74	0,75	0,68	0,71	0,75	0,61	0,43	0,33	0,29
K ₂ O	8,34	8,60	8,31	8,02	8,05	8,21	7,72	8,30	7,92	7,15	6,09
P ₂ O ₅	0,09	0,09	0,09	0,10	0,10	0,10	0,10	0,10	0,10	0,09	0,08
LOI	12,41	12,66	12,38	13,34	12,47	11,91	12,67	12,24	13,46	14,78	18,90
Tot	100	100	100	100	100	100	100	100	100	100	100
Rb	353,00	325,81	343,02	333,88	354,18	367,23	368,74	325,58	274,78	259,37	219,46
Sr	1619,65	1542,92	1511,02	1401,84	1154,97	1062,97	1048,64	994,78	1008,91	1288,82	1411,09
Y	36,07	36,76	37,66	38,29	37,34	37,92	36,54	36,98	36,81	34,65	29,39
Zr	465,71	442,49	454,78	444,66	432,38	424,50	413,78	419,52	422,46	433,71	359,30
Nb	0,09	0,96	2,11	3,74	9,49	11,75	10,43	11,53	11,63	6,67	<LLD
Ba	831,47	827,96	806,68	726,24	792,62	618,58	619,62	612,24	630,56	755,79	530,25
Cr	10,82	14,65	19,01	17,75	23,20	26,43	29,27	32,05	33,51	28,14	25,15
Ni	23,32	14,74	21,21	22,02	19,07	17,68	21,56	19,55	20,23	22,07	21,33
Sc	5,37	6,84	7,04	4,09	7,38	8,57	4,73	8,45	6,77	8,38	8,30
V	26,13	33,69	42,50	62,13	32,25	33,50	65,81	59,96	60,43	48,50	54,62
La	194,36	185,19	164,91	187,78	168,26	165,36	159,83	157,15	158,01	176,65	148,80
Ce	331,97	333,27	321,46	331,36	312,18	299,61	286,37	296,79	295,88	303,69	276,68

Insight into the geochemical variations, produced by diagenetic processes, can be obtained by comparing the composition of the glass (as a reference) with that of the diagenetic facies, in terms of SiO_2 , alkali, and alkaline-earth elements (Gündoğdu et al., 1996; Ibrahim and Hall 1996).

Figure 4.7, shows the difference between feldspar, chabazite and phillipsite-rich rocks. The high content of feldspar or zeolite do not influence the $\text{SiO}_2/\text{Al}_2\text{O}_3+\text{Fe}_2\text{O}_3$ ratio, whereas rocks that have high contents of these mineral phases are distinguished based on the following ratios: $((\text{Na}_2\text{O}+\text{K}_2\text{O})/(\text{Al}_2\text{O}_3+\text{Fe}_2\text{O}_3))$ vs. $(\text{CaO}+\text{MgO})/(\text{Al}_2\text{O}_3+\text{Fe}_2\text{O}_3)$.

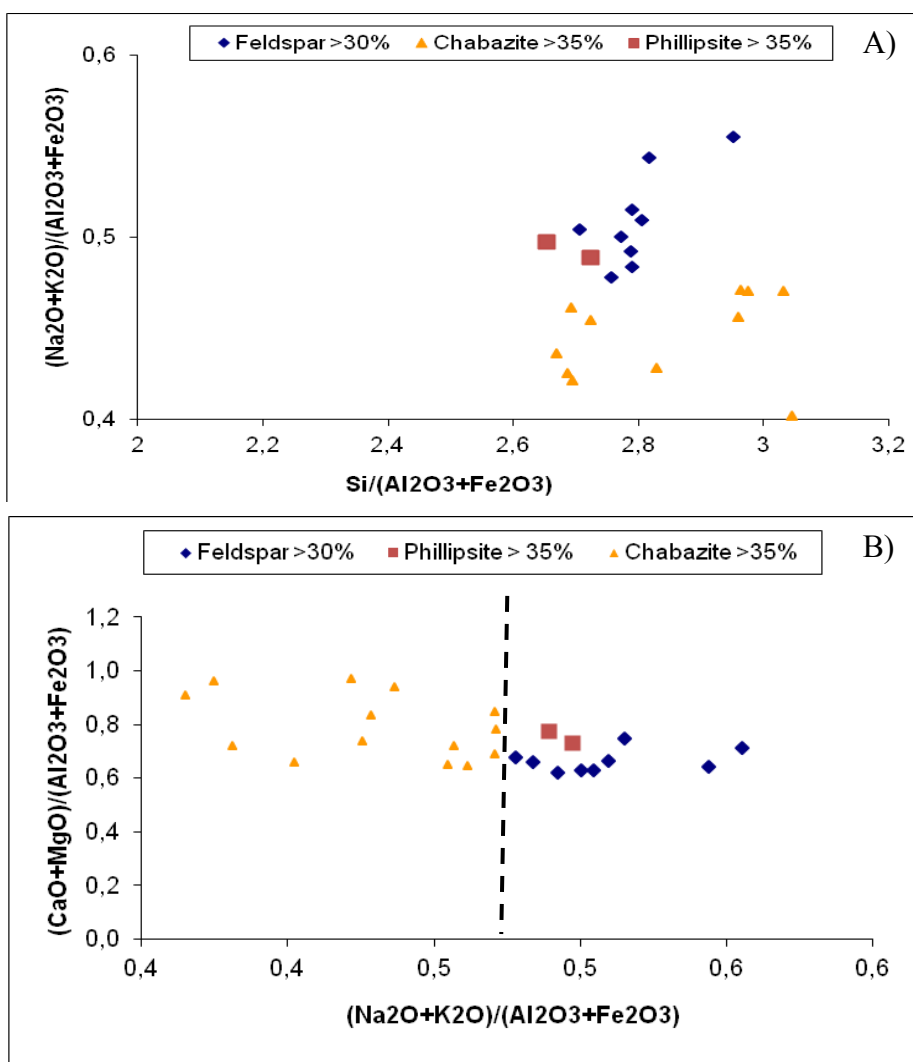


Figure 4.7: A) diagram $\text{Si}/(\text{Al}+\text{Fe}_2\text{O}_3)$ vs $(\text{Na}_2\text{O}+\text{K}_2\text{O})/(\text{Al}_2\text{O}_3+\text{Fe}_2\text{O}_3)$; B) diagram $(\text{Na}_2\text{O}+\text{K}_2\text{O})/(\text{Al}_2\text{O}_3+\text{Fe}_2\text{O}_3)$ vs. $(\text{CaO}+\text{MgO})/(\text{Al}_2\text{O}_3+\text{Fe}_2\text{O}_3)$

Figure 4.7 b) also discriminates representative data for chabazite-rich samples from phillipsite and feldspar-rich samples, whereas there is no clear difference between phillipsite-rich rocks and feldspar-rich samples, because of the similar K_2O values.

In order to obtain information on chemical composition of the system after the glass-to-zeolite transformation; The variation of some major elements (Si, Mg, Ca, Na, K) in zeolitized rocks were reported, according to Broxton et al. (1987).

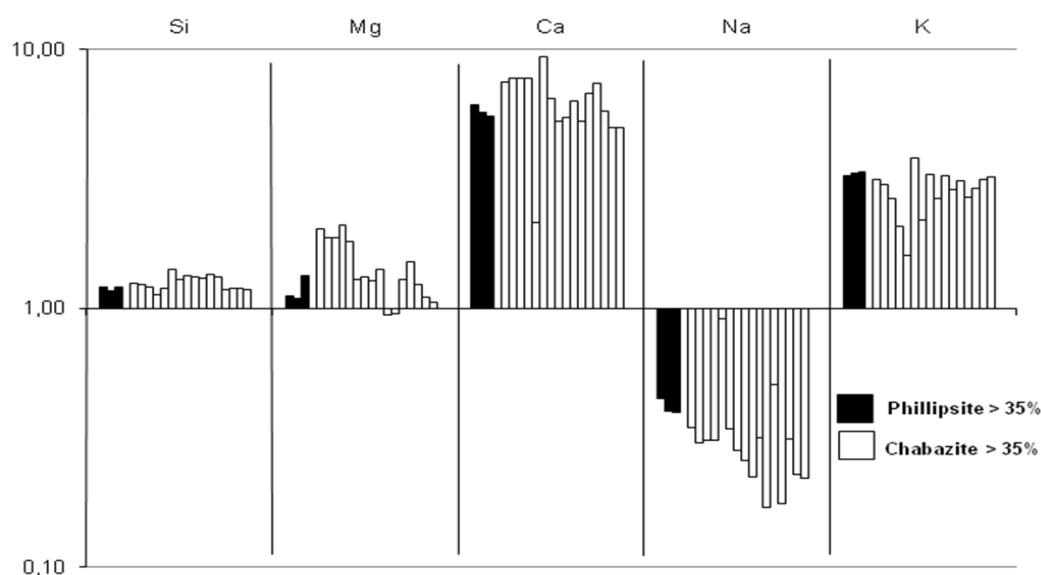


Figure 4.8. Broxton et al. (1987) diagram.

Figure 4.8 confirms the hypothesis of a calcic-potassic environment, that favored the chabazite crystallization, during the conversion process glass-to-zeolite, as shown by the increase in Ca and K content, and the Na depletion due to the glass hydrolysis.

4.3.3. CALCIMETRY

The quantitative mineralogical data relative to the calcite content, that also determine the high CaO percentage of chemical analysis of bulk rocks, were verified by calcimetry. Calcimetry allowed to determine the total carbonate content by attacking the sample with hydrochloric acid and measuring the CO_2 . To this purpose samples with the higher calcite wt%, obtained with RIR method, were selected. The results obtained through calcimetry confirm quantitative mineralogical data, and table 4.14 shows very similar values of calcite content.

Table 4.14: Comparison of calcite content (RIR and calcimetry values)

Analyses	RIR	Calcimetry
Sample	Calcite [%]	Calcite [%]
C1_1	15 (\pm 1)	17
C1_12	15 (\pm 1)	18
C1_22	15 (\pm 1)	15
C1_30	21 (\pm 1)	22
C3_2	14 (\pm 1)	12
C4_1	11 (\pm 1)	13
C2_P1_2	14 (\pm 1)	14
C2_P2_1	16 (\pm 1)	13

4.3.4. POLARIZING OPTICAL MICROSCOPE (OM)

Further mineralogical informations were obtained by polarizing optical microscopy (OM). OM observations show a clear distinction between primary and authigenic minerals.

Primary minerals are predominantly K-feldspar and subordinate pyroxenes and biotite. Figure 4.9 shows a sanidine crystal, with a carlsbad germination at crossed nicols.



Figure 4.9: Polarizing microscope photograph of sanidine crystal; left, parallel nicols, right, crossed nicols (magnification 4x)

Polarizing microscope observations confirm the presence of zeolitic minerals. Phillipsite clusters and chabazite crystals were observed. OM observations also showed presence of carbonatic clasts, belonging to the underlying sedimentary basement (figure 4.10).

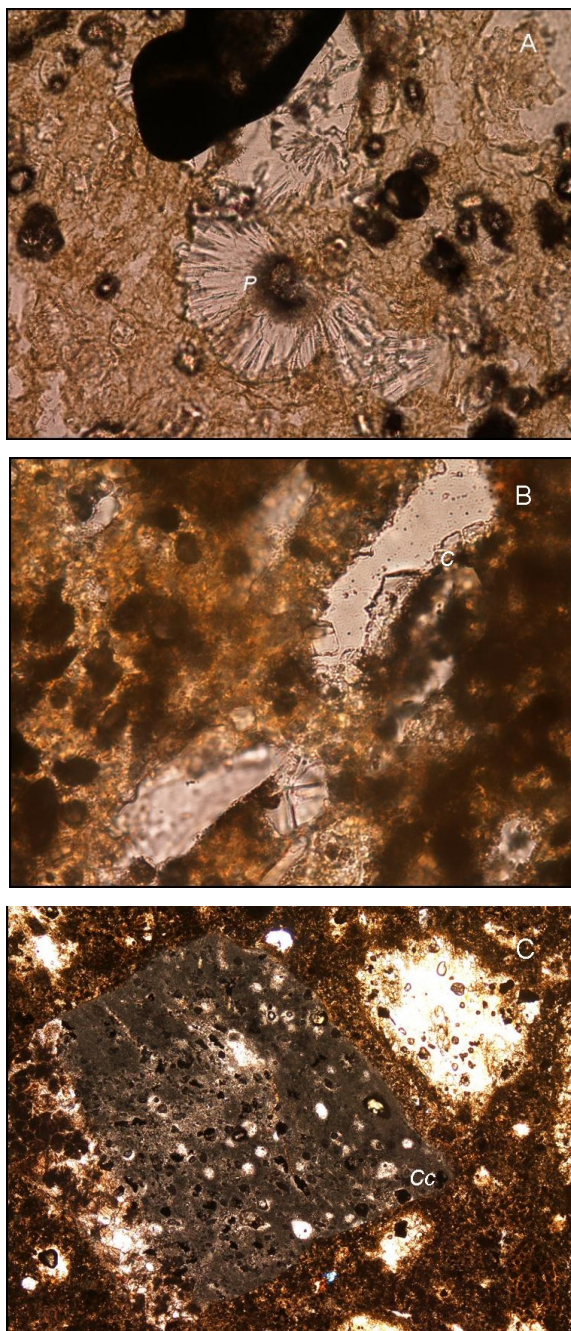


Figure 4.10: Polarizing microscope photograph of A) phillipsite (P); B) chabazite (C); C) Carbonatic clast (Cc)
(magnification 4x)

OM investigation allowed to identify presence of second generation of calcite that filled the fractures of the rock (figure 4.11).

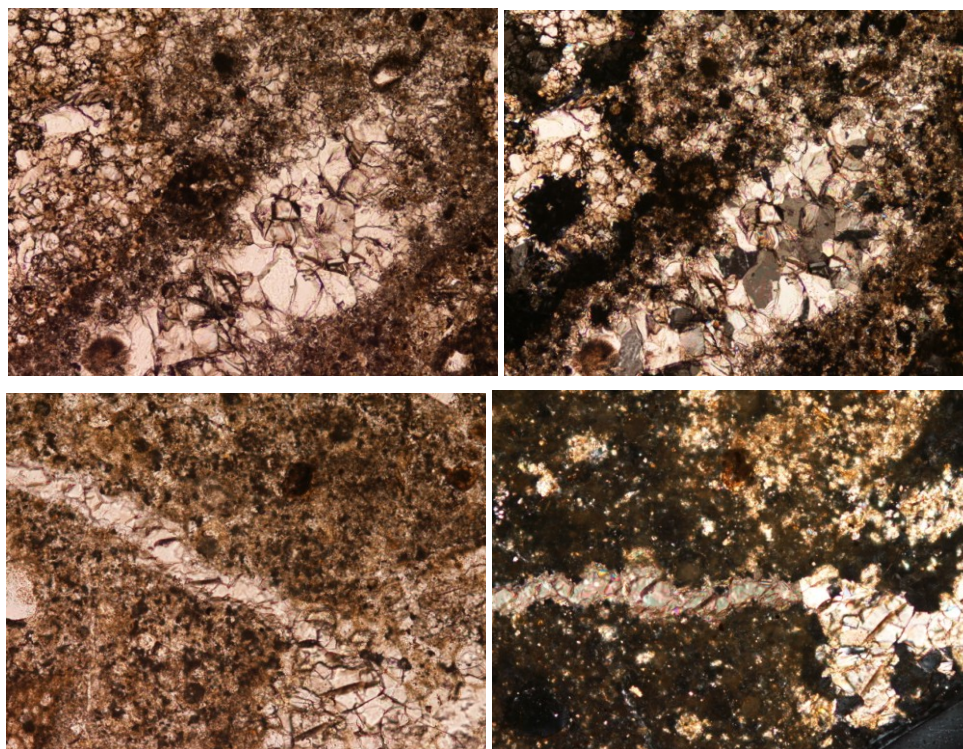


Figure 4.11 : Veins filled with calcite (magnification 20 x); left parallel nicols, right crossed nicols.

The occurrence of secondary calcite could suggest an initial acidic solution that dissolves the carbonatic clasts; this determines a buffer effect on the pH of solution, with hydrolysis and dissolution of the glassy fraction. The progressive increase of pH (basic environment) led to react the CaO with the CO₂ in solution, with the consequence precipitation of secondary calcite.

4.3.5. SCANNING ELECTRON MICROSCOPE (SEM)

SEM observations, carried out on a large number of samples, provided further information on authigenic minerals. On the basis of quantitative mineralogical data and OM observations several samples were selected in order to carry out SEM observations. Samples showed the presence of clusters of phillipsite, and rhombohedral chabazite crystals, in agreement both with the mineralogy OM observations. The presence of an authigenic feldspar (adularia-like) during the SEM observations was also observed, confirming the hypothesis of a feldspatization process, wherever deposit reaches the higher thickness. SEM observation also confirmed the initial acidic environment; as testified by the occurrence of glassy shards totally devitrified and replaced by clay minerals (smectite). Observations allowed to point out also analcime crystals. Figure 4.12 provides a general view of the mineralogical phases observed.

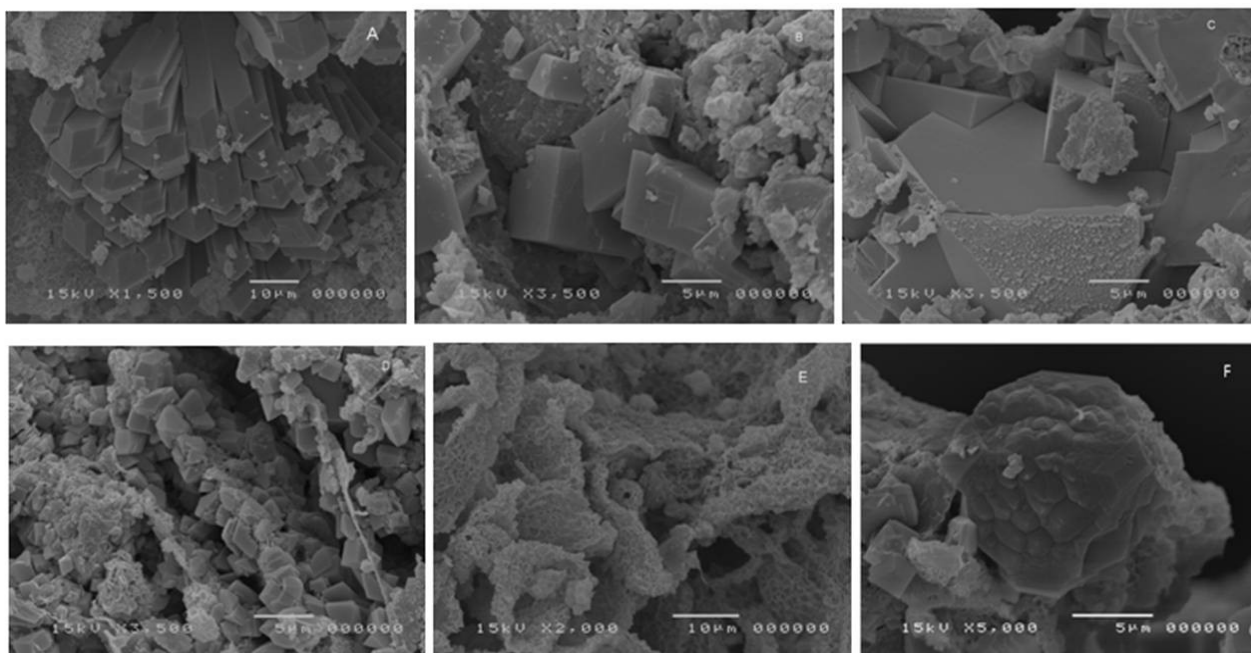


Figure 4.12: SEM micrograph :A) clusters of phillipsite; B) and C) rhombohedral chabazite crystals; D) adularia, E) smectite, F) analcime

SEM observations revealed that there were domains characterized by clusters of phillipsite, this zeolite is only concentrated in pumice, where it coats the walls and fills the cavities (figure 4.13). Only in pumice the chemical condition (sodic-potassic environment), allowing the crystallization of this zeolite has been maintained. Therefore the random higher phillipsite content can be attributed to an high pumice concentration.

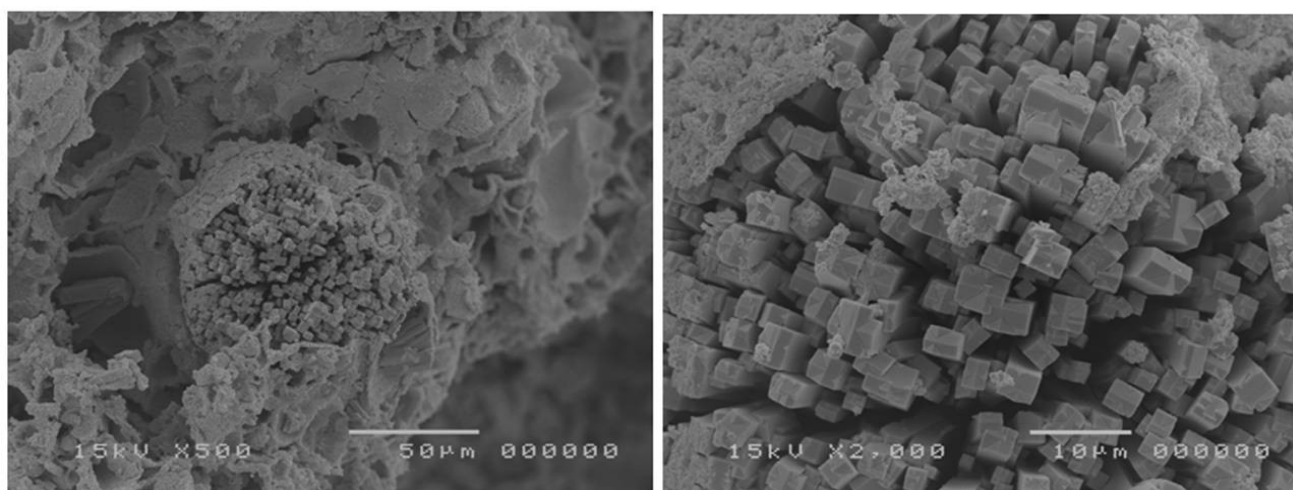


Figure 4.13: SEM micrograph, pumice vugs filled with clusters of phillipsite, on the right higher magnification of previous photograph.

Phillipsite crystals are characterized by prismatic morphology and typical cruciform twinning (figures 4.14).

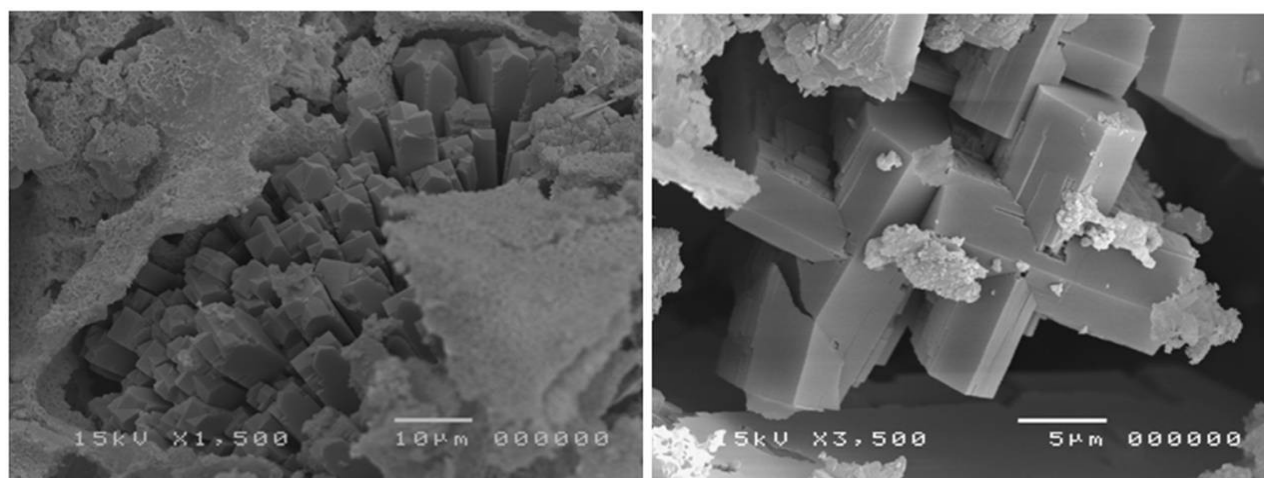


Figure 4.14: SEM micrographs: On the left cluster of phillipsite in pumice cavities, on the right phillipsite crystals with typical cruciform twinning

Chabazite-rich samples the presence of this zeolite was concentrated in the vugs of the rock, with crystals larger up to several tens of μm (figure 4.15). Chabazite crystals are associated with altered glassy shard; this feature could suggest an early crystallization sequence glass-to-smectite-to-chabazite. This sequence confirm an increase of initial acidic pH toward a basic environment, due to hydrolysis of glassy fraction.

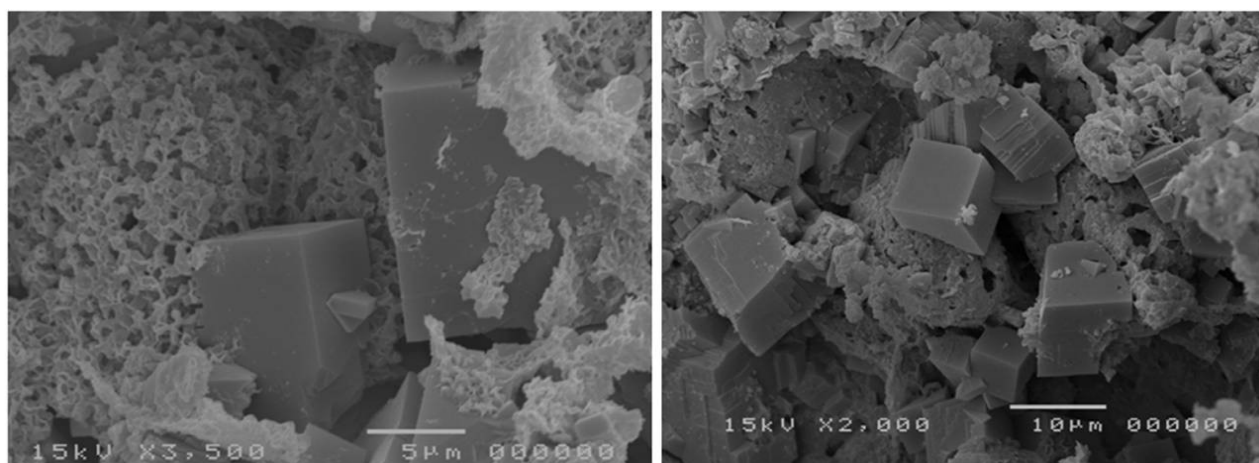


Figure 4.15: SEM micrographs of rhombohedral chabazite crystals in vitreous altered matrix.

Contrary to what observed for other Italian volcanic deposits (Neapolitan Yellow Tuff and Campanian Ignimbrite) unresolved association of chabazite and phillipsite are recognized.

Afterwards attention was focused on samples that had an high feldspar content. Authigenic feldspar is observed in association both with phillipsite and chabazite crystals (figure 4.16) and

also on wall of altered glassy shards (figure 4.17). These associations suggest a transformation from a metastable phase (zeolites) to more stable phase; but also the occurrence of high temperatures that allow the crystallization of authigenic feldspar from glass.

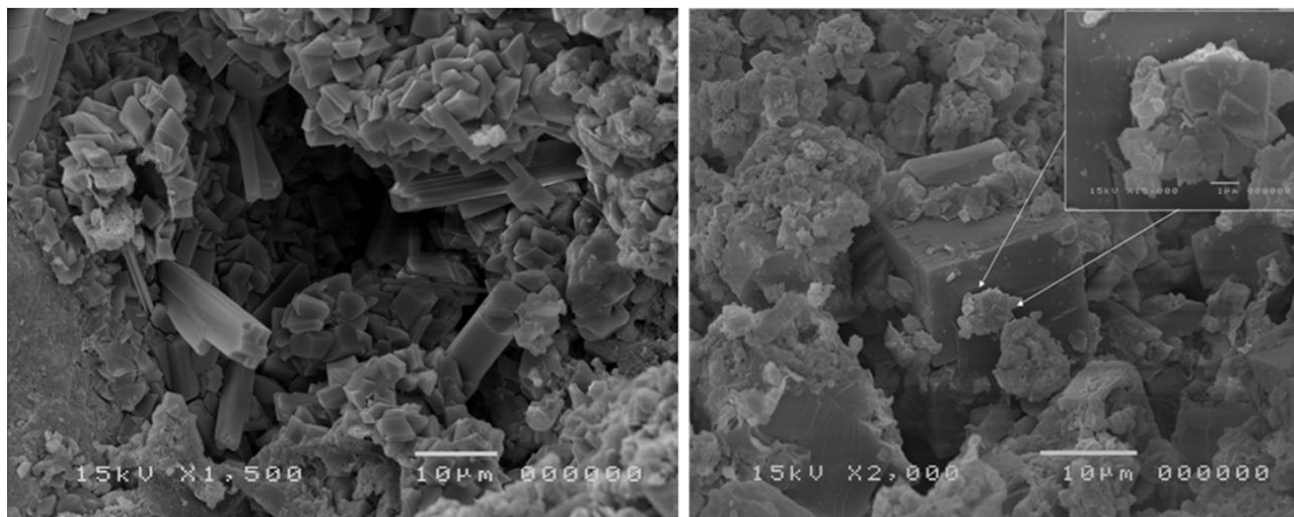


Figure 4.16: SEM micrographs, on the left authigenic feldspar (adularia) associated with phillipsite crystals; on the right authigenic feldspar (adularia) associated with rhombohedral chabazite.

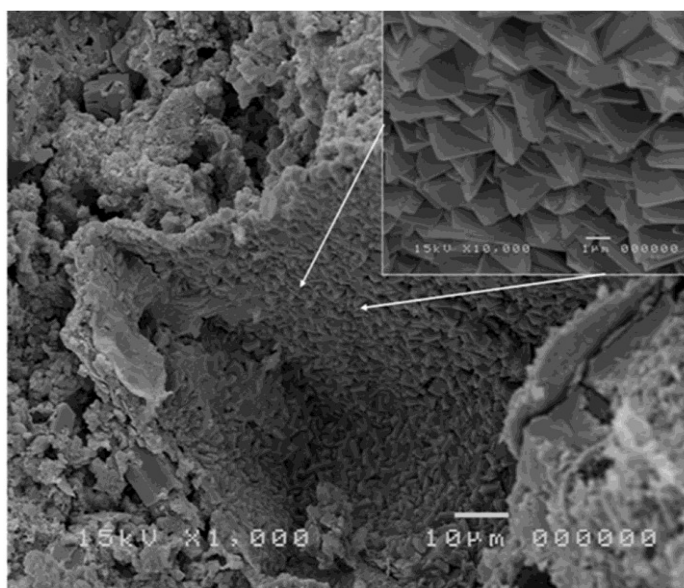


Figure 4.17: SEM micrograph of authigenic feldspar (adularia) on wall of altered glassy shards

SEM observations were carried out not only on lithified samples, but also on un-lithified samples, belonging to the discontinuities between the three sub-units. The latter samples allowed to observe analcime crystals, that were un-resolvable at low magnifications. Figure 4.18 testifies previous hypothesis, where the high analcime content can be attributed to the high percentage of black-grey scoria.

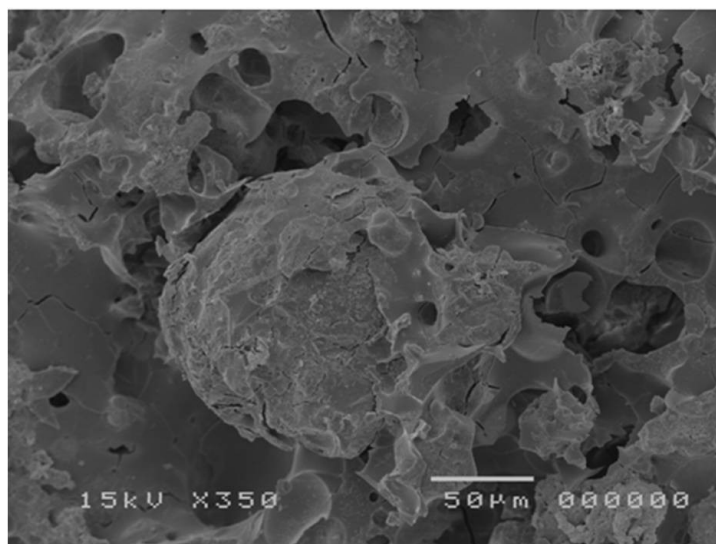


Figure 4.18: Analcime crystal belong to juvenile clast (black-grey scoria).

Observations both on polished thin sections and on analcime crystals, embedded in thermosetting bi-component resin, allowed better knowledge on the genesis of this zeolite. This investigation allow to verify that analcime derived from the alteration of primary leucite (Giampaolo and Lombardi, 1994; Giampaolo et al., 1997). Figure 4.19, showing a back-scattering electron (BSE) image of leucite crystal, where the crystal core is K-rich, whereas the rim show a Na-rich; the exchange between potassium and sodium indicated the initial analcimization process of the leucite crystal (Giampaolo et al., 1997). In order to verify to composition of core and rim of this crystal, the X-ray spectrum of two representative points are reported, the former show the presence of Si, Al and K, that are the typical component of leucite, the latter is characterized by Si, Al and Na, that are typical component of analcime.

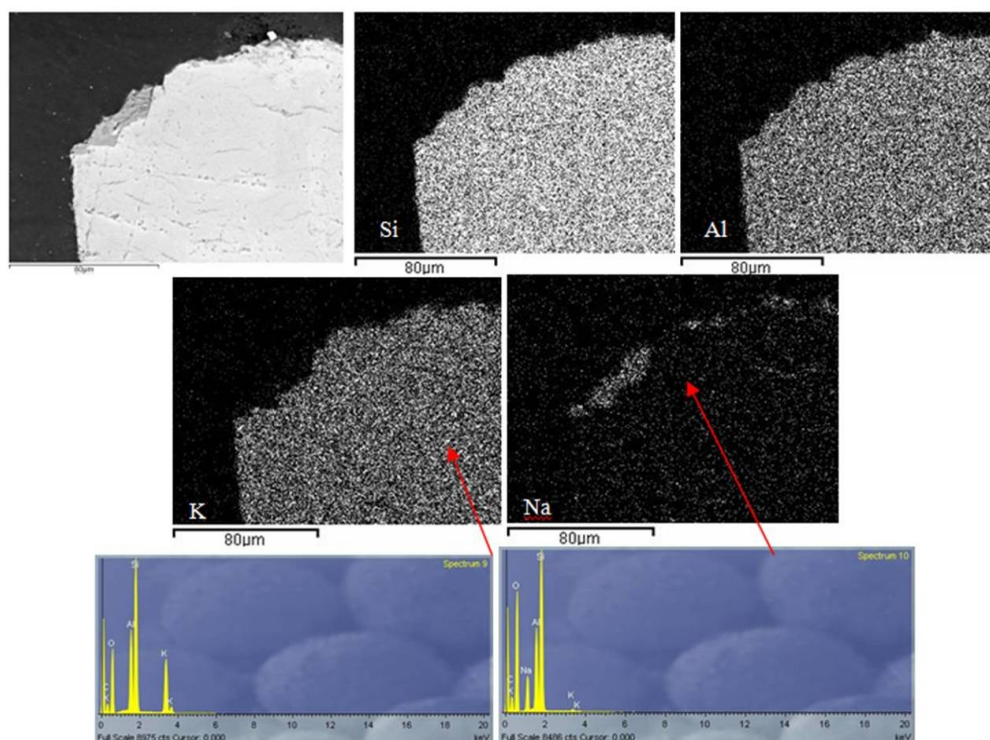


Figure 4.19: back-scattering electron image of leucite-analcimized

Quantitative mineralogical data, for most of the investigated samples, indicated a calcite content ≥ 10 wt%; further OM observations allowed to attribute the calcite content to: 1) carbonatic clasts and 2) calcitic cement. In order to verify the differences between the aforementioned two types of calcite back-scattering electron (hereafter BSE) investigations were carried out, that allow to obtain the elements distribution inside of the part of the thin section investigated; the distribution of elements as Si, Al, K, and Ca is also reported.

Figure 4.20, shows a thin section portion where is visible the presence of carbonatic clasts, and they are indicated by light color zones, concentrated to a restricted area.

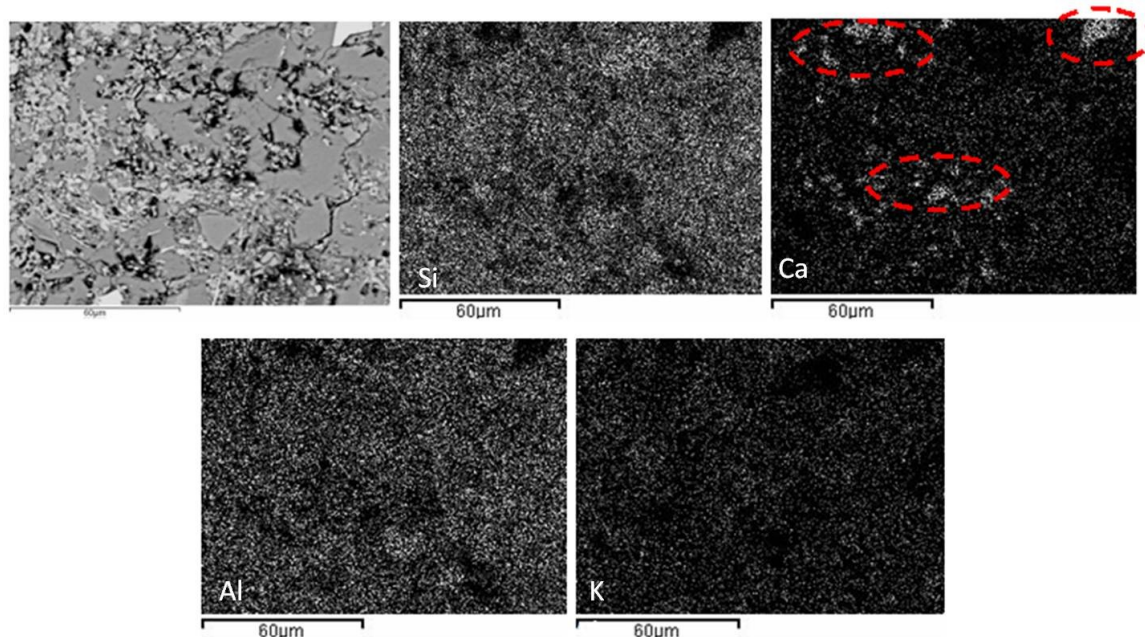


Figure 4.20: BSE images: Si, Ca, Al, K maps of element distribution, dashed areas pick out the carbonatic clasts.

Whereas, figure 4.21 shows a wide spread of calcium inside this part of the investigated thin section.

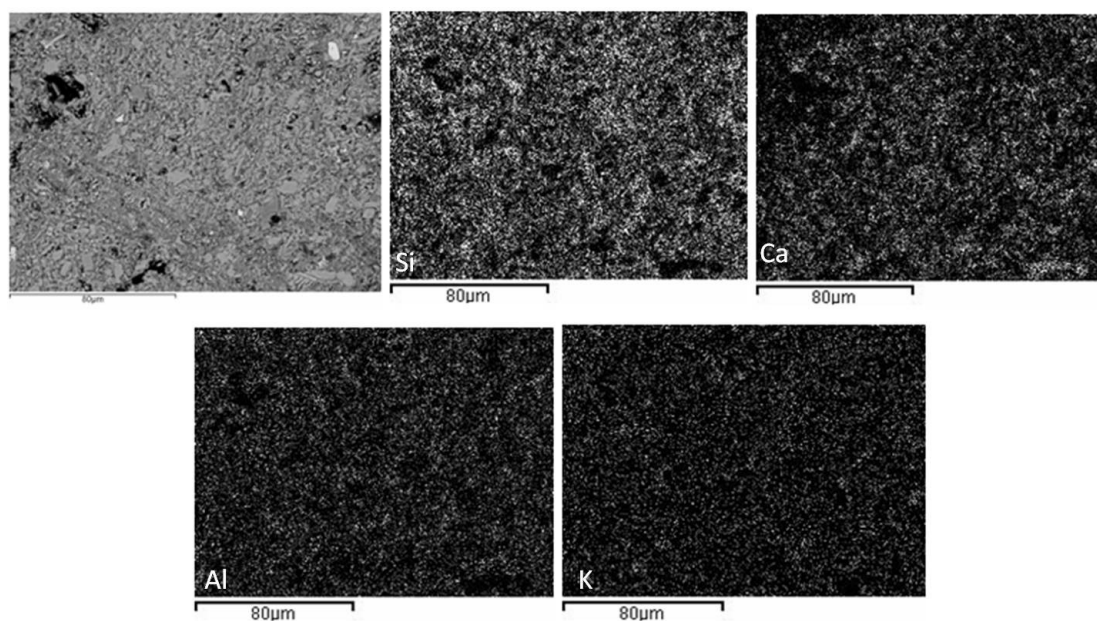


Figure 4.21: BSE images: Si, Ca, Al, K maps of element distribution

Therefore a comparison between the Ca element map of TGVT formation with others central-southern Italian volcanoclastic formations Campanian Ignimbrite (CI) and Neapolitan Yellow Tuff (NYT) were carried out (figure 4.22).

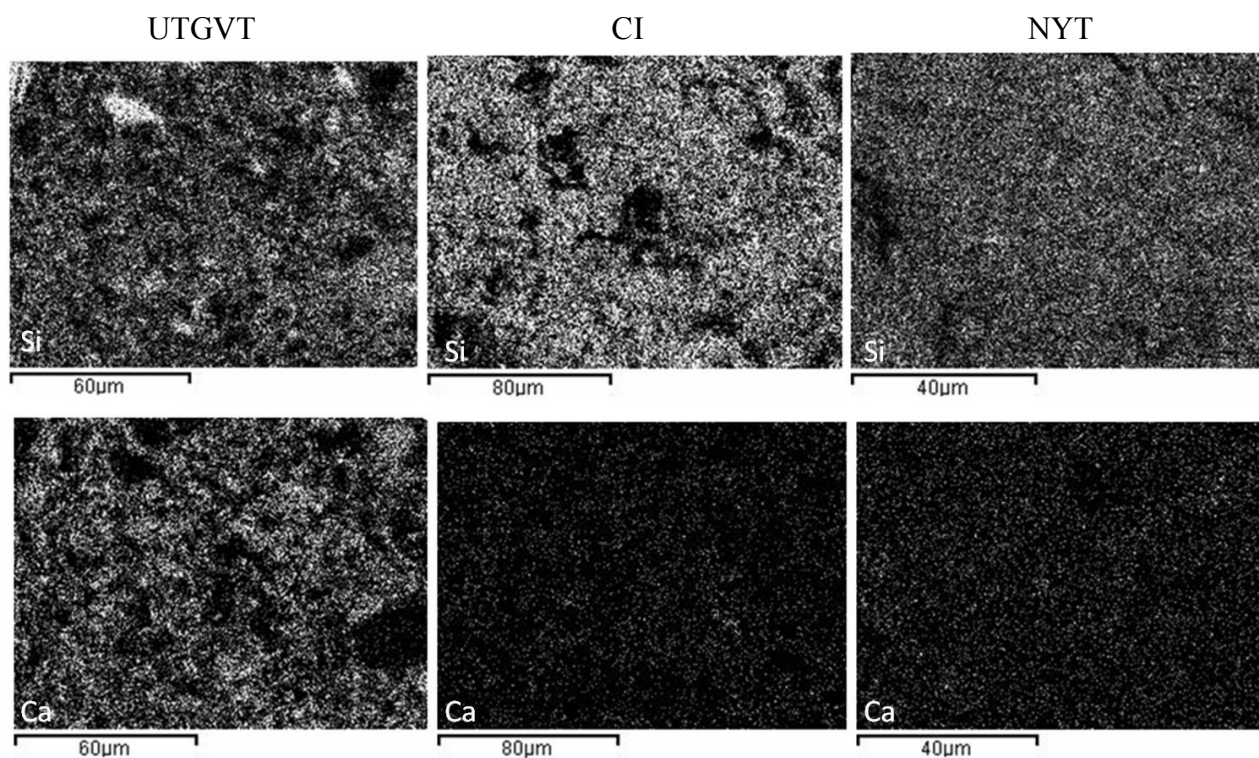


Figure 4.22: Comparison of Si and Ca distribution maps in UTGVT-CI-NYT.

Figure 4.22 shows a more intense light color in UTGVT, rather than CI and NYT, due to the presence both of high calcium content of zeolites and to calcitic cement in the Sabatini pyroclastic formation, whereas the Ca distribution maps of CI and NYT are only attributed to the contribution of extra-framework cation of zeolites. Previous figures clearly show the presence of secondary calcite, confirming the hypothesis obtained from early OM observation. Further researches were carried out on samples that show a wide spread of Ca, by reacting with acid acetic, in a solution of 30 wt%. Afterwards the sample which has reacted with the acid is compared with the surface of the same sample not treated. BSE image shows the lower spread of Ca as result of treatment, the calcium distribution map is attributed to the contribution of Ca content of zeolites (figure 4.23).

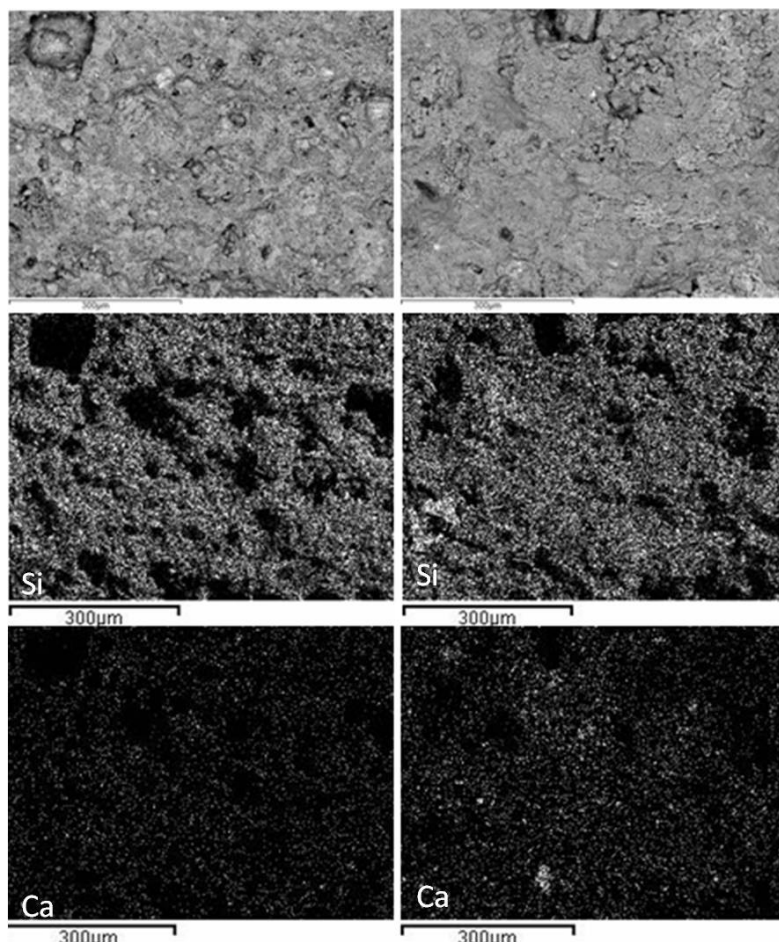


Figure 4.23: Comparison between raw and acid acetic treated sample., left is reported the elements maps of Si and Ca in acid acetic treated sample. Right is showed the elements maps of Si and Ca in the un-treated sample.

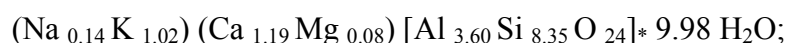
4.3.6. EDS MICROANALYSIS

In order to obtain better knowledge on glassy fraction and solution composition, which led to the minerogenesis of zeolites, chemical analysis of chabazite, phillipsite, analcime and glass (tables 4.15, 4.16, 4.17 and 4.18 respectively) of the investigated samples were carried out by EDS microanalysis. For each sample, the average data produced during the investigation were reported. The aforementioned tables also show the number of atoms, normalized to 24, 32, 96 oxygens for the chabazite, phillipsite and analcime respectively; while for glass, atomics content are calculated according to Barth's standard anhydrous cell (160 oxygen atoms). For zeolites, H₂O content is calculated by difference, in tables also are reported balance error (E%), the Si/(Si+Al) ratio (R), Si/Al ratio, Na/K ratio, divalent/monovalent ratio (D/M).

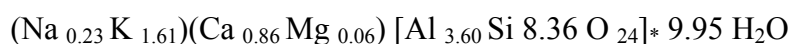
Chemical data of chabazite (table 4.15) showed a variable calcium and potassium content. Samples, belonging to vertical sampling and drill core, have an high Ca content followed by

potassium. Mineralogical data show that these samples are also characterized by an higher feldspar content. While chabazites, belonging to SICAT and Fantini quarries (lowermost portion of flow units), have a high K content followed by Ca. Quantitative mineralogical data showed that these samples have the lower feldspar content. The occurrence of Ca-rich chabazite and high feldspar content, could suggest a K depletion in the system as a consequence of authigenic feldspar crystallization at the expense of zeolite. The high temperature needed for feldspatization, could determines an exchange process for the residual chabazite with the Ca-rich solution; thereby leading to Ca-rich chabazite. While the absence of authigenic feldspar in the lowermost portion of flow unit suggest low temperature, which does not allow exchange process with the Ca-rich solution. This could determine the occurrence of K-rich chabazite.

On the bases of these results two average chemical formulas were calculated: one for the calcic-potassic type:

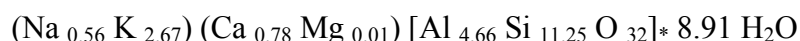


the second for the potassic-calcic character of chabazites:



The whole sampled showed a constant water content, about 18 wt%, and R value about 0.70; while they showed a very wide range of Si/Al and D/M ratios.

Chemical compositions of phillipsite (table 4.16) is quite constant in both flow units, and it illustrates its potassic-calcic character, with the following average chemical formula:



Also phillipsite showed a constant water content, about 15-16 wt%, and R value about 0.70, and a wide range of Si/Al and D/M ratios.

Chemical analyses of analcime (table 4.17) showed higher K and Ca content than those reported in literature for an authigenic analcime (Giampaolo et al., 1997). The high K content can be attributed to the starting leucite.



Analcime shows a R values about 0.69.

The R values are included in the range of 0.62-0.75, that allowed the classification of chabazite, phillipsite and analcime as intermediate zeolites.

Chemical analyses of glasses are obtained on juvenile clasts, belonging to un-lithified samples, embedded in thermosetting bi-component resin. Data (table 4.18) illustrates the chemical difference between the two type of glasses; the white pumice (WP) shows an high potassium content followed by calcium and sodium, whereas the black-grey scoria (BGS) had an higher calcium content, followed by potassium and sodium. These glasses are also different in terms of Si/Al ratio, in particular WP has a Si/Al ratio < 2.39 , while the BGS has an higher Si/Al ratio (> 2.42).

Table 4.15 :Chemical analyses (wt%) and unit-cell content of chabazite (calculated on 24 oxygens)

Quarry	Perina									
Unit	UTGVTb				UTGVTa					
Sample	CV 1	CV 3	CV 5	CV 9	CV 24	CV 32	CV 37	C2_P1_1		C2_P2_1
Mean	n°2	n°3	n°3	n°3	n°4	n°2	n°3	n°3	n°5	n°3
SiO ₂	50,66	50,32	50,04	50,46	50,62	50,91	50,63	50,10	50,44	50,36
Al ₂ O ₃	18,57	18,69	18,53	18,42	19,30	18,34	18,38	18,75	18,41	18,01
TiO ₂	0,03	0,00	0,04	0,01	0,08	0,04	0,09	0,23	0,10	0,09
Fe ₂ O ₃	0,22	0,11	0,17	0,10	0,10	0,04	0,21	0,02	0,07	0,03
MgO	0,34	0,37	0,30	0,32	0,13	0,42	0,21	0,33	0,22	0,39
CaO	7,40	6,74	6,87	6,63	6,09	6,48	5,80	5,02	4,94	6,05
MnO	0,13	0,00	0,13	0,18	0,04	0,16	0,12	0,00	0,08	0,13
Na ₂ O	0,29	0,49	0,44	0,53	0,51	0,53	0,63	0,71	0,81	0,43
K ₂ O	4,16	4,43	5,32	4,55	6,89	4,88	7,12	6,76	7,69	5,95
H ₂ O	18,20	18,86	18,14	18,80	16,25	18,22	16,82	18,09	17,24	18,57
tot	81,80	81,14	81,86	81,20	83,75	81,78	83,18	81,91	82,76	81,43
Si	8,33	8,34	8,29	8,37	8,25	8,39	8,33	8,32	8,35	8,39
Al	3,60	3,65	3,62	3,60	3,71	3,56	3,56	3,67	3,59	3,53
Ti	0,00	0,00	0,01	0,00	0,01	0,00	0,01	0,03	0,01	0,01
Fe	0,03	0,01	0,02	0,01	0,01	0,00	0,03	0,00	0,01	0,00
Mg	0,08	0,09	0,08	0,08	0,03	0,10	0,05	0,08	0,05	0,10
Ca	1,30	1,20	1,22	1,18	1,06	1,14	1,02	0,89	0,88	1,08
Mn	0,02	0,00	0,02	0,03	0,01	0,02	0,02	0,00	0,01	0,02
Na	0,09	0,16	0,14	0,17	0,16	0,17	0,20	0,23	0,26	0,14
K	0,87	0,94	1,13	0,96	1,43	1,02	1,49	1,43	1,62	1,26
E%	-4,59	-0,60	-7,04	-2,59	-2,32	-4,54	-8,06	1,76	-4,67	-6,68
R	0,70	0,70	0,70	0,70	0,69	0,70	0,70	0,69	0,70	0,70
Si/Al	2,31	2,28	2,29	2,32	2,23	2,36	2,34	2,27	2,32	2,37
Na/K	0,10	0,17	0,13	0,18	0,11	0,17	0,13	0,16	0,16	0,11
D/M	1,44	1,18	1,02	1,11	0,69	1,04	0,63	0,59	0,49	0,84

Table 4.15 (continued)

Quarry	SICAT	Cannetaccio (drill core)						Fantini		
Unit	UTGVTb	UTGVTa						UTGVTa		
Sample	C3_2	C1_12	C1_14	C1_17	C1_21	C1_23	C1_26	C4_1	C4_2	
Mean	n°3	n°5	n°3	n°3	n°2	n°2	n°3	n°2	n°3	n°6
SiO ₂	50,60	49,59	50,97	51,11	51,09	50,67	50,93	50,64	49,31	50,42
Al ₂ O ₃	18,43	18,63	19,02	17,92	18,35	18,45	17,99	18,87	17,74	18,08
TiO ₂	0,08	0,09	0,14	0,02	0,09	0,10	0,03	0,04	0,15	0,06
Fe ₂ O ₃	0,08	0,02	0,07	0,18	0,18	0,20	0,11	0,22	0,02	0,16
MgO	0,25	0,18	0,23	0,40	0,32	0,46	0,30	0,31	0,14	0,31
CaO	4,40	5,45	6,98	7,29	6,96	6,35	6,48	7,45	4,65	4,74
MnO	0,02	0,02	0,06	0,01	0,01	0,06	0,06	0,14	0,04	0,09
Na ₂ O	0,71	0,43	0,36	0,27	0,36	0,49	0,52	0,20	0,95	0,66
K ₂ O	8,34	6,43	4,48	3,97	4,38	4,36	4,50	4,11	8,12	7,87
H ₂ O	17,09	19,16	17,68	18,84	18,25	18,86	19,07	18,03	18,87	17,61
tot	82,91	80,84	82,32	81,16	81,75	81,14	80,93	81,97	81,13	82,39
Si	8,37	8,33	8,33	8,44	8,40	8,38	8,45	8,31	8,36	8,38
Al	3,59	3,69	3,66	3,49	3,55	3,60	3,52	3,65	3,55	3,54
Ti	0,01	0,01	0,02	0,00	0,01	0,01	0,00	0,00	0,02	0,01
Fe	0,01	0,00	0,01	0,02	0,02	0,02	0,01	0,03	0,00	0,02
Mg	0,06	0,05	0,06	0,10	0,08	0,11	0,08	0,08	0,04	0,08
Ca	0,78	0,98	1,22	1,29	1,22	1,13	1,15	1,31	0,84	0,84
Mn	0,00	0,00	0,01	0,00	0,00	0,01	0,01	0,02	0,01	0,01
Na	0,23	0,14	0,11	0,09	0,12	0,16	0,17	0,06	0,31	0,21
K	1,76	1,38	0,93	0,84	0,92	0,92	0,95	0,86	1,76	1,67
E%	-2,17	3,11	1,08	-5,76	-2,50	0,70	-2,12	-2,25	-7,69	-5,57
R	0,70	0,69	0,69	0,71	0,70	0,70	0,71	0,69	0,70	0,70
Si/Al	2,33	2,26	2,27	2,42	2,36	2,33	2,40	2,28	2,36	2,37
Na/K	0,13	0,10	0,12	0,10	0,13	0,17	0,18	0,07	0,18	0,13
D/M	0,42	0,68	1,22	1,50	1,26	1,15	1,09	1,50	0,43	0,49

Table 4.16 : Chemical analyses (wt%) and unit-cell content of phillipsite (calculated on 32 oxygens)

Quarry	Perina									
Unit	UTGVTb					UTGVTa				
Sample	CV_1	CV_3	CV_5	CV_9	CV_13	CV_17	CV_24	C2_P1_1		C2_P2_1
Mean	n°3	n°3	n°3	n°2	n°2	n°4	n°4	n°3	n°4	n°6
SiO2	53,05	52,65	53,51	52,89	53,05	52,17	53,50	54,46	54,76	53,79
Al2O3	18,21	18,80	18,70	18,72	20,17	19,73	19,13	18,26	19,13	18,56
TiO2	0,13	0,15	0,09	0,27	0,33	0,13	0,25	0,17	0,11	0,25
Fe2O3	0,17	0,31	0,15	0,10	0,11	0,16	0,15	0,01	0,23	0,04
MgO	0,01	0,06	0,15	0,00	0,03	0,11	0,00	0,01	0,36	0,00
CaO	4,56	3,77	3,67	3,39	3,86	4,08	2,73	1,69	5,14	3,13
MnO	0,08	0,11	0,04	0,05	0,05	0,20	0,02	0,07	0,02	0,04
Na2O	0,67	1,74	1,06	1,40	1,59	1,57	1,44	1,77	0,85	1,08
K2O	9,53	8,56	9,33	9,50	9,56	9,50	11,31	11,24	8,37	11,02
H2O	13,58	13,85	13,28	13,68	11,24	12,35	11,46	12,32	11,03	12,10
tot	86,42	86,15	86,72	86,32	88,76	87,65	88,54	87,68	88,97	87,90
Si	11,29	11,20	11,30	11,25	11,01	10,99	11,20	11,45	11,23	11,30
Al	4,57	4,71	4,65	4,69	4,93	4,90	4,72	4,52	4,63	4,60
Ti	0,02	0,02	0,02	0,04	0,05	0,02	0,04	0,03	0,02	0,04
Fe	0,03	0,05	0,02	0,02	0,02	0,03	0,02	0,00	0,03	0,01
Mg	0,00	0,02	0,05	0,00	0,01	0,03	0,00	0,00	0,11	0,00
Ca	1,04	0,86	0,83	0,77	0,86	0,92	0,61	0,38	1,13	0,70
Mn	0,01	0,02	0,01	0,01	0,01	0,04	0,00	0,01	0,00	0,01
Na	0,28	0,72	0,43	0,58	0,64	0,64	0,58	0,72	0,34	0,44
K	2,59	2,32	2,51	2,58	2,53	2,55	3,02	3,01	2,19	2,95
E%	-8,19	-2,60	-1,33	-0,53	0,15	-5,31	-2,50	0,01	-7,72	-4,54
R	0,71	0,70	0,71	0,71	0,69	0,69	0,70	0,72	0,71	0,71
Si/Al	2,47	2,38	2,43	2,40	2,23	2,24	2,37	2,53	2,43	2,46
Na/K	0,11	0,31	0,17	0,22	0,25	0,25	0,19	0,24	0,15	0,15
D/M	0,36	0,29	0,30	0,25	0,27	0,30	0,17	0,10	0,49	0,21

Table 4.16 (continued)

Quarry	SICAT	Cannetaccio Drill core			Fantini	
Unit	UTGVtb	UTGVta			UTGVta	
Sample	C3_2	C1_5	C1_6	C1_12	C4_2	
Mean	n°4	n° 3	n° 6	n° 2	n°2	n°2
SiO ₂	52,44	53,47	53,68	54,15	53,64	53,47
Al ₂ O ₃	19,24	18,11	18,75	18,82	18,32	18,81
TiO ₂	0,39	0,06	0,02	0,17	0,29	0,35
Fe ₂ O ₃	0,17	0,00	0,25	0,00	0,16	0,11
MgO	0,00	0,04	0,04	0,00	0,00	0,03
CaO	3,64	3,38	4,53	3,93	2,09	3,24
MnO	0,05	0,07	0,07	0,00	0,00	0,01
Na ₂ O	1,25	1,37	1,37	1,66	1,48	1,92
K ₂ O	10,73	9,19	8,47	9,04	11,56	9,70
H ₂ O	12,11	14,30	12,83	12,23	12,45	12,38
tot	87,89	85,70	87,17	87,77	87,55	87,62
Si	11,07	11,41	11,26	11,30	11,34	11,23
Al	4,78	4,55	4,64	4,63	4,57	4,65
Ti	0,06	0,01	0,00	0,03	0,05	0,06
Fe	0,03	0,00	0,04	0,00	0,03	0,02
Mg	0,00	0,01	0,01	0,00	0,00	0,01
Ca	0,82	0,77	1,02	0,88	0,47	0,73
Mn	0,01	0,01	0,01	0,00	0,00	0,00
Na	0,51	0,57	0,56	0,67	0,61	0,78
K	2,89	2,50	2,27	2,41	3,12	2,60
E%	-5,42	-2,37	-5,60	-4,30	-2,26	-4,10
R	0,70	0,71	0,71	0,71	0,71	0,71
Si/Al	2,31	2,51	2,43	2,44	2,48	2,41
Na/K	0,18	0,23	0,24	0,28	0,20	0,30
D/M	0,24	0,26	0,36	0,29	0,13	0,22

Table 4.17: Chemical analyses (wt%) and unit-cell content of analcime (calculated on 96 oxygens)

Quarry	Cannetaccio				
Unit	UTGVTa				
Sample	C1_6	C1_12	C1_17	C1_23	C1_26
Mean	n° 5	n° 4	n° 4		n° 5
SiO ₂	55,09	57,27	56,68	55,38	55,02
Al ₂ O ₃	21,31	22,03	21,11	21,13	21,86
TiO ₂	0,15	0,16	0,06	0,08	0,07
Fe ₂ O ₃	0,69	0,76	0,69	0,70	0,20
MgO	0,03	0,09	0,05	0,10	0,01
CaO	0,46	0,59	0,30	0,36	0,39
MnO	0,05	0,05	0,07	0,11	0,06
Na ₂ O	11,64	11,61	11,57	10,95	12,11
K ₂ O	0,44	0,58	0,50	0,52	0,71
H ₂ O	10,15	6,87	8,98	10,68	9,57
tot	89,85	93,13	91,02	89,32	90,43
Si	32,85	32,92	33,28	33,11	32,67
Al	14,98	14,93	14,61	14,88	15,29
Ti	0,07	0,07	0,03	0,03	0,03
Fe	0,31	0,33	0,30	0,32	0,09
Mg	0,02	0,07	0,04	0,08	0,01
Ca	0,29	0,36	0,19	0,23	0,25
Mn	0,03	0,02	0,04	0,06	0,03
Na	13,45	12,94	13,16	12,69	13,94
K	0,34	0,42	0,37	0,40	0,53
E%	3,51	4,55	3,84	7,66	1,57
R	0,69	0,69	0,69	0,69	0,68
Si/Al	2,19	2,21	2,28	2,22	2,14
Na/K	39,72	30,47	35,52	32,00	26,06
D/M	0,02	0,03	0,02	0,02	0,02

Table 4.19: Chemical analyses (wt%) and Barth's standard cell content of the glasses (calculated on 160 oxygens)

	White pumice	Black-grey scoria	White pumice	Black-grey scoria
Unit	UTGVTa		UTGVTb	
Sample	A3		B2	
Mean	n°6	n°6	n°7	n°3
SiO ₂	56,80	54,67	57,48	54,23
Al ₂ O ₃	20,20	19,20	20,73	18,78
TiO ₂	0,46	0,69	0,38	0,72
FeO	3,57	5,53	2,90	6,18
MgO	0,51	1,10	0,32	1,23
CaO	4,42	6,70	3,91	8,14
MnO	0,13	0,10	0,15	0,29
Na ₂ O	4,28	4,24	4,64	4,37
K ₂ O	9,40	7,68	9,41	6,06
BaO	0,22	0,36	0,16	0,42
Cl	0,12	0,08	0,09	0,10
tot	100	100	100	100
Si	53,50	51,87	53,85	51,41
Al	22,42	21,47	22,88	20,98
Ti	0,33	0,49	0,27	0,51
Fe	2,53	3,95	2,04	4,41
Mg	0,71	1,56	0,45	1,74
Ca	4,46	6,81	3,92	8,27
Mn	0,10	0,08	0,12	0,23
Na	7,82	7,79	8,42	8,03
K	11,30	9,30	11,24	7,33
Ba	0,08	0,13	0,06	0,16
Si/Al	2,39	2,42	2,35	2,45
Na/K	0,69	0,84	0,75	1,10

The chemical composition of chabazite, phillipsite and glass were plotted on the triangular mole diagrams (figure 4.24), where the exchangeable cations content is reported. The chemical analysis of the present research are compared to literature data (Cappelletti et al., 1999; de' Gennaro et al., 1995, Masotta et al., 2010).

Figure 4.24a shows a very wide calcium range, and it allow to be distinguish chabazites with Ca as main extra-framework cation, from those with K as main extra-framework cation. Figure 4.24b plotted the phillipsite chemical component, showing that this zeolite have potassium as main extra-framework cation followed by calcium; phillipsites plot in the field marked by a rather uniform content of K. Both chabazite and phillipsite data were compared to glass composition, and the diagram easily distinguish the two type of glasses; it also show the lower Na content of zeolites than of the glass; Na is the first element that was leached after the hydrolysis of glassy fraction. The joint occurrence of chabazite and phillipsite suggests a potassic environment for these zeolites. The high Ca content of zeolites can be attributed to Ca-rich solution, due to dissolution of calcareous clasts from the initial acidic solution.

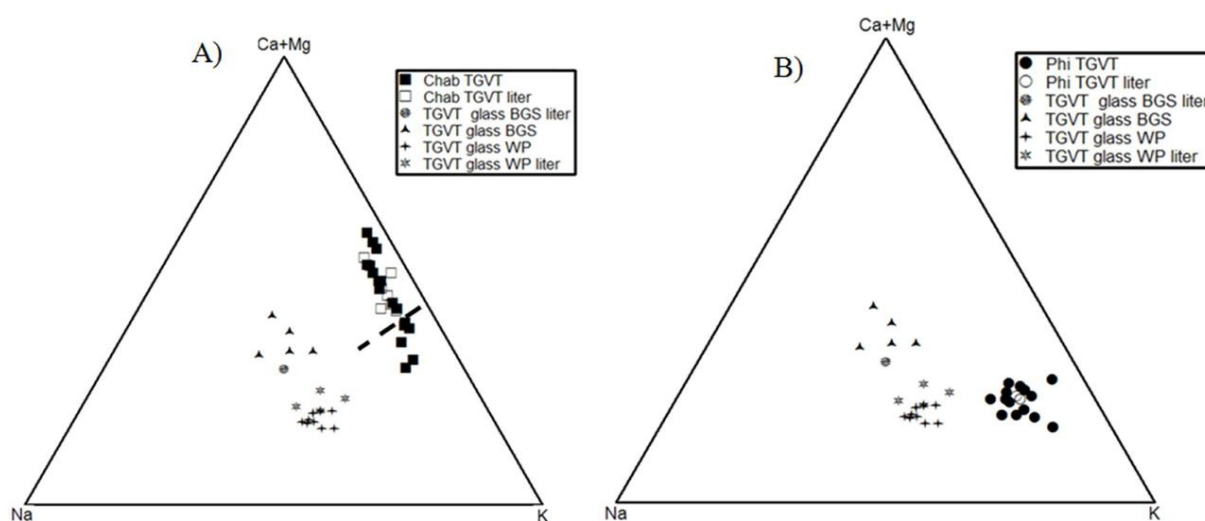


Figure 4.24: ternary diagrams a) chabazite and glass, the dotted line distinguished the Ca-chabazites from K-chabazites; b) phillipsite and glass.

Chemical compositions of zeolites and glass of UTGVT formation were compared with chemical data of chabazite, phillipsite and glass of others central-southern Italian volcanoclastic formations such as Neapolitan Yellow Tuff (NYT) and Campanian Ignimbrite (CI) (figure 4.25).

Figure 4.25a shows that chabazites from UTGVT formation have similar chemical composition compared to the same zeolite of CI formation; whereas they have a lower content of Na in regard to the NYT chabazites. Also phillipsites of UTGVT have similar composition of CI

phillipsites, and they display lower content of Na compared to the same zeolite of NYT formation (Figure 4.25b).

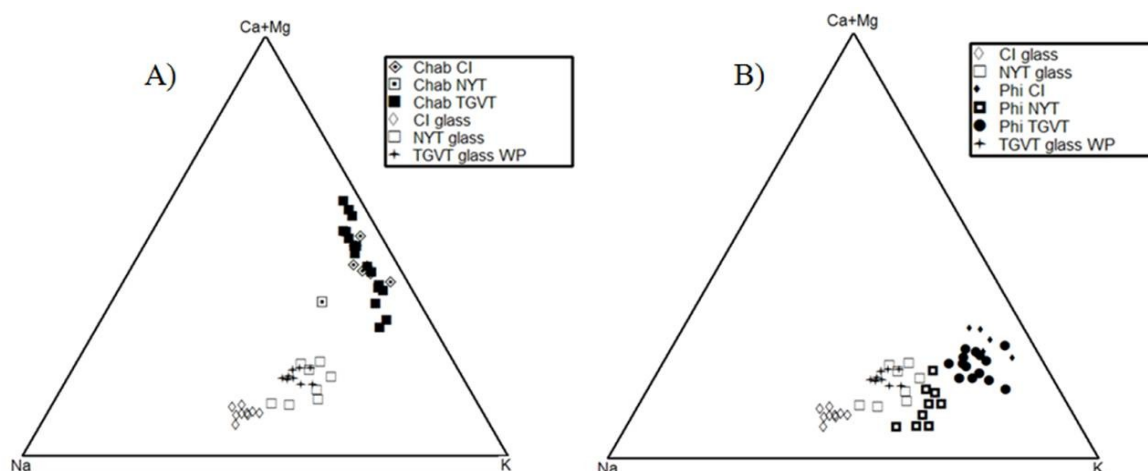


Figure 4.25: ternary diagrams a) chabazite and glass (TGVT-CI-NYT); b) phillipsite and glass (TGVT-CI-NYT)

The triangular mole diagrams in figure 4.25, show that the UTGVT and CI formations have zeolites with similar chemical compositions, although the precursor glasses have different compositions. Notwithstanding UTGVT and NYT formations have quite similar glass composition, they gave rise to zeolite with different alkali-composition.

Further information on difference between the precursor glasses of UTGVT, NYT and CI, from which derive chabazite and phillipsite, are reported in figure 4.26. Diagram shows the comparison between alkaline oxides content and Si/Al ratio of UTGVT, NYT and CI glasses. The UTGVT and NYT glasses show similar alkaline composition; despite this similar glass composition, UTGVT zeolites have higher K values than the same zeolites of NYT formation. The chemical composition of glass often play an important role in determining the type of authigenic minerals, but for the UTGVT formation, the aforementioned features suggested an important role in the crystallization of zeolites from glass exerted by solutions.

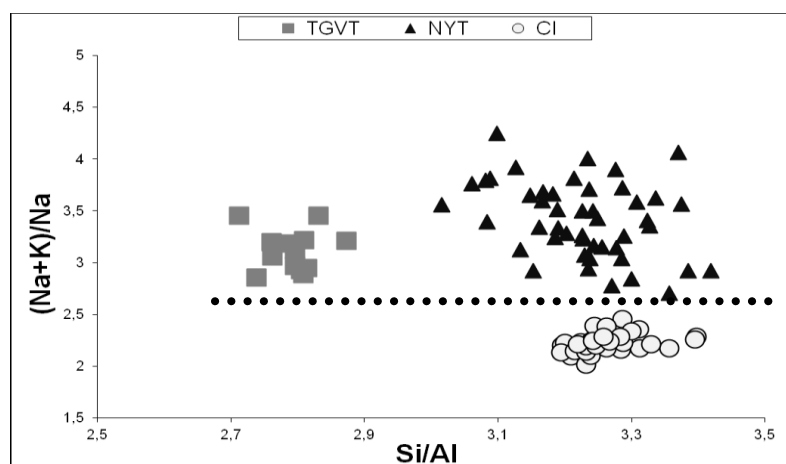


Figure 4.26: Binary diagram Si/Al vs (Na+K)/Na

In order to better understand the typical variation that occurs during the glass-to-zeolite transformation; mole oxides content (SiO_2 ; Al_2O_3 , CaO , Na_2O , K_2O) against mole water content of glass, phillipsite and chabazite, belonging to the most representative sample examined, were plotted in a binary diagram (figure 4.27). Diagram shows a constant Si content in the glass-to-phillipsite transformation, while it decreases in glass-to-chabazite transformation; Al remained nearly constant, therefore the Si/Al ratio slightly decrease in the glass-to-phillipsite-to-chabazite zeolitization process. The glass-to phillipsite transformation does not involve clear variation in oxides content, whereas the glass-to-chabazite transformation determines a decrease of Na_2O and K_2O , while increase the CaO content.

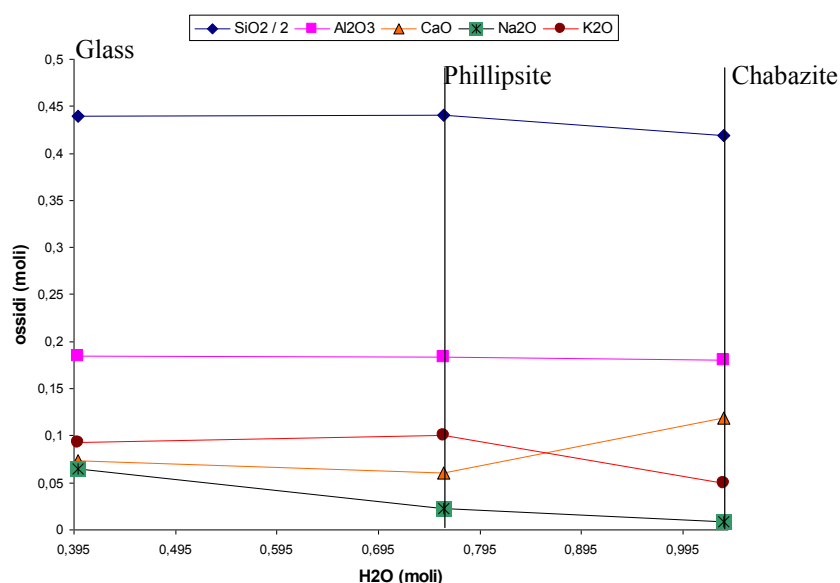


Figure 4.27: Oxide variation during glass-to zeolite conversion process plotted against water content of each phase

On the basis of SEM observations, that allow to distinguish pyrogenic and authigenic feldspars, chemical analyses on polished thin section were carried out, in order to identify possible compositional differences between them. Table 4.19 reports the chemical composition of pyrogenic and authigenic feldspars, and the unit-cell contents calculated on 8 oxygen atoms. The chemical data were plotted in triangular albite – anorthite – orthoclase diagram, where it is possible to clearly distinguish the pyrogenic ones from authigenic feldspars, in particular the authigenic feldspars cluster towards the Or end member, while the pyrogenic feldspars scatter towards the Ab end member, with an increase in the Or molecule (figure 4.28).

Authigenic feldspars have a higher K content (>95 wt%) than the pyrogenic feldspars (≤ 90 wt%); the chemical composition, compared to SEM observations, identify this authigenic mineral as adularia.

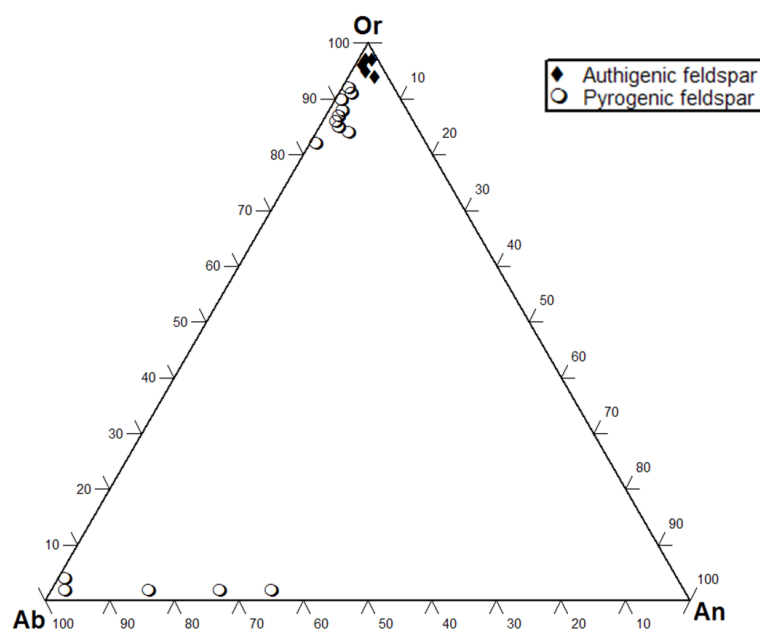


Figure 4.28: Triangular diagram Ab-An-Or

Table 4.19: chemical analysis of pyrogenic feldspars, and unit-cell content calculated on 8 oxygen atoms

Quarry	Perina										
	Sample	CV1	CV_9	CV_13	CV_17	CV_27	CV_30	C2_P1_1		C2_P2_1	
SiO ₂	64,67	64,58	65,88	63,38	64,50	65,57	64,65	65,20	58,51	61,76	67,38
Al ₂ O ₃	18,95	19,25	19,64	18,92	19,57	19,57	18,97	19,28	24,92	19,02	19,67
TiO ₂	0,28	0,00	0,18	0,00	0,00	0,40	0,06	0,00	0,17	0,00	0,19
Fe ₂ O ₃	0,08	0,00	0,00	0,00	0,11	0,00	0,18	0,18	0,12	0,25	0,00
MgO	0,02	0,00	0,00	0,02	0,06	0,00	0,00	0,00	0,00	0,00	0,00
CaO	0,33	0,46	0,36	0,43	0,35	0,32	0,30	0,30	7,21	0,28	0,19
MnO	0,38	0,00	0,02	0,00	0,18	0,00	0,00	0,00	0,04	0,00	0,08
Na ₂ O	1,24	1,02	1,24	1,34	1,12	0,78	1,08	1,93	7,46	1,03	11,49
K ₂ O	15,19	14,57	15,25	14,59	14,59	15,27	15,57	14,52	0,32	14,63	0,72
SrO	0,24	0,69	0,23	0,00	0,30	0,66	0,54	1,05	0,64	1,10	0,23
BaO	0,04	0,05	0,00	0,67	0,41	0,00	0,23	0,45	0,00	0,57	0,00
tot	101,39	100,61	102,80	99,35	101,20	102,56	101,57	102,90	99,40	98,64	99,94
Si	2,96	2,97	2,96	2,96	2,95	2,96	2,97	2,96	2,65	2,94	2,97
Al	1,02	1,04	1,04	1,04	1,06	1,04	1,03	1,03	1,33	1,07	1,02
Ti	0,01	0,00	0,01	0,00	0,00	0,01	0,00	0,00	0,01	0,00	0,01
Fe	0,00	0,00	0,00	0,00	0,00	0,00	0,01	0,01	0,00	0,01	0,00
Mg	0,00	0,00	0,00	0,00	0,00	0,00	0,00	0,00	0,00	0,00	0,00
Ca	0,02	0,02	0,02	0,02	0,02	0,02	0,01	0,01	0,35	0,01	0,01
Mn	0,01	0,00	0,00	0,00	0,01	0,00	0,00	0,00	0,00	0,00	0,00
Na	0,11	0,09	0,11	0,12	0,10	0,07	0,10	0,17	0,66	0,09	0,98
K	0,89	0,85	0,87	0,87	0,85	0,88	0,91	0,84	0,02	0,89	0,04
Sr	0,01	0,02	0,01	0,00	0,01	0,02	0,01	0,03	0,02	0,03	0,01
Ba	0,00	0,00	0,00	0,01	0,01	0,00	0,00	0,01	0,00	0,01	0,00
E%	-3,62	5,26	2,13	0,48	4,73	6,44	-0,99	-0,77	-3,38	5,47	-2,33
R	0,74	0,74	0,74	0,74	0,74	0,74	0,74	0,74	0,67	0,73	0,74
Si/Al	2,90	2,85	2,85	2,84	2,80	2,84	2,89	2,87	1,99	2,75	2,91
X	1,01	0,97	1,00	1,03	0,99	0,98	1,04	1,06	1,02	1,00	1,03
Z	3,98	4,01	4,00	4,00	4,01	4,00	3,99	3,99	3,98	4,01	3,99

Table 4.19 continued

Quarry	SICAT		Cannetaccio							Fantini			
Sample	C3_2		C1_1	C1_5	C1_6	C1_21		C1_23	C1_26	C4_1		C4_2	
SiO ₂	62,92	63,96	64,29	65,50	62,04	62,24	64,70	60,11	64,94	62,62	66,74	67,14	62,36
Al ₂ O ₃	22,11	18,56	19,28	19,43	18,94	20,97	18,75	23,33	23,20	19,30	20,24	19,69	18,60
TiO ₂	0,14	0,01	0,15	0,25	0,15	0,00	0,05	0,08	0,00	0,37	0,00	0,00	0,10
Fe ₂ O ₃	0,16	0,00	0,14	0,06	0,00	1,03	0,17	0,10	0,00	0,01	0,00	0,00	0,28
MgO	0,03	0,00	0,05	0,00	0,08	0,13	0,00	0,00	0,14	0,00	0,00	0,15	0,00
CaO	3,30	0,09	0,28	0,47	0,39	3,55	0,26	5,31	4,01	0,38	0,03	0,46	0,45
MnO	0,04	0,06	0,00	0,09	0,05	0,08	0,06	0,02	0,00	0,00	0,00	0,18	0,30
Na ₂ O	9,96	0,79	0,75	1,09	1,07	2,62	1,17	7,98	9,75	0,71	11,37	11,36	1,04
K ₂ O	0,24	16,13	15,60	15,28	14,65	10,35	14,67	0,42	0,01	14,87	0,33	0,30	14,40
SrO	0,26	0,47	0,00	0,00	0,73	0,92	0,66	1,16	0,00	0,19	0,24	0,00	0,00
BaO	0,02	0,32	0,00	0,00	0,00	0,44	0,15	0,00	0,17	0,00	0,29	0,00	0,00
tot	99,20	100,39	100,55	102,18	98,10	102,33	100,64	98,52	102,22	98,44	99,24	99,26	97,52
Si	2,82	2,98	2,95	2,96	2,94	2,83	2,98	2,74	2,81	2,94	2,96	2,97	2,95
Al	1,17	1,02	1,04	1,03	1,06	1,12	1,02	1,25	1,18	1,07	1,06	1,02	1,04
Ti	0,00	0,00	0,01	0,01	0,01	0,00	0,00	0,00	0,00	0,01	0,00	0,00	0,00
Fe	0,01	0,00	0,00	0,00	0,00	0,04	0,01	0,00	0,00	0,00	0,00	0,00	0,01
Mg	0,00	0,00	0,00	0,00	0,01	0,01	0,00	0,00	0,01	0,00	0,00	0,01	0,00
Ca	0,16	0,00	0,01	0,02	0,02	0,17	0,01	0,26	0,19	0,02	0,00	0,02	0,02
Mn	0,00	0,00	0,00	0,00	0,00	0,00	0,00	0,00	0,00	0,00	0,00	0,01	0,01
Na	0,86	0,07	0,07	0,10	0,10	0,23	0,10	0,71	0,82	0,06	0,98	0,97	0,10
K	0,01	0,96	0,91	0,88	0,89	0,60	0,86	0,02	0,00	0,89	0,02	0,02	0,87
Sr	0,01	0,01	0,00	0,00	0,02	0,02	0,02	0,03	0,00	0,01	0,01	0,00	0,00
Ba	0,00	0,01	0,00	0,00	0,00	0,01	0,00	0,00	0,00	0,00	0,00	0,00	0,00
E%	-2,98	-2,40	2,72	0,52	1,83	-6,41	2,07	0,26	-2,07	7,45	5,85	-3,82	0,26
R	0,71	0,75	0,74	0,74	0,74	0,72	0,75	0,69	0,70	0,73	0,74	0,74	0,74
Si/Al	2,41	2,92	2,83	2,86	2,78	2,52	2,93	2,19	2,38	2,75	2,80	2,89	2,85
X	1,04	1,03	1,00	1,00	1,03	1,05	1,00	1,02	1,02	0,97	1,00	1,02	0,99
Z	3,98	3,99	4,00	3,99	4,00	3,95	4,00	4,00	3,99	4,01	4,01	3,99	3,99

Table 4.19 continued: chemical analysis of authigenic feldspars, and unit-cell content calculated on 8 oxygen atoms

Quarry	Perina			Cannetaccio		
Sample	CV_3	CV_28	CV_36	C1_6	C1_26	C1_29
SiO ₂	61,96	63,84	62,49	62,42	64,51	65,71
Al ₂ O ₃	18,03	19,14	17,79	17,82	18,57	18,93
TiO ₂	0,00	0,18	0,19	0,14	0,12	0,01
Fe ₂ O ₃	0,15	0,25	0,22	0,32	0,30	0,00
MgO	0,03	0,00	0,36	0,22	0,00	0,07
CaO	0,82	0,23	0,41	0,25	0,13	0,35
MnO	0,00	0,00	0,08	0,26	0,08	0,11
Na ₂ O	0,21	0,29	0,09	0,17	0,29	0,34
K ₂ O	16,02	16,44	15,82	16,12	16,90	16,55
SrO	0,20	0,00	0,00	0,00	0,35	0,00
BaO	0,17	0,00	0,00	0,00	0,03	0,11
tot	97,58	100,38	97,46	97,71	101,28	102,19
Si	2,96	2,95	2,97	2,97	2,97	2,98
Al	1,02	1,04	1,00	1,00	1,01	1,01
Ti	0,00	0,01	0,01	0,01	0,00	0,00
Fe	0,01	0,01	0,01	0,01	0,01	0,00
Mg	0,00	0,00	0,03	0,02	0,00	0,00
Ca	0,04	0,01	0,02	0,01	0,01	0,02
Mn	0,00	0,00	0,00	0,01	0,00	0,00
Na	0,02	0,03	0,01	0,02	0,03	0,03
K	0,98	0,97	0,96	0,98	0,99	0,96
Sr	0,01	0,00	0,00	0,00	0,01	0,00
Ba	0,00	0,00	0,00	0,00	0,00	0,00
E%	-6,33	2,40	-6,54	-6,75	-2,90	-2,60
R	0,74	0,74	0,75	0,75	0,75	0,75
Si/Al	2,92	2,83	2,98	2,97	2,95	2,95
X	1,04	1,01	1,01	1,02	1,04	1,01
Z	3,98	3,99	3,97	3,97	3,98	3,99

In the second phase of the research a further detailed investigation was carried out on zeolite-enriched samples, through thermal analyses: thermogravimetry (TG), and differential thermal analysis (DTA). Also thermodynamic modeling was carried out to calculate stability fields of zeolites, including chabazite, phillipsite, and analcime. These models allow to identify the favorable temperature, within the flow units, suitable for the crystallization of different zeolites.

4.4. PHASE CONCENTRATION

Enrichment of zeolites (chabazite, phillipsite), was obtained using a series of techniques based on the different physical behavior of the various constituents.

Starting from XRPD data, samples that showed the highest percentage of chabazite or phillipsite, were selected to carry out zeolites enrichment. For this purpose the following samples have been selected: C5_1 and CV_17 belong to Fantini and Perina quarries. The former shows an initial chabazite content about 64 wt%, whereas the latter has a phillipsite content about 40 wt% (table 4.20).

Tabella 4.20: Quantitative XRPD analyses (RIR) of enriched samples (wt.%).

Sample	Smectite %	Biotite %	Chabasite %	Phillipsite %	Feldspar %	Calcite %	Total %	Amorphous
C5_1	7 (\pm 1)	0	64 (\pm 4)	4 (\pm 1)	9 (\pm 2)	12 (\pm 1)	95 (\pm 7)	5
CV_17	4 (\pm 1)	tr	11 (\pm 1)	40 (\pm 2)	18 (\pm 8)	11 (\pm 1)	84 (\pm 12)	16

Error in brackets = $\sqrt{\sigma_1^2 + \sigma_2^2 + \dots}$ (Chipera and Bish, 1995), amorphous % by difference

The phase concentration allowed to obtain an enriched sample reaching chabazite content > 90 wt%, along with minor amount of phillipsite. Phillipsite-enriched sample reaches a content of this zeolite about 76 wt% with 5 wt% of chabazite and 12 wt% of feldspar.

Table 4.21 reports the quantitative mineralogical data of enriched samples.

Tabella 4.21: Quantitative XRPD analyses (RIR) of enriched samples (wt.%).

Sample	Chabasite %	Phillipsite %	Feldspar %	Total %	Amorphous
C5_1	95 (\pm 7)	2 (\pm 1)	0	97 (\pm 8)	3
CV_17	5 (\pm 1)	76 (\pm 4)	12 (\pm 3)	93 (\pm 8)	7

Error in brackets = $\sqrt{\sigma_1^2 + \sigma_2^2 + \dots}$ (Chipera and Bish, 1995), amorphous % by difference

4.5. THERMAL ANALYSIS

A further detailed investigation was carried out on zeolite-enriched samples, through thermal analyses: thermogravimetry (TG), and differential thermal analysis (DTA). Figure 4.29 shows the TG and DTA curves of chabazite and phillipsite of enriched samples.

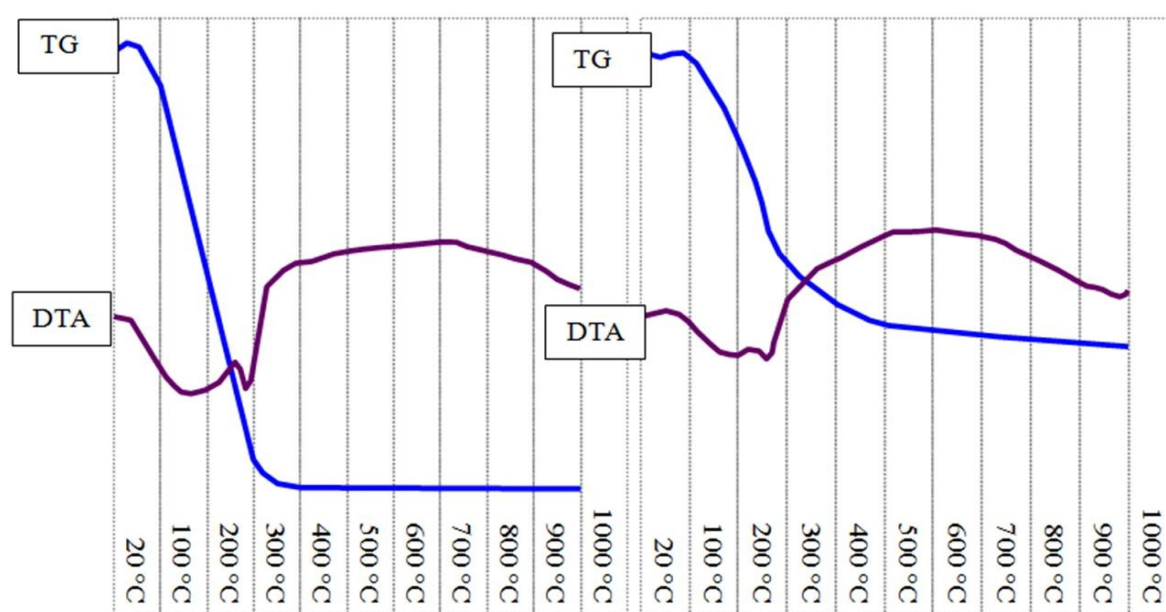


Figure 4.29: Thermal analyses of zeolites enriched samples; left chabazite-enriched sample, right, phillipsite-enriched sample

DTA curve of chabazite-enriched sample shows a first endothermic peak around 150°C, which led to the loss of most water molecules from the structure; a second endothermic peak, less accentuated, is recorded around 300°C, where the remainder of the framework water was lost, which led to the collapse of the zeolite framework. The total weight loss of the sample is about 18 wt%, this value can be considered available also for chabazite, due to high percentage (95 wt%) of this zeolite in the analyzed sample.

Phillipsite-enriched sample shows a DTA curve with a first endothermic peak around 150°C, with a second peak around 280°C (zeolite framework collapse), in this case the weight loss of the sample is about 12 wt%.

4.6. THERMADINAMIC MODEL

Thermodynamic parameters affecting the crystallization of different zeolites was well represented by calculated stability diagrams. During the simulation it is considered a water activity fixed to 1, while a silica activity value of -2.7 was considered; such condition were

chosen in order to allow analcime crystallization. The resulting diagrams showed that phillipsite and chabazite crystallization primarily depend on K, Ca, and Na activities in solution, while analcime crystallization depends on both temperature, in particular it does not form below 120°C, and Na activities (figure 4.30). This results confirm the important role of chemical composition of solution for the crystallization of chabazite or phillipsite.

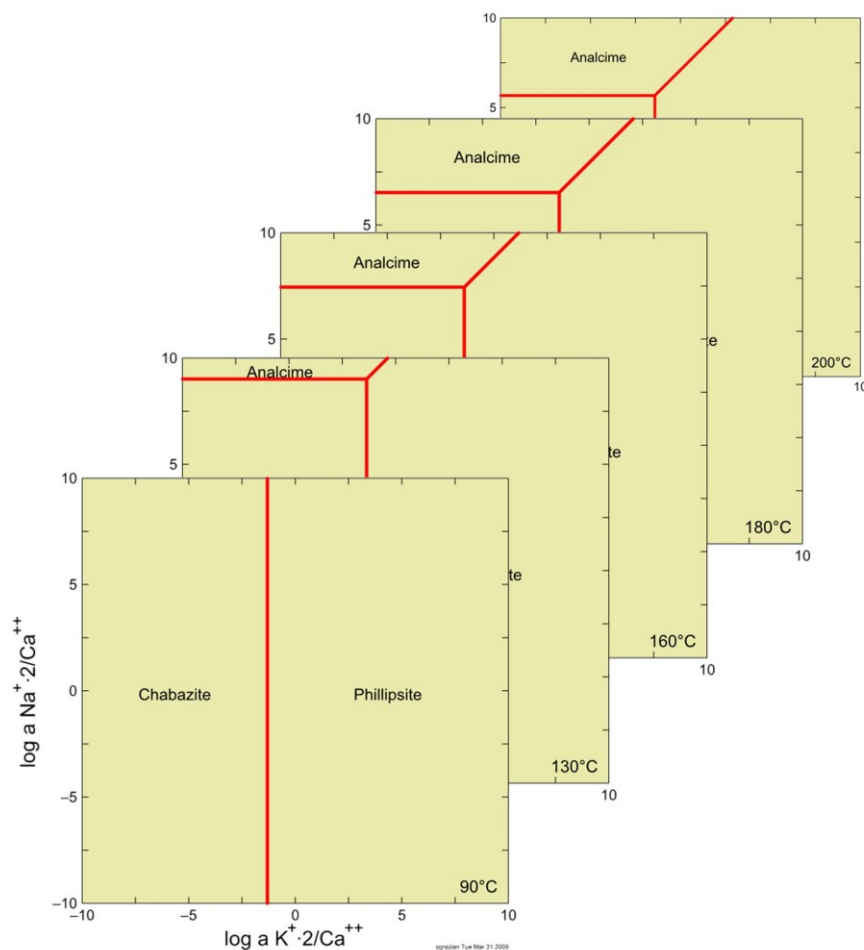


Figure 4.30: Stability fields of zeolites

The crystallization of authigenic minerals plays an important role in the lithification process of volcanoclastic deposit, also influencing the physic-mechanical features of material. Previous works (Langella et al., 2002, Colella et al., 2009) showed that high zeolites content determines high compressive strength values. In the last phase of the research, the physic-mechanical characterization of UTGVT formation were performed, in order to better understand the lithification process.

4.7. PHYSIC-MECHANICAL CHARACTERIZATION

The petrophysical characterization is carried out at “Laboratorio per la Caratterizzazione Petrofisica dei Lapidei Ornamentali e la Diagnostica dei Geomateriali” of University of Naples Federico II.

During the early phases of physic-mechanical characterization the determination of: appearance volume, appearance density, bulk volume and bulk density were performed, afterwards it was calculated the porosity for all investigated samples. Table 4.22 reports the features of the investigated samples; they shows a quite constant values both of appearance volume and density, ranging between 11-14 cm³ and 1.16-1.32 g/cm³, respectively; whereas they have a values of bulk volume and density, ranging between 5.96 - 7.79 cm³, 2.27-2.44 g/cm³. As regards the porosity, samples belong to Perina quarry shows a slightly higher average value, about 49 wt%, compared to those from Cannetaccio and Fantini quarries, with an average porosity of about 47 wt%.

Table 4.22: Geometric features and values of porosity

Quarry	Sample	Weight g	Height cm	Diameter cm	Apparent volume cm ³	Apparent density g/cm ³	Bulk volume cm ³	Bulk density g/cm ³	Open porosity %	Average open porosity
Cannetaccio	C1	17,33	2,7	2,53	13,57	1,28	7,12	2,43	47,52	47,42
	C2	17,29	2,65	2,55	13,53	1,28	7,28	2,38	46,18	
	C3	17,33	2,7	2,53	13,57	1,28	7,14	2,43	47,37	
	C4	15,05	2,3	2,53	11,56	1,30	6,17	2,44	46,61	
	C5	14,51	2,31	2,55	11,79	1,23	5,96	2,43	49,45	
	C6	17,22	2,7	2,53	13,57	1,27	7,14	2,41	47,37	
Perina	P1	16,40	2,8	2,52	13,96	1,17	7,04	2,33	49,56	49,60
	P2	15,93	2,8	2,51	13,85	1,15	6,81	2,34	50,82	
	P3	17,31	2,82	2,53	14,17	1,22	7,33	2,36	48,27	
	P4	16,01	2,75	2,53	13,82	1,16	6,84	2,34	50,50	
	P5	16,78	2,78	2,55	14,19	1,18	7,05	2,38	50,32	
	P6	17,12	2,78	2,55	14,19	1,21	7,2	2,38	49,26	
	P7	17,23	2,83	2,52	14,11	1,22	7,27	2,37	48,47	
Fantini	F1	17,05	2,72	2,55	13,88	1,23	7,41	2,30	46,63	47,21
	F2	16,73	2,8	2,52	13,96	1,20	7,37	2,27	47,20	
	F3	18,23	2,7	2,55	13,78	1,32	7,79	2,34	43,48	
	F4	16,72	2,82	2,55	14,39	1,16	7,31	2,29	49,22	
	F5	16,96	2,75	2,55	14,04	1,21	7,39	2,29	47,35	
	F6	16,02	2,61	2,58	13,64	1,17	6,9	2,32	49,41	

High values of open porosity should be related to the particular texture of the rock with abundant pumices and lithics set in a ashy matrix.

Afterwards the determination of porosity through Hg – porosimetry was obtained and results are reported in figure 4.31. As far as pore distribution is considered, UTGVT shows a unimodal distribution characterized by a single class within the macropores field (0.1 - 1 μ m).

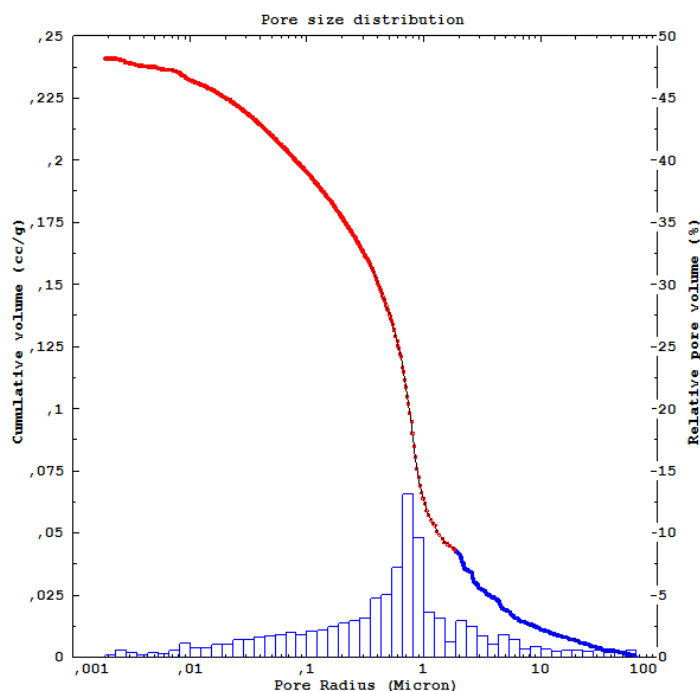


Figure 4.31: Pore size distribution obtained by Hg-porosimetry in a TGVT sample

Average pore radius and specific surface of UTGVT were determined by means of Hg-porosimetry; the former has a value of 0.72 μm , while the latter is 6.81 m^2/g , finally a porosity value of about 35 wt% (table 4.23) was calculated. Hg-porosimetry does not allow to measure volume and size of micropores size class.

Table 4.23: Parameters determined by Hg-porosimetry on TGVT sample

Mean pore radius μm	Specific surface m^2/g	Porosity wt%
0.72	6.81	35.38

4.7.1. TOTAL ABSORPTION WATER (UNI EN 13755)

Further information on rocks porosity was obtained by measuring the water absorption. Water absorption by total immersion tests revealed the high attitude of those materials to fluid circulation, linked to the occurrence of a net of interconnected pores.

Three samples for each quarry in order to determine the water absorption was selected. Table 4.24 reports the water adsorption coefficient, the average water absorption and standard deviation for each sample; where samples, belong to Perina quarry, samples have an average water absorption coefficient (about 24 wt%) higher than of Cannetaccio and Fantini quarries

Dott. Gianmarco Rapisardo. Scuola di dottorato in Scienze della Natura e delle sue Risorse. 118

Indirizzo: Scienza e tecnologia dei Minerali e delle rocce di interesse industriale. XXV ciclo.

Post-emplacement minerogenetic processes in Upper Tufo Giallo della Via Tiberina (Latium): a mineralogical and volcanological approach

(about 22 wt%). This high value of average water absorption is in agreement with the aforementioned higher porosity.

Table 4.24: Imbibition coefficient (IC wt%)

Quarry	Sample	IC wt%	Average(wt%)	Stand. Dev
Cannetacio	CV_4	23,19	22,73	0,33
	CV_5	22,50		
	CV_6	22,49		
Perina	C2_4	24,26	24,46	0,61
	C2_5	25,28		
	C2_6	23,84		
Fantini	C4_4	21,95	22,09	0,30
	C4_5	21,82		
	C4_6	22,50		

Results of water absorption were highlighted by graphics of figures 4.32, 4.33 and 4.34, that showed the water absorption variation as time function.

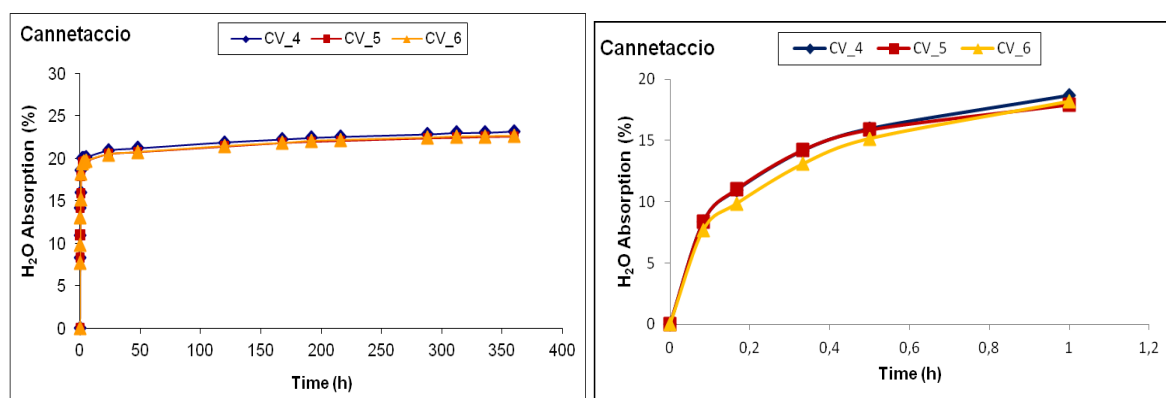


Figure 4.32: Total water absorption curves for Cannetaccio quarry samples (UNI-EN 13755). On the right is reports the shape of the curves in the time interval between 0h and 1h

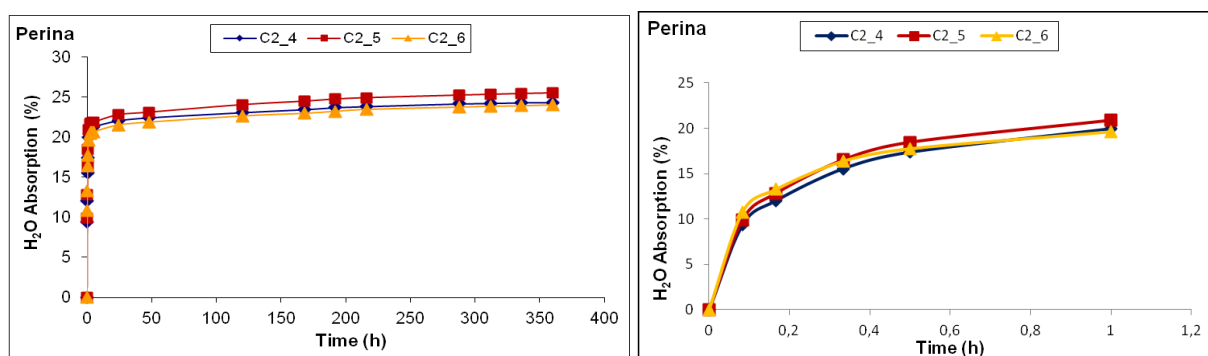


Figure 4.33: Total water absorption curves for Perina quarry samples (UNI-EN 13755). On the right is reports the shape of the curves in the time interval between 0h and 1h

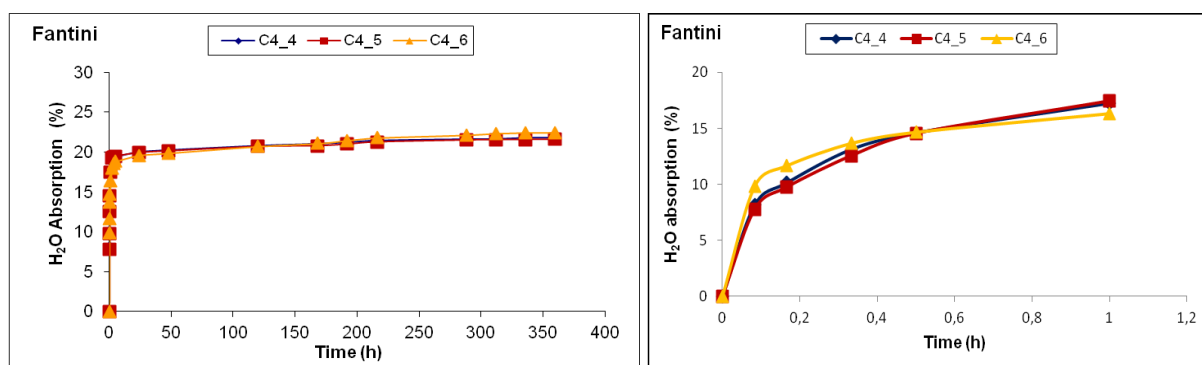


Figure 4.34: Total water absorption curves for Fantini quarry samples (UNI-EN 13755). On the right is reports the shape of the curves in the time interval between 0h and 1h

The total water absorption curves have a first portion rather steep, that corresponds to the time taken to reach saturation. The saturation is already achieved in the first hour of the test.

4.7.2. ULTRASONIC VELOCITY TEST (UNI EN 14579)

A better knowledge of lithification process can be obtained through determination of ultrasonic velocity, since this parameter may be related to the density, and therefore to the compactness of the rock.

Table 4.25 reports the ultrasonic velocity values for all investigated samples. Samples of Cannetaccio quarry have an ultrasonic velocity ranging between 2088 m/s and 2243 m/s; Perina samples shows a lower ultrasonic velocity values, ranging between 1969 m/s and 2128 m/s, whereas samples belong to Fantini quarry have the lowest values range between 1880 m/s and 2049 m/s.

This data variability is definitely due to the heterogeneity of the material and their textural features. The higher ultrasonic velocity can be attributed to the high compactness of the rock, due to minor amount of pumice, and/or to the higher occurrence of lithics.

Table 4.25: Ultrasonic velocity values (Vs m/s)

Quarry	Sample	Vs (m/s)	Average m/s
Cannetaccio	CV_1	2173	2148
	CV_2	2233	
	CV_3	2243	
	CV_4	2062	
	CV_5	2089	
	CV_6	2088	
Perina	C2_0	2011	2032
	C2_1	2053	
	C2_2	2128	
	C2_3	2064	
	C2_4	1996	
	C2_5	1969	
	C2_6	2006	
	C2_7	2028	
Fantini	C4_1	2049	1939
	C4_2	1984	
	C4_3	1880	
	C4_4	1881	
	C4_5	1926	
	C4_6	1913	

4.7.3. UNIAXIAL COMPRESSIVE STRENGTH TEST (UCS, UNI EN 11926)

Lithification grades of the rock can be indicated by measuring their compressive strength. The response of a material to compression may be affected by several factors such as structure, texture, and alteration. The former, and in particular its cohesion grade, influence the values of compressive strength.

Table 4.26 reports the uniaxial compressive strength values, the UCS mean values and deviation standard of the whole data set from samples. Samples belonging to Cannetaccio quarry show an UCS values ranging between 6.14 and 8.87 MPa, they have a UCS average value of 7.48 Mpa. Perina samples have both a lower UCS range (between 5.72 and 7.45 MPa) and UCS mean value (6.42 MPa), rather than Cannetaccio; samples belong to Fantini quarry have the lowest UCS range and UCS mean value rather than the whole samples, they have a mean value of 5.03 MPa.

Table 4.25: UCS (Mpa) values

Quarry	Sample	UCS (MPa)	Average UCS (MPa)	Dev. Stand.
Cannetaccio	CV_1	8.87	7.48	1.06
	CV_2	7.48		
	CV_3	8.49		
	CV_4	6.53		
	CV_5	6.14		
	CV_6	7.36		
Perina	C2_0	5.69	6.42	0.68
	C2_1	5.72		
	C2_2	6.74		
	C2_3	7.45		
	C2_4	5.77		
	C2_5	6.88		
	C2_6	6.12		
	C2_7	6.97		
Fantini	C4_1	5.44	5.03	0.65
	C4_2	6.17		
	C4_3	4.67		
	C4_4	4.41		
	C4_5	4.73		
	C4_6	4.77		

The correlation between uniaxial compressive strength and textural features of rocks is highlighted by graphic of figure 4.35 where the high UCS values coincide with high ultrasonic velocity values, therefore there is a direct proportion between UCS value and textural features of the deposit.

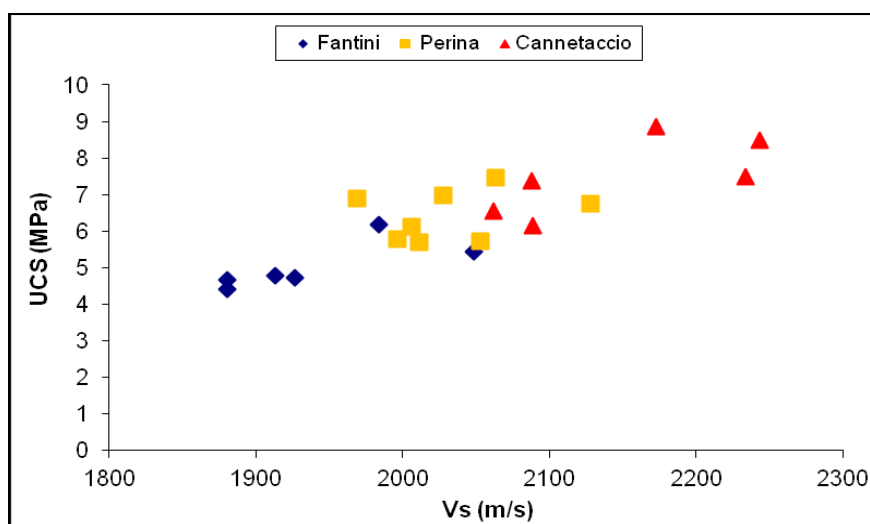


Figure 4.35: Diagram UCS vs ultrasonic velocity

In order to verify the relationship between zeolites content and compressive strength, a quantitative mineralogical analysis was performed on a set of samples subjected to UCS test. Table 4.26 reports the results of this comparison, and shows that all samples are chabazite-prevalent; Cannetaccio samples have a chabazite range content between 21-24 wt%, Perina samples have a chabazite range between 29-39 wt%, whereas Fantini samples show the higher chabazite content (>50 wt%). The lower zeolites content in Cannetaccio and Perina samples, correspond with higher feldspars content, vice-versa for Fantini samples. Calcite content range between 8 and 17 wt%. SEM observations allow to verify the presence of adularia in samples with the higher feldspar content (Cannetaccio and Perina), while it is not observed in Fantini samples. These results apport additional relevant evidence of the minerogenetic model described in this research.

Table 4.26: RIR values of UCS samples, with the corresponding UCS values

Quarry	Sample	Smectite %	Chabazite %	Phillipsite %	Feldspar %	Calcite %	Total %	Amorphous	UCS (MPa)
Cannetaccio	CV_1	10 (± 1)	24 (± 1)	4 (± 1)	27 (± 5)	10 (± 1)	75 (± 9)	25	8,87
	CV_3	9 (± 1)	27 (± 1)	5 (± 1)	26 (± 9)	11 (± 1)	78 (± 13)	22	8,49
	CV_6	10 (± 1)	21 (± 1)	4 (± 1)	22 (± 10)	15 (± 1)	73 (± 14)	27	7,36
Perina	C2_0	7 (± 1)	29 (± 2)	5 (± 1)	15 (± 3)	17 (± 1)	73 (± 8)	27	5,69
	C2_6	8 (± 1)	39 (± 2)	7 (± 1)	20 (± 3)	12 (± 1)	86 (± 8)	14	6,12
	C2_7	11 (± 2)	35 (± 2)	6 (± 1)	17 (± 7)	11 (± 1)	81 (± 13)	19	6,97
Fantini	C4_1	9 (± 1)	55 (± 3)	4 (± 1)	13 (± 3)	12 (± 1)	93 (± 9)	7	5,44
	C4_2	8 (± 1)	53 (± 3)	3 (± 1)	13 (± 6)	10 (± 1)	86 (± 12)	14	6,17
	C4_3	10 (± 1)	58 (± 3)	6 (± 1)	11 (± 4)	8 (± 1)	64 (± 10)	6	4,67
	C4_4	9 (± 1)	55 (± 3)	5 (± 1)	10 (± 4)	11 (± 1)	90 (± 10)	10	4,41
	C4_5	8 (± 1)	62 (± 3)	4 (± 1)	11 (± 4)	10 (± 1)	95 (± 10)	5	4,73
	C4_6	9 (± 1)	54 (± 3)	3 (± 1)	8 (± 4)	13 (± 1)	87 (± 10)	13	4,77

Error in brackets = $\sqrt{\sigma_1^2 + \sigma_2^2 + \dots}$ (Chipera and Bish, 1995), amorphous % by difference

In order to identify the mineralogical phase that affects the compressive strength, it is carried out a correlation between the UCS values with chabazite, feldspar and calcite content (figure 4.36).

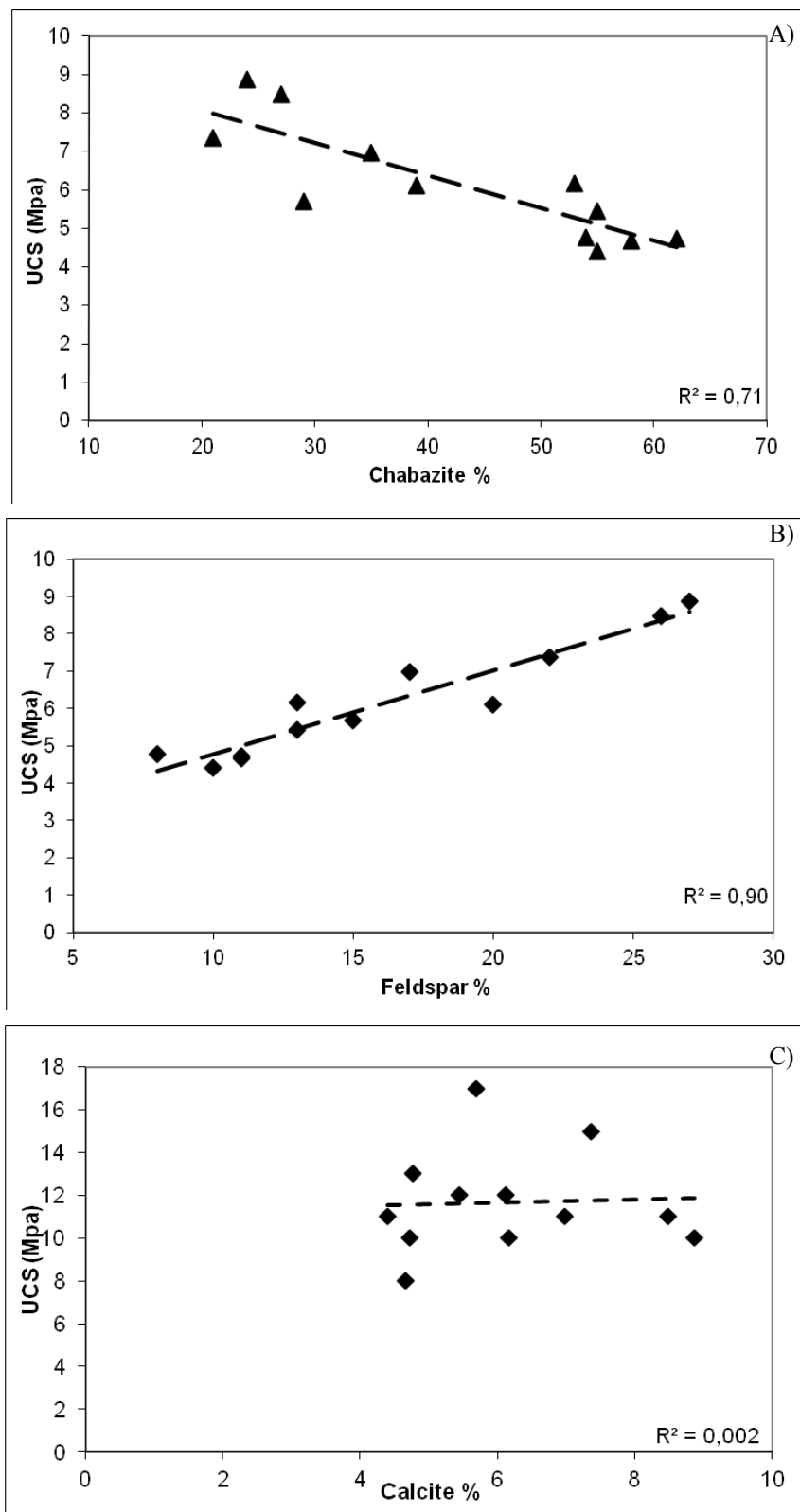


Figure 4.36: Relationship between UCS (Mpa) values and a) chabazite, b) feldspar and c) calcite content.

Figure 4.36a shows a negative correlation between UCS values and chabazite content, where high compressive strength values coincide with low zeolite content. A better correlation is

showed by UCS and feldspar ratio, where there is a direct proportion between compressive strength and feldspar percentage, higher UCS value coincides with higher feldspar content, figure 4.36b shows a better interpolation line with R^2 value of 0.9. Finally, there is no good relationship between UCS and calcite content, also showed by the lowest R^2 value close to 0.

4.7.4. LINEAR THERMAL EXPANSION COEFFICIENT (UNI EN 14581)

The zeolite content influences another petrophysic parameter: thermal dilatation (Marino et al. 1991, Colella et al 2009). Table 4.27 shows the results of investigated samples, belonging to Cannetaccio, Perina and Fantini quarries. For the whole samples a dimensional contraction has been registered. This behavior can be related with dehydration of zeolitic phases as a result of heating, that leads to a reduction of volume of the zeolitic framework, with the contraction of the specimen. The results show an increase of contraction from Cannetaccio ($-5.31 \cdot 10^{-6} \text{mm/mm } ^\circ\text{C}^{-1}$) to Perina ($-12.85 \cdot 10^{-6} \text{mm/mm } ^\circ\text{C}^{-1}$) to Fantini ($-17.73 \cdot 10^{-6} \text{mm/mm } ^\circ\text{C}^{-1}$) samples, attributed with the growing zeolites content.

Table 4.27: Thermal dilatation results

Quarry	Sample	Mean sample ($10^{-6} \text{mm/mm } ^\circ\text{C}^{-1}$)	min	max	dev.st.	Mean quarry ($10^{-6} \text{mm/mm } ^\circ\text{C}^{-1}$)
Cannetaccio	1	-6,91	-14,00	-4,16	4,10	-5,31
	2	-5,75	-10,83	-2,83	3,17	
	3	-4,00	-8,66	-1,66	2,74	
	4	-5,83	-8,66	-4,50	1,66	
	5	-4,08	-6,16	-3,16	1,22	
Perina	1	-11,96	-17,17	-10,00	3,01	-12,85
	2	-10,37	-17,66	-7,16	4,24	
	3	-16,96	-21,83	-14,50	2,86	
	4	-12,12	-19,50	-9,00	4,28	
Fantini	1	-18,29	-28,00	-14,16	5,66	-17,73
	2	-17,04	-26,33	-13,83	5,36	
	3	-20,25	-29,83	-16,50	5,54	
	4	-17,96	-27,16	-14,66	5,32	
	5	-16,25	-25,00	-13,00	5,06	
	6	-16,62	-25,33	-13,00	5,05	

5. DISCUSSION

Volcanological and mineralogical aspects allowed to hypothesize a minerogenetic processes that affected the three sub-units of Upper Tufo Giallo della Via Tiberina (UTGVT) formation. The UTGVT is made up of three distinct pyroclastic flow units :UTGVTa, UTGVTb and UTGVTc ranging in age between 551 ka and 547 ka. The products of UTGVT eruptions occurs as un-welded and welded facies. The UTGVTa and UTGVTb units (the lowermost units of the whole succession) are made up of yellowish lithified massive cineritic layer; and they are characterized by white pumice clasts, contain scarce feldspar and clinopyroxene. The lithified facies are overcome by an un-welded cineritic deposit, which represent the discontinuity layer between units; these facies are only visible where deposits reach the lowermost thickness, for example around the abandoned quarries of km 12,7 and 13 of Tiberina road. The uppermost unit, UTGVTc, is made up of poorly lithified deposit with pumice rich layers; it is characterized by black-grey scoria clasts, which contain diffuse leucite phenocrysts. Field investigations allow to define the stratigraphic relationship of the mentioned three flow units (in three main investigated outcrops: Km 13-12.7, Perina and Cannetaccio quarries) with the pre-volcanic basement (figure 5.1).

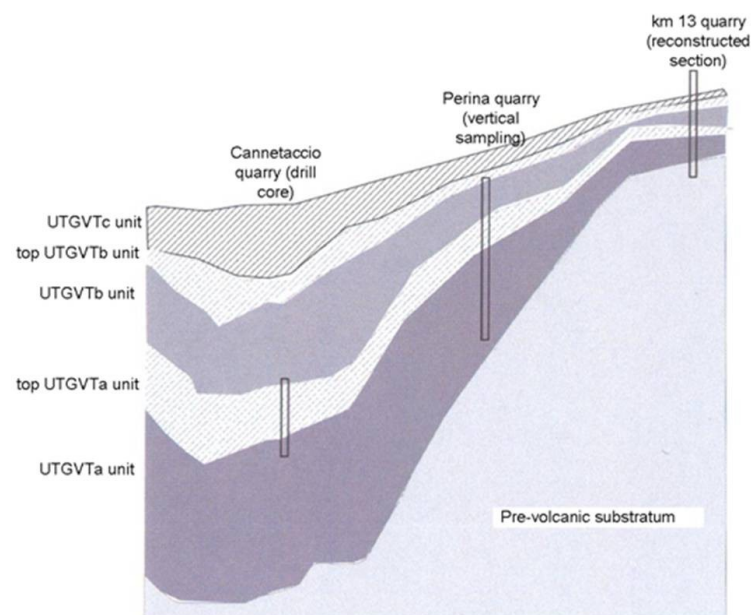


Figure 5.1: Stratigraphic relationship between investigated outcrops and pre-volcanic basement

Field data show that the thickness of units is not constant. Whenever the formation reaches highest thickness no clear evidence, of the presence of overlapping flow units, can be pointed

out; probably the discontinuity layers between units was erased from the subsequent flow unit. Field evidence (accretionary lapilli, dune structure) allowed to identify the emplacement mechanism, that involve water-magma interaction. The products of the eruption were characterized by an abundant fluid phase and emplacement temperature of a few hundred degree Celsius.

From a mineralogical point of view, the lowermost units (UTGVTa and UTGVTb) have similar mineralogical composition. In particular they are characterized by the presence of authigenic minerals, primarily zeolites and feldspars. Zeolites are characterized by the prevalence of chabazite, followed by phillipsite and in some outcrop (km 13-12.7 and Cannetaccio quarries) also analcime is found. Mainly zeolites are found in lithified facies of UTGVTa and UTGVTb units that are almost completely devitrified, while the un-lithified facies of these units show a very limited amount of zeolites (18 wt%) and feldspar (between 7 and 16 wt%), retaining its original glassy nature. Wherever the UTGVTc unit is observed, it has a lower lithification degree rather than the lithified facies of the aforementioned a and b sub-units.

Mineralogical data shows that the upper part of the UTGVTa unit, wherever deposit reaches its higher thickness (Cannetaccio quarry), is characterized by prevalent phillipsite, followed by chabazite and analcime. In this outcrop can be also observed the higher content of feldspar (about 30 wt%), where SEM observations allow to attribute this high values to an authigenic feldspar (adularia). The middle and lower part of UTGVTa (Fantini quarry) units show an slightly increase of chabazite content, reaching 64 wt%, while analcime disappears. Laboratory analyses allow to attribute analcime to the alteration of primary leucite. Since UTGVTa flow unit is associated to the emission of products from the inner portion of magma chamber, which are characterized by the absence of primary leucite, this feature explains the lack of analcime in the lowermost part of unit. Wherever the discontinuity layer between UTGVTa and UTGVTb units is not observed, for example along both the floor of Cannetaccio quarry and the wall of Perina quarry, the layer with prevalent phillipsite could be attributed to the top of UTGVTa unit, thus identifying the level that distinguish the two sub-units. Along the outcrop where UTGVTa deposit reaches the lower thickness (along the wall of km 13 quarry); this layer shows prevalent chabazite with minor amount of phillipsite, feldspar, with a slightly decrease of analcime towards the lower part of outcrop. SEM observation allow to attribute the high phillipsite content to the pumice concentration; this feature suggest that the juvenile clasts are concentrated in the uppermost portion of body of pyroclastic flow (Cannetaccio and Perina

quarry). Pumice content probably decrease toward the tail of pyroclastic flow (km 13-12.7 outcrop).

As regard to the UTGVTb unit, it is characterized by prevalent chabazite from the upper towards the lower part of the deposit; wherever unit reaches the highest thickness, lack of analcime can be observed, with a slightly increase of phillipsite content.

The UTGVTc flow unit is characterized by the occurrence of analcime, with its higher content (21 wt%), along with minor amount of phillipsite, feldspar and smectite. The higher content of analcime is associated to diffuse leucite phenocrysts that characterize products emitted from the peripheral portion of magma chamber.

The mineralogical features of UTGVTa, UTGVTb, and UTGVTc flow unit are outlined in figure 5.2, where the prevalent phillipsite layer can be observed; it identifies the level that distinguish the UTGVTa unit from UTGVTb unit, wherever the discontinuity layer are erased from the overlapping pyroclastic flow.

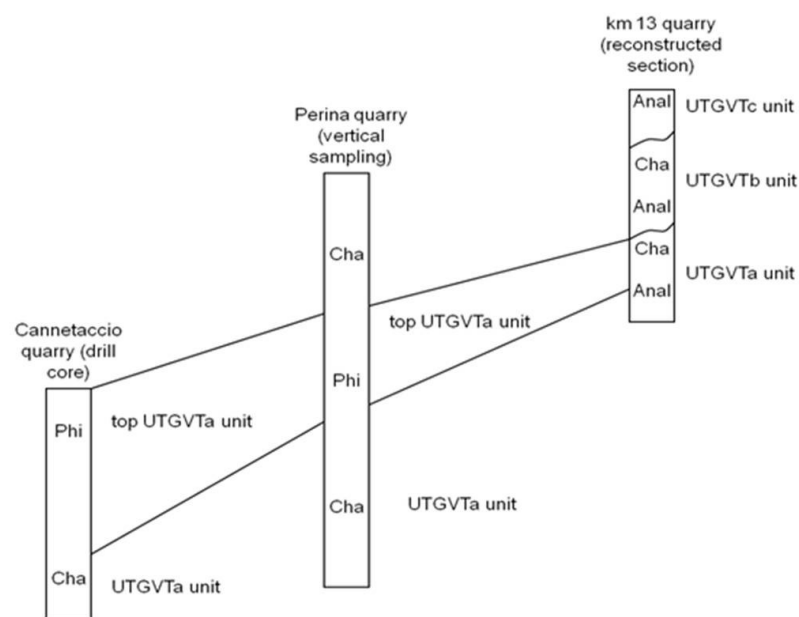


Figure 5.2: Reconstructed zeolitic assemblages and vertical variation in km 13-12.7, Perina and Cannetaccio quarries.

The occurrence of phillipsite or chabazite within the UTGVTa and UTGVTb suggest temperatures suitable for zeolitization by interaction of fresh glass with water; this water that can be attributed to eruption type (phreatomagmatic), but also to paleo-Tiber river and meteoric waters. The existence of favorable conditions for zeolitization during emplacement of the volcanoclastite is confirmed by volcanological features; for example the occurrence of layers

with accretionary lapilli indicate that the emplacement temperature was very close to the water condensation point (de' Gennaro et al., 2000).

Available data not allow determination of waters pH values during emplacement. However, indirect evidences support the presence of initial acid pH. The acidic solutions began to circulate within the deposit, causing the glass alteration with the subsequent formation of smectite, as confirmed by SEM observations. The acidic solutions also interact with the carbonatic clasts, that occur within the deposit, thereby causing a buffer effect on the system with hydrolysis and dissolution of the glassy fraction. Glass hydrolysis produces an early Na enrichment, suitable for the analcimization process of leucite (Giampaolo et al., 1997). Thereby the solution was indirectly enriched in potassium; this achieved a sodic-potassic environment, suitable for phillipsite crystallization within the pumice. Afterwards both K and Ca were enriched. The Ca enrichment was due to the previous dissolution of carbonatic clasts, too. Thereby conditions more favorable for chabazite formation were obtained (de Gennaro et al., 1999). The residual Ca-rich solution, which was not involved in the chabazite crystallization, produces favorable condition for the crystallization of secondary calcite that fills the fractures of the rock. Field investigations have shown the occurrence of crystallizations of secondary calcite in the lower part of formation (calcite crystals around carbonized woods). The calcic environment is also highlighted by the chemical composition of zeolitic phases, that show an higher Ca content than the same authigenic minerals belong to others central-southern Italian volcanoclastic formation. The K enrichment also establishes favorable conditions for the formation of authigenic feldspars in some portion of the deposit, where the highest temperatures were preserved for a long time, for example whenever it reaches high thickness (Cannetaccio quarry). This hypothesis is confirmed by SEM observations; they showed the absence of adularia in samples, belonging to outcrop with the lower thickness (km 12.7-13 quarries) or from the lower part of the sub-unit a (Fantini quarry). The latter has been cooled faster, due to its contact with the sedimentary basement. Authigenic feldspar is observed in association both with phillipsite or chabazite crystals (resulting from a series of reactions from metastable to more stable phases) and also on wall of altered glassy shards (high temperature suitable for feldspatization).

Comparison between cation composition of glass and its derivative phases does not reveal, whether the cations favored the crystallizations of one or the other zeolite. This suggests that the solution exerts an important role in the crystallization of zeolites from glass.

Chemical compositions of chabazite reveal the occurrence of two type of this zeolite (Ca-rich chabazite and K-rich chabazite). Chemical and mineralogical data show the association of Ca-rich chabazite and authigenic feldspar, and K-rich chabazite and primary feldspar. These associations could suggest an exchange process of chabazite with the Ca-rich solution; thereby leading to the Ca-rich chabazite. While wherever exchange process with the solution was lacking; this determine the occurrence of K-rich chabazite and the crystallization of secondary calcite from the calcitic solution. The chemical exchanges with the surrounding environment can suggest the action of percolating solution in open hydrologic systems (Sheppard and Hay, 2001).

The secondary crystallization of authigenic minerals such as zeolites and feldspars progressively enhances the physical properties of the deposit. But also the eruption mechanisms, emplacement condition, temperature, degree of lithification affect the geotechnical characteristic of volcanoclastic formation (Bear et al., 2009). Zeolites act as a cementing agent in pyroclastic rocks causing superior mechanical properties compared with non-zeolitized deposits (Aversa and Evangelista, 1998; Evangelista et al., 2000). Previous studies conducted on the mechanical properties of volcanic tuffs have shown a linear relationship between porosity and uniaxial compressive strength; as porosity decrease, subsequently the uniaxial compressive strength and cohesiveness of the deposit increase (Evangelista et al., 2000; Langella et al., 2002; Bear et al., 2009). These studies have also shown that zeolitization progressively fills pore and therefore decreases the overall porosity of the deposit. Langella et al. (2002) have observed that the decrease of porosity is due to the zeolites content increase. This process is related to the reduction of macropores among the glass shards when zeolites take over the shards surfaces.

The results of the present research have shown that not only zeolites, but also feldspars and calcite exert an important role on physical properties of the deposit. Notwithstanding the high open porosity values (>47 wt%), it is recorded a lower imbibition coefficient about 22 wt% than other southern-central Italian pyroclastic deposits (Neapolitan Yellow Tuff-NYT, 44 wt%, Di Benedetto, 2011). This low value could be attributed to secondary calcite that has hindered water absorption.

Laboratory analyses show the good relationship between ultrasonic velocity and uniaxial compressive strength (UCS); they also show that the cohesiveness and strength of the deposit, are related to the textural and fabric of the rocks (lithics, clast and pumice concentration). The

high zeolite content (samples belong to Fantini quarry) can be related to the higher pumice concentration, that explains the lower UCS values.

Petrophysical characterization reveals, the better compressive strength of the UTGVT (about 6 MPa) than others volcanoclastic deposit (for example the NYT formation with a mean UCS of 3 MPa; Di Benedetto, 2011). Petrophysical data also reveals the better relationship between feldspar content and UCS values, and this feature evidenced that feldspatization process, involving mainly the central part of UTGVT formation, greatly improves the geotechnical characteristic of this deposit.

CONCLUSION

The reconstruction of the minerogenetic processes that affected the Upper Tufo Giallo della Via Tiberina formation, was carried out by a comparative study, taking in account both volcanological and mineralogical features.

In an early phase of research a careful geovolcanological characterization was performed. Field investigations allowed to reconstruct: 1) geometry of the deposits; 2) stratigraphy of the products. These two aspects showed the variable thickness of the deposits, due to the pre-volcanic basement, represented by the paleo-Tiber river valley. This feature determined a very high variability of thickness inside a limited area (80m in Cannetaccio, 15m at km 13 quarry). The stratigraphy of the formation allowed to distinguish three distinct flow units (UTGVTa, UTGVTb, UTGVTc). The lowermost units (a, and b) showed similar features; both are made up of yellowish lithified massive cineritic layer, separated by an un-lithified cineritic deposits. The uppermost unit, UTGVTc, is constituted by an un-lithified deposit with pumice-rich layers. Whenever deposits reach high thickness, no clear evidence of separation among different flow units were observed; the discontinuity layers, whose presence was reported in the result section, were probably obliterated by the erosion properties of the following unit.

Results of volcanological characterization allowed to ascribe the deposit to a pyroclastic flow-like emplacement mechanism. The cineritic grain-size of matrix, the occurrence of dune structures in un-lithified layers and the presence of accretionary lapilli within the deposits suggested a strong interaction between water and magma.

It is well known that the water-magma interaction mechanism favored the formation of authigenic minerals. The main results of present research can be summarized as follows:

- ✓ Presence of water, linked to a phreatomagmatic eruption, favored hydrolysis processes of volcanic glass. The water-glass interaction led to formation of zeolites (chabazite and phillipsite). The chemical composition of precursor glass (trachytic-phonolitic) could have been played an important role in the crystallization of one or other zeolite; but the prevalence of chabazite in whole deposit, except for the middle portion of investigated sections, suggested an important role played instead by the chemical composition of water (Ca-rich solution). The joint prevalence of Ca^{2+} and K^+ , this latter released during hydrolysis, in solution directed the crystallization of authigenic phases towards chabazite; this hypothesis is confirmed by the calcic-potassic composition of this

zeolite. The previous assumption is also verified by the occurrence of phillipsite mainly within pumice, where favorable conditions (presence of Na and K) to the crystallization of this phase were obtained. The Ca-rich solution led to phillipsite with an high calcium content, if compared to the same zeolite of others Italian volcanoclastic formations.

- ✓ An important feature of UTGVT formation is represented by the occurrence of high Ca values in the bulk rocks ($\text{CaO} > 10 \text{ wt\%}$), which was never observed in others Italian zeolitized volcanoclastic formations. The high Ca value was early attributed to the presence of carbonatic clasts, belonging to sedimentary basement, but further investigations showed a widespread occurrence of Ca within the rocks. These data allowed to attribute the high Ca values to a diffuse “secondary stage” of calcite precipitation, triggered by the increase in pH values.

The aforementioned features led to hypothesize that post-emplacement process developed in several successive stages. The minerogenetic model can be described as follows:

- 1) The initial acidic solution began to circulate within the deposit, causing the glass alteration with subsequent formation of smectite. This feature was also observed in others volcanoclastic deposits (i.e. Neapolitan Yellow Tuff and Campanian Ignimbrite);
- 2) the acidic solution also interacted with the carbonatic clasts, occurring within the deposit, thereby causing an increase of Ca^{2+} ion in the solution;
- 3) the growing of pH toward higher values and the hydrolysis of glass determine the increase of K and Na in solution. It is well known that a calcic-potassic environment favours the crystallization of chabazite. This process explained the prevalence of chabazite in the whole investigated sections. Only for longer reaction time, phillipsite crystallized;
- 4) the pH increased, favoring the crystallization of secondary calcite, with a subsequent decrease of Ca and an indirect increase of K in the solution. This led to a suitable condition for the crystallization of phillipsite and chabazite. Chemical analyses of K-rich zeolites confirm this hypothesis;

- 5) chemical composition of zeolites (phillipsite and chabazite) is in agreement with those findings; both phases are potassic-calcic. In chabazites the extraframework cation content can be summarized as follow: $\text{Ca} > \text{K} > \text{Na}$, whereas in phillipsites $\text{K} > \text{Ca} > \text{Na}$.
- 6) in the portions of the deposits, where temperature was maintained for longer times, conditions suitable for the crystallization of adularia-like feldspar were obtained.

The results suggested that lithification of Upper Tufo Giallo della Via Tiberina can be related both to zeolitization process and to secondary calcite crystallization. The lithification process, in several volcanic tuffs (i.e Neapolitan Yellow Tuff-NYT), was credited to transformation of un-lithified material (*pozzolana*) into lithoid tuff after zeolitization process. The most important features of UTGVT formation is the occurrence of cement of double origin: zeolites and secondary calcite. This lithification process account for the better petro-physical features of TGVT than others volcanoclastic deposits (NYT and CI). Wherever zeolitization should evolve toward more stable phases (like authigenic feldspars), a further improvement in the geotechnical characteristic of this deposit could be observed.

REFERENCES

- Aleksiev, B.**, Djourova, E.G. (1975). On the origin of zeolite rocks. *Comptes Rendus de l'Academie Bulgare des Sciences* 28, 517-520.
- Alvarez W.** (1973). Ancient course of Tiber River near Rome: an introduction to the Middle Pleistocene volcanic stratigraphy of Central Italy. *Geol. Soc. Am. Bull.* 84, 749-758.
- Aversa S.**, Evangelista A., (1998). Mechanical behaviour of a volceianic tuff; yield, strenght and destructureation effects. *Rock Mech. Rock Eng.* 31, 359-366.
- Barth F.W. T** (1948). Oxygen in Rocks: A Basis for Petrographic Calculations. *The Journal of Geology.* 56,(1), 50-60.
- Bear, A.N.**, Giordano, G., Giampaolo, C., Cas, R.A.F., (2009). Volcanological constraints on the post-emplacement zeolitization of ignimbrites and geoarcheological implications for Etruscan tomb construction (6th-3rd century B.C.) in the Tufo Rosso a Scorie Nere, Vico Caldera, Central Italy. *Journal of Volcanology and Geothermal Research.* 183, 183-200.
- Bish D. L.** and Chipera S. J. (1988) Problems and solution in quantitative analysis of complex mixture by X ray powred diffraction, *Adv. X ray Anal.*, 31, 295-307.
- Bish, D.L.**, Post, J.E., (1993). Quantitative mineralogical analysis using the Rietveld full-pattern fitting method. *American Mineralogist* 78, 932-940.
- Blanc A.C.**, Cova G., Franceschi P., Lona F., Settepassi F. (1955). Ricerche sul quaderno laziale. II – Una torba glaciale, avifauna artica, e malacofauna montana nel Pleistocene medio-inferiore dell'agro Cerite a di Roma. Il periodo glaciale Flaminio. *Quaternaria*, 2, 151-186.
- Cappelletti P.**, Cerri G., Colella A., de'Gennaro M., Langella A., Perrotta A., and Scarpati C. (2003). Post-eruptive processes in the Campanian Ignimbrite. *Mineralogy and Petrology*, 79, 79–97.
- Cappelletti P.**, Langella A., de Gennaro R. and Colella A. (1999). Mineralogical and technical features of zeolite deposits from northern latium volcanic districts. *Periodico di Mineralogia*, 68 (2), 127-144.
- Cappelletti P;** Rapisardo G, de Gennaro B., Colella A ., Langella A, Graziano S.F., Bish D.L, de Gennaro M., (2011). Immobilization of Cs and Sr in aluminosilicate matrices derived from natural zeolites. *Journal of Nuclear Materials.* 414, 451–457.

- Campobasso C.**, Cioni R., Salvati L., Sbrana A. (1994). Geology and paleogeographic evolution of a peripheral sector of the Vico and Sabatini volcanic complex, between Civita Castellana and Mazzano Romano (Latium, Italy). *Men. Descr. Carta Geol. d'It.*, 49, 277-290.
- Cioni, R.**, Sbrana, A., Bertagnini, A., Buonasorte, A., Landi, P., Rossi, U., Salvati, L., (1987). Tephrostratigraphic correlations in the Vulsini, Vico and Sabatini volcanic successions. *Per. Mineral.* 56, 137–155.
- Chipera S.J.**, Guthrie Jr G.D., Bish D.L., (1993). Preparation and purification of mineral dusts, in: G.D. Guthrie Jr., B.T. Mossman (Eds.), *Health Effects of Mineral Dusts*, , Mineralogical Society of America, Washington, DC. 28, 235–249.
- Chipera S.J.** and Bish D.L. (1995) Multirefection RIR and intensità normalizations for quantitative analyses: applications to feldspar and zeolites, *Powder Diff.*, 10 (1), 47-55.
- Chung F. H.** (1974) Quantitative interpretation of X-ray diffraction patterns of mixture I. Matrix-flushing method for quantitative multicomponent analysis, *J. Appl. Cryst.* 7, 519-525.
- Colella C.** (1996). Ion exchange equilibria in zeolite minerals, *Mineralium Deposita*, 31, 554-562.
- Conticelli S.**, Manetti P., Peccerillo A. Santo A. (1986). Caratteri petrologici della vulcaniti potassiche italiane: considerazioni genetiche e geodinamiche. *Mem. Soc. Geol. Ital.* 35, 775-783.
- de Gennaro B.**, Colella A., Cappelletti P., Pansini M., de Gennaro M., Colella C., (2005). Effectiveness of clinoptilolite in removing toxic cation from water: a comparative study, *Studies in Surface Science and Catalysis*, 158B, 1153-1160.
- de Gennaro B.**, Aprea P., Colella C., Buondonno A. (2009). Comparative ion-exchange characterization of zeolitic and clayey materials for pedotechnical applications—Part 2: interaction with nutrient cations. *J Porous Mater* 16:667–673.
- de' Gennaro M.** and Franco E. (1979) Arricchimento e separazione delle zeoliti di rocce piroclastiche, *L' Industria Mineraria*, 30, 329-336.
- de' Gennaro, M.**, Langella, A., Colella C., Coppola E., and Buondonno A. (1995b). Italian zeolitized tuffs as soil conditioners. Recent research advances. In *Natural Zeolites*. Kirov G., Filizova L., Petrov O. Eds., Sofia 93-100.

- de' Gennaro, M.** and Langella, A (1996). Italian zeolitized rocks of technological interest. *Mineralium Deposita*, 31, 452-472.
- de' Gennaro, M.**, Langella, A., Cappelletti, P., Colella, C., 1999. Hydrothermal conversion of trachytic glass to zeolite. 3. Monocationic model glasses. *Clays and Clay Minerals*. 47 (3), 348-357.
- de' Gennaro M.** Cappelletti P. Langella A. Perrotta A., Scarpati C. (2000). Genesis of zeolites in the Neapolitan Yellow Tuff: geological, volcanological and mineralogical evidence , *Contrib Mineral Petrol*. 139,17-35.
- de' Gennaro M.**, Colella A., Aprea P., Colella C.,(2003). Evaluation of an intermediate-silica sedimentary chabazite as exchanger for potentially radioactive cation, *Microporous and Mesoporous Material*. 61, 159-165.
- de Gennaro R.**, Cappelletti P., Cerri G., de' Gennaro M., Dondi M., Graziano S.F., Langella A. (2007). Campanian Ignimbrite as raw material for lightweight aggregates, *Applied clay science* . 37, 115-126.
- de Gennaro R.**, Dondi M. Cappelletti P., Cerri G., de' Gennaro M., Guarini G., Langella A., Parlato L, Zanelli C (2007). Zeolite-feldspar epiclastic rocks as flux in ceramic tile manufacturing; *Microporous and Mesoporous Materials*; 105, 273-278.
- de Gennaro R.**, Langella A., D'Amore M. Dondi M., Colella A., Cappelletti P., de' Gennaro M. (2008). Use of zeolite-rich rocks and waste material for the production of structural lightweight concretes. *Applied clay science*. 41, 61-72.
- de Rita, D.**, Funicello, R., Parotto, M., (1988). Geological Map of the Colli Albani Volcanic Complex. Progetto Finalizzato Geodinamica C.N.R., Rome, Italy.
- de Rita, D.**, Funicello, R., Corda, L., Sposato, A., Rossi, U., (1993). Volcanic units. In: Di Filippo, M. (Ed.), *Sabatini volcanic complex. : Quad. Ric. Sci., Vol. 114. Progetto Finalizzato Geodinamica C.N.R, Roma, pp. 33–79.*
- de Rita, D.**, Di Filippo, M., Rosa, C., (1996). Structural evolution of the Bracciano volcanotectonic depression, Sabatini Volcanic District, Italy. In: McGuire, W.J., Jones, A.P., Neuberg, J. (Eds.), *Volcano instability on the Earth and other planets: Geol. Soc. London Spec. Publ., Vol. 110, pp. 225–236.*

- de Rita, D.**, Bertagnini, A., Faccenna, C., Landi, P., Rosa, C., Zarlenga, F., Di Filippo, M., Carboni, M.G., (1997). Evoluzione geopetrografica-strutturale dell'area tolfetana. *Boll. Soc. Geol. It.* 116, 143–175.
- Di Bartolomeo P.**, Dondi M., and Marsigli M. (1996). Use of zeolitic rocks in ceramic tile production. *Tile and Brick Int.*, XII. 4, 311-318.
- Dibbel W.E. Jr**, Tiller W.A. (1981). Kinetic model of zeolites paragenesis in tuffaceous sediments. *Clays and Clays Minerals.* 29, 323-330.
- Di Benedetto** (2011). Valutazione dei parametri petrofisici del Tufo Giallo Napoletano e della Pietra di Vicenza: indagini sperimentali finalizzate al recupero ed alla conservazione di materiali macroporosi. Ph.D thesis.
- Evangelista A.**, Pellegrino A., 1990. Caratteristiche geotecniche di alcune rocce tenere italiane. In *Atti 3° Ciclo di Conferenze di Meccanica ed Ingegneria delle Rocce*, G Barla (ed.), SGE Editoriali, Padova, 2/1-2/31.
- Follieri M.**, Magri M.G. (1961). I legni fossili della Via Flaminia (Cava Bianca) presso Roma. *Ann. Bot.* 27 (1), 1-18.
- Follieri M.** (1963). Legni fossili nel tufo sovrapposto alle argille marine in località Paradisi (Roma). *Giorn. Bot. Ital.* 70, 685-689.
- Giacomelli L.**, Scandone R (2007). *Vulcani d'Italia*. Liguori editore.
- Giampaolo, C.**, Lombardi, G., (1994). Thermal behaviour of analcimes from two different genetic environment. *European Journal of Mineralogy* 6, 285-289.
- Hay R.L.** (1966). Zeolites and zeolitic reactions in sedimentary rocks. *Geol. Soc. Am. Spec. Paper.* 85, 130.
- Hay R.L.** and Sheppard R.A. (2001). Occurrence of zeolites in sedimentary rocks: an overview, *Reviews in mineralogy and geochemistry*, Mineralogical society of America , geochemical society . 45, 217-234.
- Karner DB**, Renne PR (1998). $^{40}\text{Ar}/^{39}\text{Ar}$ geochronology of Roman Province tephra in the Tiber River Valley: age calibration of Middle Pleistocene sea-level changes. *Geol Soc Am Bull* 110:740-747.

- Karner, D.B.**, Marra, F., Renne, P., (2001). The history of the Monti Sabatini and Alban Hills volcanoes: groundwork for assessing volcanic-tectonic hazards for Rome. *J. Volcanol. Geotherm. Res.* 107, 185–219.
- Klug H.P.**, Alexander L.E. (1974). X-ray diffraction procedures for polycrystalline and amorphous materials, J. Wiley and sons EDS., New York, 451.
- Langella A., de' Gennaro M., Colella C., and Buondonno A.** (1995). Effect of phillipsite or chabazite rich-tuff addition to soil on the growth and yield of Beta Vulgaris and Raphanus Sativus. In: Proc. III Convegno Nazionale di Scienza e tecnologia delle zeoliti, Cetraro: Aiello R., Ed. De Rose , Cosenza. 277-285.
- Langella A., De Simone P., Calcaterra P., de' Gennaro M.** (2002). Evidence of the relationship occurring between zeolitization and lithification in the yellow facies of the Campanian Ignimbrite (southern Italy). In Aiello et al., (Ed). Studies in surface science and catalysts. Elsevier Science. 1775-1782.
- Le Bas M.J., Le Maitre R.W., Streckeisen a., Zanettin B.** (1986). A chemical classification of volcanic rocks based on the total alkali-silica diagram. *J. Petrol.*, Vol. 27, p. 745-750.
- Lenzi, G., Passaglia, E.,** (1974). Fenomeni di zeolitizzazione nelle formazioni vulcaniche nella regione sabatina. *Bollettino della Società Geologica Italiana.* 93, 623-645.
- Lombardi, G., Nicoletti, M., Petrucciani, C.,** (1974). Età delle vulcaniti dei complessi Tolfetano, Cerite e Manziate (Lazio Nord-occidentale). *Per. Mineral.* 43, 351–376.
- Lombardi G., Meucci C., Mottana A.,** (2006). Il Tufo Giallo della Via Tiberina (Roma) utilizzato nei monumenti romani. *Rend. Fis. Acc. Lincei,* 17, 263-287.
- Lustrino M, Duggen S, Rosenberg CL** (2011). The Central-Western Mediterranean: Anomalous igneous activity in an anomalous collisional tectonic setting. *Earth Sci Rev* 104:1-40.
- Mariner, R.H., AND Surdam, R.C.** (1970). Alkalinity and formation of zeolites in saline alkaline lakes: *Science*, v. 170, p. 977–980.
- Mattias P.P., Ventriglia U.** (1970). La regione vulcanica dei Monti Sabatini e Cimini. *Soc. Geol. It.*, 331-384.
- Nappi G., De Casa G., Volponi E.** (1979). Geologia e caratteristiche tecniche del Tufo Giallo della Via Tiberina. *Boll. Soc. Geol. It.*, 98, 431-445.

- Nappi, G.**, Mattioli, M., (2003). Evolution of the Sabatinian Volcanic District (central Italy) as inferred by stratigraphic successions of its northern sector and geochronological data. *Per. Mineral.* 72, 79–102.
- NORMAL UNI EN 11926**, (2000). Natural stone test methods: determination of compressive strength. Ente Nazionale Italiano di Unificazione, Milano.
- NORMAL UNI EN 13755 (2002)**. Natural stone test methods: determination of water absorption at atmospheric pressure. Ente Nazionale Italiano di Unificazione, Milano.
- NORMAL UNI EN 14579**, (2005). Natural stone test methods: determination of ultrasonic wave velocity. Ente Nazionale Italiano di Unificazione, Milano.
- NORMAL UNI EN 14581**, (2005). Natural stone test methods: determination of linear thermal expansion coefficient. Ente Nazionale Italiano di Unificazione, Milano.
- Marra F.**, Deocampo D., Jackson M.D., Ventura G. (2011). The Alban Hills and Monti Sabatini volcanic products used in ancient Roman masonry (Italy): An integrated stratigraphic, archaeological, environmental and geochemical approach. *Earth Science review.* 108, 115-136.
- Masotta, M.**, Gaeta, M., Gozzi, F., Marra, F., Palladino, D.M., Sottili, G., 2010. H₂O- and temperature-zoning in magma chambers: the example of the Tufo Giallo della Via Tiberina eruptions (Sabatini Volcanic District, central Italy). *Lithos* 118, 119–130.
- Melluso L.**, Morra V., Brotzu P., Tommasini S., Renna M.R., Duncan R.A., Franciosi L., D'Amelio F. (2005). Geochronology and petrogenesis of the Cretaceous Antampombato–Ambatovy complex and associated dyke swarm, Madagascar, *J. Petrol.* 46, 1963–1996.
- Mumpton F.A. (1973)**. Worldwide deposits and utilization of natural zeolites. *Industrial minerals.* 73, 30-45.
- Pansini M.**(1996). Natural zeolites as cation exchangers for environmental protection. *Mineralium Deposita*, 31, 563-575.
- Passaglia E.** (1970) The crystal chemistry of chabazites, *The American Mineralogist*, vol. 55, 1278-1301.
- Passaglia, E.**, Vezzalini, G., (1985). Crystal chemistry of diagenetic zeolites in volcanoclastic deposits of Italy. *Contributions to Mineralogy and Petrology* 90, 190-198.
- Peccerillo A.** (2003) Plio-Quaternary magmatism in Italy. *Episodes*, 26, 222-226.

Peccerillo A. (2005) Plio-Quaternary volcanism in Italy. *Petrology, Geochemistry, Geodynamics*.

Springer, Heidelberg, 365 pp.

P.R.A.E Piano Regionale delle Attività Estrattive del Lazio (2007).

Serri G., Innocenti F., Manetti P., Tonarini S., Ferrara G. (1992). Il magmatismo neogenico quaternario dell' area tosco-laziale-umbra: implicazioni sui modelli di evoluzione geodinamica dell' Appennino settentrionale. *Studi geologici Camerti*, volume speciale. (1991/1), 429-463.

Sheppard R.A., Gude A. J III. (1968). Distribution and genesis of authigenic silicate minerals in tuffs of Pleistocene Lake Tecopa, Inyo County, California. *U.S. Geol Survey Prof. Paper*. 597, 38.

Sheppard R.A., Gude A. J III. (1969). Diagenesis of tuffs in the Barstow formation, Mud Hills, San Bernardino County, California. *U.S. Geol Survey Prof. Paper*. 634, 35.

Sheppard R.A., Gude A. J III. (1973). Zeolites and associated authigenic silicate minerals in tuffaceous rocks of the Big Sandy Formation, Mohave County, Arizona. *U.S. Geol Survey Prof. Paper*. 830, 36.

Sheppard R.A., Hay R.L. (2001). Formation of zeolites in open hydrologic systems. *Reviews in mineralogy and geochemistry, Mineralogical society of America , geochemical society*. 261-275.

Sottili G., Palladino D.M., Zanon, V., (2004). Plinian activity during the early eruptive history of the Sabatini Volcanic District, Central Italy. *J. Volcanol. Geotherm. Res.* 135, 361–379.

Sottili G., Palladino D.M, Marra F., Jicha B., Karner D.B., Renne P. (2010). Geochronology of the most recent activity in the Sabatini Volcanic District, Roman Province, central Italy, *J. Volcanol. Geotherm. Res.* (2010). 196, 20-30.

Stumm, W., Morgan, J.J., (1981). *Aquatic Chemistry. An introduction emphasizing chemical equilibria in natural waters* (2nd Ed.). John Wiley and Sons, New York.

Tsitsishvili G.V., Andronikashvili T.G., Kvashali N. Ph., Bagishvili R.M. and Zurabashvili Z.A. (1984). Agricultural application of natural zeolites in the Soviet Union. In *Zeo-Agriculture*,; Pond W.G., And Mumpton F.A. Eds, Westview Press, Boulder.

Washington H.S. (1906) *The Roman Comagmatic Region*. Carnegie Inst. Washington Publ. 57, 199 pp.

Young R.A. (1993). The Rietveld Method. IUCr Monograph of crystallography. Oxford Science Publication.